

BOSTON UNIVERSITY
GRADUATE SCHOOL OF ARTS AND SCIENCES

Dissertation

**SEARCH FOR NEUTRINOLESS DOUBLE BETA DECAY
TO EXCITED STATES OF BARIUM IN KAMLAND-ZEN**

by

HASUNG SONG

B.A. Physics, University of California, Berkeley, 2018

Submitted in partial fulfillment of the

requirements for the degree of

Doctor of Philosophy

2026

© 2026 by
HASUNG SONG
All rights reserved

Approved by

First Reader

Christopher Grant, PhD
Professor of Physics

Second Reader

Robert Carey, PhD
Professor of Physics

Acknowledgments

Now that it is finally time to reflect and look back on the over 6 year journey that has been my PhD, I am overwhelmed by the sheer number of people who contributed to my development over this time.

My advisor, Prof. Christopher Grant, gave me the precious gifts of his guidance, lectures, and near unlimited claim to his time. I will always be grateful for how he'd proactively search for development opportunities, be they in other groups, other universities, and in other countries. Prof. Lawrence Sulak gave a patient demonstration of how to be good experimentalist and the opportunity to work at CERN. Profs Kearns, Carey, Miller, Winslow, Axani, Li, Schmaltz, Ozaki, Shimizu, Ishidoshiro, Orebi-Gann, Anatoli, and many other professors, postdocs, technicians, and engineers I'd like to thank for the gifts of collaboration and lessons.

My fellow graduate students in the BU neutrino group, will always hold a special place in my heart for being confused with me, until we weren't. And I count myself incredibly lucky to have entered graduate school with such a fun, vibrant cohort, the entering BU Physics class of 2019.

Finally, my parents gave me the ultimate gifts of their support and love without which none of my achievements large and small would be possible.

I hope to make the most of what I've been given and make everyone proud.

Hasung Song
Boston University
Department of Physics

SEARCH FOR NEUTRINOLESS DOUBLE BETA DECAY TO EXCITED STATES OF BARIUM IN KAMLAND-ZEN

HASUNG SONG

Boston University, Graduate School of Arts and Sciences, 2026

Major Professor: Christopher Grant, PhD
Professor of Physics

ABSTRACT

Two-neutrino double beta decay to excited nuclear states ($2\nu\beta\beta^*$) provides important experimental constraints on nuclear matrix element calculations relevant to neutrinoless double beta decay searches. This dissertation presents a search for $2\nu\beta\beta^*$ decay of ^{136}Xe using data from the KamLAND-Zen 800 experiment, which employs 745 kg of xenon enriched to 91% in ^{136}Xe dissolved in a liquid scintillator detector. The analysis uses 4.3 years of data collected between February 2019 and April 2023, corresponding to an exposure of more than one ton-year of ^{136}Xe . A background model based on Monte Carlo simulations, calibrated with in situ sources, is used to perform a binned maximum likelihood fit in the energy range of 2.5–4.8 MeV. Independent studies are used to constrain key low-energy background components, including ^{11}C from cosmic muon spallation and intrinsic ^{40}K contamination of the inner balloon film, and these constraints are incorporated into the final fit. No statistically significant excess is observed. A 90% confidence level lower limit on the $2\nu\beta\beta^*$ half-life is derived using the Feldman–Cousins method, yielding $T_{1/2} > 4.25 \times 10^{24}$ yr. This result represents a preliminary but potentially world-leading constraint and demonstrates the sensitivity of KamLAND-Zen 800 to excited-state double beta decay.

Contents

1	Introduction	1
2	Theory of Neutrinos and Double Beta Decay	5
2.1	Neutrinos in the Standard Model	5
2.1.1	Neutrino Interactions	6
2.2	Neutrino Oscillations	9
2.3	Neutrino Mass	15
2.3.1	Dirac Masses	17
2.3.2	Majorana Neutrino Mass	18
2.3.3	Seesaw Mechanism	21
2.3.4	Lepton Number Violation and Leptogenesis	23
2.4	Double Beta Decay	25
2.5	Two-Neutrino Double Beta Decay	26
2.6	Neutrinoless Double Beta Decay	31
2.7	Double Beta Decay to Excited States	39
2.8	Double Beta Decay Experiments	43
3	The KamLAND-Zen Experiment	47
3.1	KamLAND	47
3.1.1	Liquid Scintillator Targets	52
3.1.2	KamLAND-Zen and XeLS	54
3.2	Chemical Handling Infrastructure	54
3.2.1	Water Extraction	55

3.2.2	Distillation	56
3.2.3	Xenon Handling	58
3.3	Data Acquisition	59
3.3.1	KamLAND DAQ	59
3.3.2	KamFEE DAQ	60
3.3.3	MoGURA	62
3.4	KamLAND-Zen Phases	63
3.4.1	KamLAND-Zen 400	63
3.4.2	KamLAND-Zen 800	65
3.4.3	KamLAND2-Zen	69
4	Event Reconstruction and Selection	72
4.1	Analysis Framework	73
4.1.1	Data Flow	73
4.2	Event Reconstruction	76
4.2.1	Waveform Analysis	76
4.2.2	PMT Corrections	78
4.2.3	Primary Vertex Fitter	80
4.2.4	Secondary Vertex Fitter	81
4.2.5	Energy Reconstruction	82
4.2.6	Muon Reconstruction	86
4.2.7	MoGURA Neutron Reconstruction	90
4.2.8	Muon–Neutron Correlation	92
4.3	Event Selection	94
4.3.1	Unphysical and Bad Quality Event Rejection	95
4.4	Background Rejection	99
4.4.1	Uranium/Thorium	99

4.4.2	Antineutrinos	105
4.4.3	Short-lived Spallation Products	106
4.4.4	Shower Veto	108
4.4.5	Xenon Spallation Products	111
4.4.6	Signal Inefficiency	117
5	Detector Calibration and MC Tuning	119
5.1	Detector Calibration	119
5.1.1	Variation of Energy Scale Over Time	120
5.1.2	MoGURA Stability	123
5.2	MC Tuning	126
5.2.1	Geant4 (KLG4)	126
5.2.2	FLUKA	132
6	Backgrounds	137
6.1	$2\nu\beta\beta$: Double-Beta Decay	138
6.2	Radioactive Contamination	139
6.2.1	^{238}U Series	139
6.2.2	^{232}Th Series	140
6.2.3	^{40}K	140
6.2.4	^{85}Kr	144
6.3	Carbon Spallation	144
6.3.1	Short-Lived Spallation Products	145
6.3.2	^{11}C Spallation Estimation	147
6.3.3	^{137}Xe	150
6.4	Long-Lived Xenon Spallation Products	151
6.4.1	FLUKA Simulation	152
6.4.2	ENSDF Database	153

6.4.3	Spectrum Distortion	154
6.5	Other Backgrounds	155
6.5.1	External Gamma Rays	155
6.5.2	Solar Neutrinos	157
7	$2\nu\beta\beta^*$ Analysis	159
7.1	Xenon Enrichment in KamLAND-Zen	159
7.2	Full KamLAND-Zen 800 Dataset	160
7.2.1	Vetoed Data Periods	160
7.3	Systematic Uncertainties	161
7.4	Spectral Fit	161
7.4.1	Likelihood (NLL) Definition	162
7.4.2	Model Prediction per Energy Bin	163
7.4.3	Minimization and Fit Configuration	163
7.5	$2\nu\beta\beta^*$ Results	165
7.5.1	Best-Fit Result	165
7.5.2	$2\nu\beta\beta^*$ Half-life Limits	166
7.5.3	Validity of Wilks' Theorem	169
7.5.4	Feldman–Cousins Calculation	170
7.5.5	Discussion	171
8	Conclusion	174
References		178
Curriculum Vitae		189

List of Tables

2.1	Weak isospin I , third component of weak isospin I_3 , hypercharge Y , and electric charge $Q = I_3 + Y/2$ for fermion doublets and singlets in the Standard Model.	7
2.2	Best-fit values $\pm 1\sigma$ from a global analysis of neutrino oscillation parameters reproduced from NuFIT version 6.0.	14
3.1	Composition and physical properties of the KamLAND liquid scintillator (KamLS).	53
3.2	Chemical composition of the xenon-loaded liquid scintillator (XeLS) for the different phases of the KamLAND-Zen experiment.	55
3.3	Balloon film contamination levels from the last three phases of KamLAND-Zen.	68
4.1	Systematic uncertainties associated with FLUKA-based simulations of long-lived spallation backgrounds.	117
4.2	Summary of deadtime contributions from background rejection vetoes.	118
5.1	Summary of the radioactive calibration sources.	127
5.2	FLUKA physics processes enabled in the spallation simulation.	133
5.3	Breakdown of ^{136}Xe spallation products.	136
6.1	Fit parameter configuration for the ^{40}K spectral analysis.	143
6.2	Production and background rate of carbon spallation products.	146
6.3	Sources of uncertainty in the ^{11}C production rate calculation.	150

7.1	Enriched xenon composition used in this analysis.	160
7.2	Fit parameter configuration for the spectral analysis. The fit condition column indicates whether parameters are free, fixed, scanned, or constrained in the fit.	164
7.3	The best fit parameter values and their fit conditions.	167

List of Figures

2.1	Atomic masses of $A = 136$ isotopes.	29
2.2	Depiction of the $0\nu\beta\beta$ black box theorem, the black box represents an arbitrary $0\nu\beta\beta$ process, which can be used to convert antineutrinos into neutrinos.	32
2.3	Feynman diagrams for $2\nu\beta\beta$ decay (Left) and $0\nu\beta\beta$ decay (Right). . .	33
2.4	Possible Majorana masses for normal (magenta) and inverted (blue) mass orderings, calculated with mixing angles and mass differences from the PMNS matrix.	34
2.5	Results from various NME calculation of $M_{0\nu}$ on particular $0\nu\beta\beta$ decaying isotopes versus atomic mass.	38
2.6	Predictions of $T_{1/2}^{2\nu^*}$ using various NME calculation methods. . . .	40
2.7	Radial distributions of $0\nu\beta\beta$ (top) and $2\nu\beta\beta$ (bottom) NMEs of ${}^{76}\text{Ge}$ obtained via pnQRPA.	42
2.8	Correlation of $2\nu\beta\beta$ and $0\nu\beta\beta$ NME as calculated by NSM (Nuclear Shell Model) and pnQRPA (proton-neutron quasiparticle random-phase approximation) methods.	43
2.9	Effective Majorana neutrino mass as a function of the lightest neutrino mass state $m_{lightest}$	45
2.10	EXO-200's fit over energy spectrum (Left) and particle ID discriminator spectrum (Right) in two data-taking phases of the excited state signal and background.	46

3.1	Illustration of the KamLAND site.	48
3.2	KamLAND-Zen detector.	49
3.3	Schematics of the 17-inch and 20-inch PMTs.	50
3.4	Quantum Efficiency of the KamLAND inner PMTs and PPO emission over wavelength.	52
3.5	Flow diagram of the water extraction and nitrogen purge system.	56
3.6	Flow diagram of the KLZ distillation and circulation system.	57
3.7	Flow diagram of the KLZ Xenon system.	60
3.8	Flow diagram of the KamLAND data acquisition system.	61
3.9	Inner balloon structure and measurements for KamLAND-Zen 800 configuration.	67
3.10	Coincidence event rate in KamLAND-Zen 800 during the first distillation campaign, second distillation campaign, and xenon loading phase.	68
4.1	Data flow in KamLAND from raw waveforms to analysis variables such as energy, vertex, and total hit PMTs.	73
4.2	Example of waveform analysis.	77
4.3	Trend in the number of low-gain 17-inch PMTs prior to KamLAND-Zen 800.	79
4.4	Example PMT hit-time distribution from data run 14783.	80
4.5	Probability density functions of 17-inch and 20-inch PMT hit-time residuals derived from calibration data.	82
4.6	Fit of the no-hit probability as a function of expected charge μ for a low-gain PMT.	87
4.7	A schematic illustration of cosmic-ray muon reconstruction in the KamLAND detector, showing how the muon entrance and exit points are estimated using PMT information.	90

4.8	Time residual distribution for a neutron capture event recorded by MoGURA, illustrating contributions from genuine scintillation light and fake PMT after-pulses.	92
4.9	Muon–neutron correlation using MoGURA data.	95
4.10	Event display of a PMT flasher event.	96
4.11	<code>Nhit17</code> versus <code>NsumMax</code> distributions for all physics events (Left) and ^{214}Bi -tagged events (Right).	98
4.12	Badness distributions for all physics events (Left) and ^{214}Bi -tagged events (Right).	99
4.13	Delayed-coincidence selection parameter distributions for ^{214}Bi	101
4.14	Delayed-coincidence selection parameter distributions for ^{212}Bi	102
4.15	Selection criteria in the $(E_d, \Delta T)$ plane used to identify pileup events.	105
4.16	Schematic illustration of the spallation veto strategy using MoGURA-tagged neutrons for carbon- and xenon-based spallation products.	109
4.17	Schematic illustration of photon production along a cosmic-ray muon track and the geometry used for dE/dX reconstruction.	111
4.18	Example of a reconstructed dE/dX distribution along a muon track.	112
4.19	Spatial distributions and weighting functions used in the ENN calculation.	113
4.20	Two-dimensional likelihood PDFs in (dR, ENN) space for spallation and accidental hypotheses.	115
4.21	Log-likelihood ratio distributions generated using toy Monte Carlo simulations, demonstrating clear separation between spallation and accidental hypotheses.	115
4.22	Figure of Merit used to determine the optimal likelihood ratio threshold for long-lived spallation background separation.	116

5.1	Time variation of ^{40}K peak after correction.	120
5.2	Neutron capture energy over KLZ-800 data-taking.	122
5.3	The event rate in the $2\nu\beta\beta$ dominant energy region over KLZ-800 data-taking.	123
5.4	Time evolution of the neutron capture rate and neutron tagging efficiency measured by MoGURA over KamLAND-Zen 800 data-taking.	124
5.5	Characteristic distributions of ^{10}C decay candidates.	125
5.6	Time evolution of the ^{10}C decay rate (Left) and the shape of the dR distribution (Right) over KamLAND-Zen 800 data-taking.	126
5.7	N_{hit} and total charge distributions from source calibration data.	128
5.8	Position dependence of the total charge peak for each calibration source isotope.	129
5.9	Radius dependence of the total collected charge for ^{214}Po α decays.	130
5.10	$\Delta\chi^2$ scan over Birks' constant k_B and the Cherenkov-to-scintillation ratio R	131
5.11	Tuned ^{214}Bi β -decay energy spectrum and spatial correlation of delayed-coincidence Bi–Po decays.	132
5.12	Simulated energy spectra of ^{136}Xe spallation products including their decay chain.	134
5.13	Comparison of tuned FLUKA simulations (red curves) and data (black points) for the ^{10}C dR (Left) and ENN (Right) distributions.	135
6.1	An example ^{40}K fit performed at $r = 15 \text{ m}^3$, outside the IB.	142
6.2	The fitted ^{40}K radial distribution.	142
6.3	The fit to short-lived spallation backgrounds over Energy and dT	146
6.4	Distribution of dT (time delay from muon to event) for muon-event pairs passing all selection cuts, shown separately for KamLS and XeLS.	148

6.5	Subtracted energy distributions compared to MC ^{11}C in XeLS and KamLS.	149
6.6	The fit to short-lived spallation backgrounds over Energy and dT	151
6.7	Production rates of spallation nuclei in KamLAND-Zen XeLS.	153
6.8	Comparison between FLUKA predictions and xenon beam data constraints.	155
6.9	Characterization of external gamma-ray backgrounds in KamLAND-Zen.	156
6.10	Energy spectra of solar neutrino fluxes.	157
6.11	Modeled solar neutrino backgrounds included in the excited-state analysis, including ^8B elastic scattering and ^{136}Cs beta decay.	158
7.1	Best-fit energy spectrum for the full KamLAND-Zen 800 dataset in the reduced fiducial volume $r < 1.33$ m.	166
7.2	Difference in the NLL test statistic as a function of fixed $2\nu\beta\beta^*$ signal rate.	168
7.3	Feldman–Cousins analysis results.	171
7.4	A comparison of experimental lower limits on the $2\nu\beta\beta^*$ decay half-life to the 0_1^+ excited state in ^{136}Xe and selected theoretical predictions. .	172

List of Abbreviations

$0\nu\beta\beta$	Neutrinoless Double-Beta Decay
$2\nu\beta\beta$	Two-Neutrino Double-Beta Decay
ATWD	Analog Transient Waveform Digitizer
DAQ	Data Acquisition
ENSDF	Evaluated Nuclear Structure Data File
FBE	Fast Bus Electronics
FV	Fiducial Volume
GEANT4	Geometry and Tracking 4 (MC simulation toolkit)
GVF	General Vector File
IB	Inner Balloon
IBD	Inverse Beta Decay
ID	Inner Detector
KamFEE	KamLAND Front-End Electronics
KamLAND	Kamioka Liquid Scintillator Antineutrino Detector
KamLS	KamLAND Liquid Scintillator
KDF	Kinoko Data Format
KLG4Sim	KamLAND GEANT4 Simulation Framework
LS	Liquid Scintillator
MC	Monte Carlo
MNVF	Muon-Neutron Vector File
MoGURA	Module for General-Use Rapid Application
NHIT	Number of Hit Photomultiplier Tubes
OD	Outer Detector
OB	Outer Balloon
PEN	Polyethylene Naphthalate
PMT	Photomultiplier Tube
PPO	2,5-Diphenyloxazole
QE	Quantum Efficiency
ROI	Region of Interest
RTQ	Raw Time and Charge
TQ	Time and Charge
XeLS	Xenon-Loaded Liquid Scintillator

Chapter 1

Introduction

One of the most striking features of the universe is that it exists in a form capable of forming stars, planets, and ultimately life. This fact alone points to a deep asymmetry in nature: matter is abundant, while antimatter is almost entirely absent. In the early universe, following the Big Bang, energy was readily converted into particle–antiparticle pairs under extreme temperatures and densities. According to the known laws of physics, these processes should have produced matter and antimatter in equal quantities, leading to their mutual annihilation as the universe cooled. The survival of matter therefore signals that a subtle but fundamental imbalance must have emerged during the universe’s earliest moments, the origin of which remains one of the central open questions in modern physics.

The existence of this imbalance implies that the fundamental symmetries governing particle interactions are not exact. In particular, charge–parity (CP) symmetry determines whether the laws of physics treat matter and antimatter in the same way. Although CP violation has been observed in the quark sector, its measured effects within the Standard Model are far too weak to account for the matter dominance inferred from cosmological observations. This gap between theory and observation suggests that additional sources of CP violation, or entirely new particles and interactions, played a role in shaping the universe we observe today.

Neutrinos offer a compelling window into this missing physics. Unlike other fermions in the Standard Model, neutrinos are exceptionally light, weakly interact-

ing, and exhibit properties that already require physics beyond the Standard Model. Many theoretical frameworks link these unusual features to the origin of the cosmic matter asymmetry through the mechanism of leptogenesis. In such scenarios, CP-violating processes involving heavy neutrino states in the early universe generate an excess of leptons over antileptons, which is later converted into a baryon asymmetry by electroweak interactions. A key ingredient in many of these models is that neutrinos are Majorana particles, identical to their own antiparticles. This possibility can be tested experimentally through the search for neutrinoless double beta decay ($0\nu\beta\beta$), a rare nuclear process whose observation would reveal lepton number violation and provide direct evidence for the Majorana nature of neutrinos and for new physics beyond the Standard Model.

Neutrinoless double beta decay ($0\nu\beta\beta$) is a hypothetical nuclear transition in which two neutrons decay into two protons and two electrons without the emission of neutrinos. If observed, this process would demonstrate the violation of lepton number and provide a direct link between nuclear decay rates and fundamental neutrino properties. While experimental searches for $0\nu\beta\beta$ continue to improve in sensitivity, the interpretation of any observed signal, or increasingly stringent null result, depends critically on the reliability of nuclear matrix element calculations.

At present, theoretical predictions for the nuclear matrix elements governing $0\nu\beta\beta$ differ substantially among nuclear-structure approaches, leading to significant uncertainties in the inferred neutrino mass scale. Reducing these uncertainties is therefore essential for fully realizing the physics potential of $0\nu\beta\beta$ experiments. One promising avenue for constraining nuclear matrix element calculations is provided by measurements of Standard Model two-neutrino double beta decay ($2\nu\beta\beta$), which serve as important benchmarks for nuclear theory. In addition to the well-studied decays to the ground state of the daughter nucleus, double beta decay can also proceed to ex-

cited nuclear states. Although such excited-state transitions are strongly suppressed by reduced phase space, they probe complementary aspects of nuclear structure and provide additional experimental constraints on the models used to calculate $0\nu\beta\beta$ nuclear matrix elements.

In particular, $2\nu\beta\beta$ to excited states of the daughter nucleus ($2\nu\beta\beta^*$) offers a unique opportunity to test nuclear-structure calculations beyond the single ground-state transition. These decays involve different combinations of nuclear wave-function components and intermediate-state contributions, and are accompanied by characteristic gamma-ray cascades as the daughter nucleus de-excites. As a result, excited-state decays provide sensitivity to modeling assumptions that may not be fully constrained by ground-state $2\nu\beta\beta$ data alone. Experimental information on these suppressed channels can therefore help discriminate among competing nuclear models and reduce the spread of predicted $0\nu\beta\beta$ nuclear matrix element calculations.

This thesis focuses on a search for double beta decay of ^{136}Xe to excited states of ^{136}Ba using data from the KamLAND-Zen 800 experiment. Owing to the extreme rarity of these processes and the presence of substantial radioactive and instrumental backgrounds, such a search is inherently challenging. The analysis is sensitive primarily to the most dominant excited-state decay modes and is largely agnostic to the specific excited state involved. Rather than targeting a particular transition, the search is designed to address a more fundamental question: whether any statistically significant indication of excited-state double beta decay can be observed in the available dataset. Establishing an observation, or setting improved limits in the absence of a signal, provides valuable new experimental input for nuclear matrix element calculations and strengthens the interpretation of ^{136}Xe -based searches for $0\nu\beta\beta$.

The remainder of this dissertation is organized as follows. Chapter 2 reviews the

theoretical framework of neutrinos, neutrino mass, and double beta decay, with emphasis on the relationship between two-neutrino and neutrinoless modes and their associated nuclear matrix elements. Subsequent Chapters 3 – 7 describe the KamLAND-Zen detector and dataset, the modeling of signal and background processes, the analysis techniques used to search for excited-state decays, and the resulting constraints and their implications for nuclear theory and future $0\nu\beta\beta$ sensitivity.

Chapter 2

Theory of Neutrinos and Double Beta Decay

While this chapter reviews the theoretical foundations of neutrino mass and lepton number violation, particular emphasis is placed on Standard Model two-neutrino double beta decay ($2\nu\beta\beta$). In addition to serving as an irreducible background to neutrinoless double beta decay ($0\nu\beta\beta$) searches, $2\nu\beta\beta$ to excited nuclear states provides a unique experimental probe of nuclear structure that directly informs the interpretation of $0\nu\beta\beta$ results.

2.1 Neutrinos in the Standard Model

Neutrinos remain the least understood component of the Standard Model (SM) of particle physics. Their elusive nature and extremely weak interactions make them challenging to study, yet they play a central role in both particle physics and cosmology. The modern understanding of neutrinos began in 1914, when James Chadwick used magnetic spectrometry to measure the energy spectrum of electrons emitted in beta decay. He observed that the spectrum was continuous rather than discrete, implying an apparent violation of energy conservation.

To resolve this puzzle, Pauli postulated in 1930 the existence of a new neutral and very light particle that carried away the missing energy [1]. He introduced this idea in his famous letter addressed to the “Radioactive Ladies and Gentlemen.” Enrico Fermi later incorporated Pauli’s proposal into his theory of beta decay and named the

particle the neutrino, meaning “little neutral one.” The neutrino was experimentally detected in 1956 by Cowan and Reines [2], firmly establishing its existence. Since that time, the Standard Model has been extended to include three flavors of neutrinos, each associated with a corresponding charged lepton.

The Standard Model is a gauge theory based on the symmetry group $SU(3)_C \times SU(2)_L \times U(1)_Y$ [3, 4, 5, 6, 7]. Neutrinos participate only in the weak interaction, which is mediated by the charged W^\pm bosons and the neutral Z^0 boson, and they carry no electric charge. Their extremely small interaction cross sections make them difficult to detect, but also allow them to propagate over vast distances with little attenuation. This unique property enables neutrinos to serve as powerful messengers from otherwise inaccessible regions of the universe.

2.1.1 Neutrino Interactions

The Standard Model unifies the strong, weak, and electromagnetic interactions within the gauge symmetry $SU(3)_C \times SU(2)_L \times U(1)_Y$. The $SU(3)_C$ sector governs the strong interaction through quantum chromodynamics, while the $SU(2)_L \times U(1)_Y$ sector describes the electroweak interaction. In this framework, the weak interaction is mediated by the charged W^\pm bosons and the neutral Z^0 boson.

Neutrinos appear in the Standard Model as components of left handed lepton doublets, which transform as weak isospin doublets under $SU(2)_L$:

$$L_\ell = \begin{pmatrix} \nu_{\ell L} \\ \ell_L \end{pmatrix}, \quad \ell = e, \mu, \tau. \quad (2.1)$$

Here, $\nu_{\ell L}$ and ℓ_L denote the neutrino and charged lepton fields of flavor ℓ , respectively. Only the left handed components of these fermion fields participate in weak interactions. This chiral structure is implemented through the projection operator:

$$P_L = \frac{1 - \gamma_5}{2}, \quad (2.2)$$

where $\gamma_5 = i\gamma^0\gamma^1\gamma^2\gamma^3$ is constructed from the Dirac matrices.

Electroweak interactions are characterized by two quantum numbers: weak isospin I and weak hypercharge Y . The electric charge operator is given by:

$$Q = I_3 + \frac{Y}{2}, \quad (2.3)$$

where I_3 is the third component of weak isospin. For lepton doublets, the total weak isospin is $I = 1/2$ and the hypercharge is $Y = -1$. These assignments correctly reproduce the observed electric charges, yielding $Q = 0$ for neutrinos and $Q = -1$ for charged leptons.

Table 2.1 summarizes the weak isospin, hypercharge, and electric charge assignments for the fermion doublets and singlets in the Standard Model. Right handed charged leptons and quarks are singlets under $SU(2)_L$, with $I = 0$, and therefore do not participate in charged weak interactions. Their hypercharge values are chosen to reproduce the observed electric charges through Eq. 2.3.

The neutrino components of the lepton doublets are referred to as active neutrinos, reflecting their participation in weak interactions. In contrast, hypothetical sterile

		I	I_3	Y	Q
lepton doublet	$L_L \equiv \begin{pmatrix} \nu_{eL} \\ e_L \end{pmatrix}$	1/2 1/2	+1/2 -1/2	-1 -1	0 -1
lepton singlet	e_R	0	0	-2	-1
quark doublet	$Q_L \equiv \begin{pmatrix} u_L \\ d_L \end{pmatrix}$	1/2 1/2	+1/2 -1/2	1/3 1/3	2/3 -1/3
quark singlets	u_R d_R	0 0	0 -2/3	4/3 -2/3	2/3 -1/3

Table 2.1: Weak isospin I , third component of weak isospin I_3 , hypercharge Y , and electric charge $Q = I_3 + Y/2$ for fermion doublets and singlets in the Standard Model.

neutrinos would be singlets under the full Standard Model gauge group and would not couple to the W^\pm or Z^0 bosons. Within the Standard Model, there is exactly one active neutrino associated with each charged lepton flavor: e , μ , and τ .

Gauge invariance under $SU(2)_L$ dictates the form of the weak charged current and neutral current interactions involving leptons. These interactions are described by the Lagrangian terms:

$$-\mathcal{L}_{\text{CC}} = \frac{g}{\sqrt{2}} \sum_{\ell} \bar{\nu}_{\ell L} \gamma^\mu \ell_L W_\mu^+ + \text{h.c.}, \quad (2.4)$$

$$-\mathcal{L}_{\text{NC}} = \frac{g}{2 \cos \theta_W} \sum_{\ell} \bar{\nu}_{\ell L} \gamma^\mu \nu_{\ell L} Z_\mu^0, \quad (2.5)$$

where g is the weak coupling constant and θ_W is the Weinberg angle. The charged current interaction governs processes such as beta decay and double beta decay, while the neutral current interaction allows neutrinos to scatter elastically from matter without changing flavor.

Precision measurements of the invisible decay width of the Z^0 boson provide a direct constraint on the number of light, active neutrino species [8]. The experimentally measured value,

$$N_\nu = 2.984 \pm 0.008, \quad (2.6)$$

is consistent with three active neutrino flavors and provides strong experimental support for the Standard Model neutrino sector.

The purely left handed nature of weak interactions in the Standard Model has important consequences for neutrino mass and for processes that violate lepton number. Because only left handed neutrino fields appear in the electroweak Lagrangian, no renormalizable mass term for neutrinos can be constructed using Standard Model fields alone. As a result, neutrinos are massless in the minimal Standard Model. Any mechanism that generates neutrino mass must therefore extend the theory, either

by introducing new fields or by allowing higher dimensional operators. This chiral structure also plays a central role in double beta decay. In particular, the connection between left handed weak currents, neutrino mass, and lepton number violation underlies the theoretical interpretation of both $2\nu\beta\beta$ and $0\nu\beta\beta$ decay processes, which are discussed in detail in the following sections.

2.2 Neutrino Oscillations

The discovery of neutrino oscillations represents one of the most significant breakthroughs in particle physics in recent decades. This achievement was recognized with the 2015 Nobel Prize in Physics, awarded to Art McDonald of the SNO collaboration and Takaaki Kajita of the Super-Kamiokande collaboration [9]. The underlying concept of neutrino flavor oscillations was first proposed by Bruno Pontecorvo in the late 1950s, inspired by the phenomenon of neutral kaon mixing, $K^0 \leftrightarrow \bar{K}^0$ [10]. Pontecorvo suggested that neutrinos, like kaons, could change identity as they propagate, provided that the states produced in weak interactions were not identical to the states of definite mass.

Neutrino oscillations arise from the misalignment between flavor eigenstates and mass eigenstates. In a weak interaction, a neutrino is produced in a definite flavor state, associated with a charged lepton of the same flavor. However, the flavor eigenstates $|\nu_\alpha\rangle$, with $\alpha = e, \mu, \tau$, are quantum superpositions of mass eigenstates $|\nu_k\rangle$, where $k = 1, 2, 3$:

$$|\nu_\alpha\rangle = \sum_k U_{\alpha k}^* |\nu_k\rangle. \quad (2.7)$$

This relationship may also be written in matrix form as:

$$\begin{pmatrix} \nu_e \\ \nu_\mu \\ \nu_\tau \end{pmatrix} = \begin{pmatrix} U_{e1} & U_{e2} & U_{e3} \\ U_{\mu 1} & U_{\mu 2} & U_{\mu 3} \\ U_{\tau 1} & U_{\tau 2} & U_{\tau 3} \end{pmatrix} \begin{pmatrix} \nu_1 \\ \nu_2 \\ \nu_3 \end{pmatrix}, \quad (2.8)$$

where the coefficients $U_{\alpha k}$ are elements of the Pontecorvo-Maki-Nakagawa-Sakata (PMNS) matrix.

The PMNS matrix is parameterized by three mixing angles, θ_{12} , θ_{23} , and θ_{13} , a Dirac charge parity violating phase δ_{CP} , and two additional phases ξ_1 and ξ_2 that appear if neutrinos are Majorana particles. A commonly used parameterization of the PMNS matrix is:

$$U = \begin{pmatrix} 1 & 0 & 0 \\ 0 & \cos \theta_{23} & \sin \theta_{23} \\ 0 & -\sin \theta_{23} & \cos \theta_{23} \end{pmatrix} \begin{pmatrix} \cos \theta_{13} & 0 & \sin \theta_{13} e^{-i\delta_{CP}} \\ 0 & 1 & 0 \\ -\sin \theta_{13} e^{i\delta_{CP}} & 0 & \cos \theta_{13} \end{pmatrix} \times \begin{pmatrix} \cos \theta_{12} & \sin \theta_{12} & 0 \\ -\sin \theta_{12} & \cos \theta_{12} & 0 \\ 0 & 0 & 1 \end{pmatrix} \begin{pmatrix} 1 & 0 & 0 \\ 0 & e^{i\xi_1} & 0 \\ 0 & 0 & e^{i\xi_2} \end{pmatrix}. \quad (2.9)$$

The final diagonal matrix containing the Majorana phases does not affect neutrino oscillation probabilities, as these phases cancel when forming the inner products relevant for flavor transitions. Nevertheless, they play a crucial role in lepton number violating processes such as $0\nu\beta\beta$ decay and therefore remain of central interest in neutrino physics.

To illustrate how neutrino oscillation parameters are extracted experimentally, it

is instructive to derive the oscillation probability in vacuum. Unlike quarks, which are confined within hadrons, neutrinos propagate freely over macroscopic distances. The massive neutrino states $|\nu_k\rangle$ can therefore be treated as plane wave solutions to the Schrödinger equation, evolving in time as:

$$|\nu_k(t)\rangle = e^{-iE_k t} |\nu_k\rangle, \quad E_k = \sqrt{m_k^2 + \vec{p}^2}. \quad (2.10)$$

A neutrino produced at time $t = 0$ in a flavor state $|\nu_\alpha\rangle$ evolves as a coherent superposition of mass eigenstates,

$$|\nu_\alpha(t)\rangle = \sum_k U_{\alpha k}^* e^{-iE_k t} |\nu_k\rangle. \quad (2.11)$$

Using the unitarity of the PMNS matrix, $U^\dagger U = \mathbb{1}$, this expression may be rewritten in the flavor basis as:

$$|\nu_\alpha(t)\rangle = \sum_{\beta=e,\mu,\tau} \left(\sum_k U_{\alpha k}^* e^{-iE_k t} U_{\beta k} \right) |\nu_\beta\rangle. \quad (2.12)$$

The probability that a neutrino produced in flavor state ν_α is later detected as flavor ν_β is then given by:

$$P(\nu_\alpha \rightarrow \nu_\beta) = |\langle \nu_\beta | \nu_\alpha(t) \rangle|^2 = \sum_{k,j} U_{\alpha k}^* U_{\beta k} U_{\alpha j} U_{\beta j}^* e^{-i(E_k - E_j)t}. \quad (2.13)$$

For ultra relativistic neutrinos, where $m_k \ll |\vec{p}|$, the energy may be expanded as:

$$E_k \simeq E + \frac{m_k^2}{2E}, \quad (2.14)$$

leading to

$$E_k - E_j = \frac{\Delta m_{kj}^2}{2E}, \quad \Delta m_{kj}^2 \equiv m_k^2 - m_j^2. \quad (2.15)$$

Since oscillation experiments measure the source detector separation L rather than the

propagation time, the approximation $t \simeq L$ may be used. The oscillation probability then becomes:

$$P(\nu_\alpha \rightarrow \nu_\beta) = \sum_{k,j} U_{\alpha k}^* U_{\beta k} U_{\alpha j} U_{\beta j}^* e^{-i\Delta m_{kj}^2 L/2E}. \quad (2.16)$$

Separating the real and imaginary components yields the familiar form:

$$\begin{aligned} P(\nu_\alpha \rightarrow \nu_\beta) &= \delta_{\alpha\beta} - 4 \sum_{k>j} \Re [U_{\alpha k}^* U_{\beta k} U_{\alpha j} U_{\beta j}^*] \sin^2 \left(\frac{\Delta m_{kj}^2 L}{4E} \right) \\ &\quad + 2 \sum_{k>j} \Im [U_{\alpha k}^* U_{\beta k} U_{\alpha j} U_{\beta j}^*] \sin \left(\frac{\Delta m_{kj}^2 L}{2E} \right). \end{aligned} \quad (2.17)$$

The oscillation amplitudes are governed by the elements of the PMNS matrix, while the oscillation frequency is set by the ratio $\Delta m_{kj}^2 L/E$. In practical units, this phase may be written as:

$$\frac{\Delta m_{kj}^2 L}{2E} \approx 1.27 \frac{\Delta m_{kj}^2 [\text{eV}^2] L [\text{km}]}{E [\text{GeV}]} \quad (2.18)$$

Within the past two decades, the majority of neutrino oscillation parameters have been measured with impressive precision. The three mixing angles θ_{12} , θ_{23} , and θ_{13} , along with the two independent squared mass splittings Δm_{21}^2 and $|\Delta m_{31}^2|$, are now known to the level of a few percent or better. These measurements have been achieved using a diverse set of experiments that study neutrinos originating from the Sun, the Earth's atmosphere, nuclear reactors, and particle accelerators.

Despite this progress, two fundamental questions remain unresolved within the oscillation framework. The first concerns the value of the charge parity violating phase δ_{CP} , which governs potential differences between neutrino and antineutrino oscillation probabilities. The second is the ordering of the neutrino mass eigenstates, commonly referred to as the neutrino mass hierarchy.

Because oscillation experiments are sensitive only to differences in squared masses, they cannot determine the absolute neutrino mass scale. As a result, two distinct mass

orderings remain consistent with current data. In the normal ordering scenario, the third mass eigenstate is the heaviest, with $m_3 > m_2 > m_1$. In the inverted ordering scenario, the third mass eigenstate is the lightest, with $m_2 > m_1 > m_3$. These two possibilities correspond to opposite signs of the atmospheric mass splitting, Δm_{31}^2 or Δm_{32}^2 , which current experiments have not yet been able to determine conclusively.

Table 2.2 summarizes the current best fit values and one standard deviation uncertainties for the neutrino oscillation parameters, reproduced from the NuFIT version 6.0 global analysis [11]. This fit incorporates data from a wide range of experiments, including atmospheric neutrino measurements from Super-Kamiokande, and provides results for both normal and inverted mass orderings. The solar mass splitting Δm_{21}^2 is common to both orderings, while the atmospheric mass splitting Δm_{3k}^2 differs in sign depending on the assumed hierarchy. In Table 2.2, the notation Δm_{sol}^2 refers to Δm_{21}^2 , while Δm_{atm}^2 denotes either Δm_{31}^2 or Δm_{32}^2 , depending on the ordering. This convention reflects the historical sensitivity of solar neutrino experiments to Δm_{21}^2 and of atmospheric neutrino experiments to $|\Delta m_{31}^2| \approx |\Delta m_{32}^2|$.

Future experiments are expected to resolve the remaining ambiguities in the oscillation framework. Medium baseline reactor experiments such as JUNO [12] aim to determine the mass ordering through precision measurements of oscillation interference effects. Long baseline accelerator experiments, including Hyper-Kamiokande [13] and DUNE [14], are designed to probe both the mass ordering and the value of δ_{CP} through detailed studies of neutrino and antineutrino appearance channels.

Equation 2.17 shows that neutrino oscillation experiments are sensitive only to differences in the squared neutrino masses, Δm_{jk}^2 , and provide no information on the absolute values of the individual mass eigenstates. As a result, determining the absolute neutrino mass scale requires experimental approaches that are complementary to oscillation measurements.

Oscillation parameter	Normal	Inverted
$\Delta m_{21}^2 [10^{-5} \text{ eV}^2]$	$7.49^{+0.19}_{-0.19}$	$7.49^{+0.19}_{-0.19}$
$\Delta m_{3k}^2 [10^{-3} \text{ eV}^2]$	$+2.513^{+0.021}_{-0.019}$	$-2.484^{+0.020}_{-0.020}$
$\sin^2 \theta_{12}$	$0.308^{+0.012}_{-0.011}$	$0.308^{+0.012}_{-0.011}$
$\sin^2 \theta_{23}$	$0.470^{+0.17}_{-0.13}$	$0.550^{+0.012}_{-0.015}$
$\sin^2 \theta_{13}$	$0.02215^{+0.00056}_{-0.00058}$	$0.02231^{+0.00056}_{-0.00056}$
$\delta_{CP} [\circ]$	212^{+26}_{-41}	274^{+22}_{-25}

Table 2.2: Best-fit values $\pm 1\sigma$ from a global analysis of neutrino oscillation parameters reproduced from NuFIT version 6.0 in Reference [11]. Note that $\Delta m_{3k}^2 \equiv \Delta m_{31}^2 > 0$ for normal ordering and $\Delta m_{3k}^2 \equiv \Delta m_{32}^2 < 0$ for inverted ordering.

One such approach is pursued by the KATRIN experiment, which directly probes the kinematics of β decay. KATRIN measures the energy spectrum of electrons emitted in the decay of tritium, which has a Q -value of 18.6 keV. If neutrinos are massive, a small but measurable fraction of the available decay energy is carried away by the neutrino. Precise measurements of the endpoint of the electron energy spectrum therefore place a constraint on the effective mass of the electron flavor neutrino, which is a superposition of the neutrino mass eigenstates,

$$m_{\nu_e} = \sqrt{\sum_i |U_{ei}|^2 m_i^2}. \quad (2.19)$$

Achieving sensitivity to this quantity is experimentally challenging and requires sub electron volt energy resolution near the endpoint of the beta decay spectrum. The most stringent direct limit to date has been set by the KATRIN experiment, which reports $m_{\nu_e} < 0.8 \text{ eV}$ at 90% confidence level [15]. Future experiments, such as

Project 8, aim to further improve this sensitivity using Cyclotron Radiation Emission Spectroscopy, a technique that measures the frequency of radiation emitted by beta decay electrons spiraling in a magnetic field [16].

An alternative, indirect probe of neutrino masses is provided by cosmological observations. Neutrinos influence the formation and evolution of large scale structure in the universe due to their relativistic nature in the early universe and their contribution to the total matter density at later times. Measurements of the Cosmic Microwave Background, Baryon Acoustic Oscillations, and Redshift Space Distortions can therefore be combined to constrain the sum of the neutrino mass eigenstates, $\sum m_i = m_1 + m_2 + m_3$. Currently, the strongest cosmological constraint yields an upper limit of $\sum m_i < 0.09 \text{ eV}$ at 95% confidence level [17].

A third and potentially most sensitive approach to determining the absolute neutrino mass scale involves $0\nu\beta\beta$ decay. Observation of this decay would not only provide access to an effective neutrino mass parameter, but would also demonstrate the violation of lepton number and establish the Majorana nature of neutrinos. Before discussing aspects of $2\nu\beta\beta$ and $0\nu\beta\beta$ decay, we will first review the theoretical framework of neutrino mass generation that motivates and underpins these searches.

2.3 Neutrino Mass

The observation of neutrino oscillations establishes that neutrinos possess nonzero masses and that flavor eigenstates are superpositions of mass eigenstates. Despite this, the underlying mechanism responsible for neutrino mass generation remains unknown. Numerous extensions of the Standard Model have been proposed to explain this phenomenon, as discussed below.

Here we follow the derivation presented in Reference [18]. Landau, Lee and Yang, and independently Salam, showed that a massless fermion can be consistently de-

scribed by a chiral field within a two-component theory of massless neutrinos. We begin with the Dirac equation:

$$(i\gamma^\mu \partial_\mu - m)\psi = 0, \quad (2.20)$$

for a fermion field ψ . Decomposing the Dirac spinor into its left- and right-handed chiral components:

$$\psi = \psi_L + \psi_R, \quad (2.21)$$

where $\psi_{L,R} = P_{L,R}\psi$ and $P_{L,R} = \frac{1}{2}(1 \mp \gamma^5)$ are the chiral projection operators, the Dirac equation can be written as the coupled system:

$$i\gamma^\mu \partial_\mu \psi_L = m\psi_R, \quad (2.22)$$

$$i\gamma^\mu \partial_\mu \psi_R = m\psi_L, \quad (2.23)$$

where the space-time evolution of the left- and right-handed fields is coupled through the mass term m .

In the massless limit, $m = 0$, Eqs. (2.22) and (2.23) decouple:

$$i\gamma^\mu \partial_\mu \psi_L = 0, \quad (2.24)$$

$$i\gamma^\mu \partial_\mu \psi_R = 0. \quad (2.25)$$

In this case, a massless fermion may be fully described by a single chiral field (either left-handed or right-handed) which contains only two independent degrees of freedom. These equations are known as the Weyl equations, and the corresponding spinors ψ_L and ψ_R are referred to as Weyl spinors.

The minimal formulation of the Standard Model adopts this two-component description for neutrinos, treating them as massless fermions. In this framework, the neutrino is described entirely by a left-handed Weyl spinor, ν_L , which participates in

the weak interaction, while no right-handed neutrino field, ν_R , is included.

2.3.1 Dirac Masses

If right-handed neutrino fields ν_R exist, neutrinos may acquire mass through a Dirac mass term analogous to those of the charged leptons. In this case, a Yukawa interaction can be written as:

$$-\mathcal{L}_{\text{Dirac}} = Y_{ij}^\nu \bar{L}_{Li} \tilde{\Phi} \nu_{Rj} + \text{h.c.}, \quad (2.26)$$

where L_{Li} is the left-handed lepton doublet of generation i , $\tilde{\Phi} = i\sigma_2 \Phi^*$ is the conjugate Higgs doublet, and Y_{ij}^ν are the neutrino Yukawa couplings. After electroweak symmetry breaking, when the Higgs field acquires a vacuum expectation value v , this interaction generates Dirac neutrino masses:

$$m_{ij}^\nu = \frac{v}{\sqrt{2}} Y_{ij}^\nu. \quad (2.27)$$

This mechanism is entirely analogous to mass generation for the charged leptons and quarks in the Standard Model, where fermion masses arise through Yukawa couplings to the Higgs field following spontaneous symmetry breaking of the $SU(2)_L \times U(1)_Y$ gauge symmetry. In the unitary gauge, the Higgs doublet may be written as:

$$\Phi = \frac{1}{\sqrt{2}} \begin{pmatrix} 0 \\ v + h \end{pmatrix}, \quad (2.28)$$

where h denotes the physical Higgs boson. Coupling this field (or its conjugate) to left- and right-handed fermion fields yields Dirac mass terms proportional to the Higgs vacuum expectation value, as well as Higgs–fermion interaction terms.

Applying this same mechanism to neutrinos, however, presents two conceptual difficulties. First, right-handed neutrino fields are absent from the minimal Standard Model and must be introduced as gauge-singlet states. Such fields do not participate

in the weak interaction and are therefore often referred to as *sterile* neutrinos. The inclusion of ν_R thus constitutes a minimal extension of the Standard Model.

Second, even if right-handed neutrinos exist and neutrinos are purely Dirac fermions, the observed smallness of neutrino masses poses a naturalness problem. Current experimental constraints require neutrino masses to be below the eV scale, implying Yukawa couplings:

$$Y_{ij}^\nu \lesssim 10^{-12}, \quad (2.29)$$

which are many orders of magnitude smaller than those of the charged fermions. This extreme hierarchy is difficult to justify within the Standard Model framework and stands in sharp contrast to the mass spectrum of the other fermions.

The striking disparity between neutrino masses and those of the charged leptons and quarks strongly suggests the presence of an underlying mechanism that suppresses neutrino masses relative to the electroweak scale. This observation has motivated a wide class of neutrino mass models that extend the Standard Model and generate light neutrino masses in a more natural way. Several such mechanisms are discussed in the following sections.

2.3.2 Majorana Neutrino Mass

Since neutrinos have been experimentally shown to possess nonzero masses, the two-component theory of massless neutrinos is no longer sufficient. In 1937, Majorana proposed an alternative formulation of the Dirac equation in which a massive fermion can be described by a single spinor field rather than independent left- and right-handed components. The key assumption of the Majorana construction is that the right-handed field is not independent, but instead related to the left-handed field by charge conjugation:

$$\psi_R = C \overline{\psi_L}^T, \quad (2.30)$$

where C is the charge conjugation matrix.

Using the properties of the charge conjugation operator and the chiral projection operators, one finds that:

$$P_L(C \bar{\psi}_L^T) = 0, \quad (2.31)$$

which demonstrates that the charge-conjugated left-handed field transforms as a right-handed field. In other words, charge conjugation converts a left-handed Weyl spinor into a right-handed one.

With this identification, the fermion field may be written entirely in terms of a single chiral component:

$$\psi = \psi_L + \psi_L^C, \quad (2.32)$$

where $\psi_L^C \equiv C \bar{\psi}_L^T$. The corresponding equation of motion takes the form:

$$i\gamma^\mu \partial_\mu \psi = m\psi^C, \quad (2.33)$$

where ψ^C denotes the charge-conjugated field. This leads directly to the Majorana condition:

$$\psi = \psi^C, \quad (2.34)$$

which implies that the fermion is identical to its antiparticle.

Equation (2.34) can only be satisfied by electrically neutral fermions. Among the known elementary fermions, only neutrinos meet this criterion, making them unique candidates for Majorana particles. Since neutrinos interact solely through the weak interaction, the overall charge parity of the neutrino field has no observable consequence and may be chosen arbitrarily.

If neutrinos are Majorana particles, neutrinos and antineutrinos are not distinct states but differ only by their helicities. By convention, negative-helicity states are referred to as neutrinos, while positive-helicity states are referred to as antineutrinos.

In the Standard Model framework, the simplest Majorana mass term that can be constructed using only Standard Model fields and respecting gauge symmetries is a lepton-number-violating dimension-five operator:

$$\mathcal{L}_5 = \frac{Z_{ij}^\nu}{\Lambda} (\overline{L}_L^i \tilde{\Phi}) (\tilde{\Phi}^T L_L^j) + \text{h.c.}, \quad (2.35)$$

where Z_{ij}^ν is a dimensionless 3×3 coupling matrix, $\tilde{\Phi} = i\sigma_2 \Phi^*$ is the conjugate Higgs doublet, and Λ denotes the scale of new physics beyond the Standard Model.

After electroweak symmetry breaking, this effective interaction generates a Majorana mass term for the light neutrinos:

$$\mathcal{L}_{M_\nu} = \frac{1}{2} \frac{v^2}{\Lambda} Z_{ij}^\nu \overline{\nu}_{L_i} \nu_{L_j}^C + \text{h.c.}, \quad (2.36)$$

corresponding to the Majorana neutrino mass matrix:

$$\mathcal{M}_\nu = Z_{ij}^\nu \frac{v^2}{\Lambda}. \quad (2.37)$$

Compared to the renormalizable Dirac mass terms of the charged fermions, this effective operator contains two Higgs fields and is therefore of mass dimension five. As a result, it is non-renormalizable and must be interpreted as a low-energy manifestation of new physics at the scale Λ . Notably, this operator is the only dimension-five operator that can be constructed within the Standard Model field content and gauge symmetries to generate neutrino masses.

The suppression factor v^2/Λ naturally explains the smallness of neutrino masses if Λ lies far above the electroweak scale. This structure mirrors the mass suppression obtained in seesaw mechanisms, which provide explicit ultraviolet completions of the effective operator in Eq. (2.35). These mechanisms are discussed in the following section.

2.3.3 Seesaw Mechanism

We now discuss an extension of the Standard Model that naturally generates light active neutrino masses through the introduction of one or more heavy sterile neutrinos. Adding m sterile neutrino fields, ν_{si} ($i = 1, \dots, m$), allows for two distinct types of neutrino mass terms. The most general neutrino mass Lagrangian can be written as:

$$-\mathcal{L}_{M_\nu} = M_{D_{ij}} \bar{\nu}_{si} \nu_{Lj} + \frac{1}{2} M_{N_{ij}} \bar{\nu}_{si} \nu_{sj}^c + \text{h.c.}, \quad (2.38)$$

where M_D is a complex $m \times 3$ Dirac mass matrix and M_N is a complex symmetric $m \times m$ Majorana mass matrix.

The first term in Eq. (2.38) corresponds to a Dirac mass term, generated after electroweak symmetry breaking through Yukawa couplings between the sterile neutrinos, the left-handed lepton doublets, and the Higgs field:

$$Y_{ij}^\nu \bar{\nu}_{si} \tilde{\Phi}^\dagger L_{Lj} \Rightarrow M_{D_{ij}} = Y_{ij}^\nu \frac{v}{\sqrt{2}}. \quad (2.39)$$

The second term is a Majorana mass term for the sterile neutrinos and violates lepton number by two units.

Equation (2.38) may be rewritten in matrix form as:

$$-\mathcal{L}_{M_\nu} = \frac{1}{2} \begin{pmatrix} \bar{\nu}_L & \bar{\nu}_s \end{pmatrix} \begin{pmatrix} 0 & M_D^T \\ M_D & M_N \end{pmatrix} \begin{pmatrix} \nu_L^c \\ \nu_s^c \end{pmatrix} + \text{h.c.}, \quad (2.40)$$

where $\vec{\nu} = (\bar{\nu}_L, \bar{\nu}_s^c)^T$ is a $(3+m)$ -dimensional vector. The full neutrino mass matrix M_ν is complex and symmetric, and may be diagonalized by a unitary transformation:

$$(V^\nu)^T M_\nu V^\nu = \text{diag}(m_1, m_2, \dots, m_{3+m}), \quad (2.41)$$

with the corresponding mass eigenstates given by:

$$\vec{\nu}_{\text{mass}} = (V^\nu)^\dagger \vec{\nu}. \quad (2.42)$$

In terms of the mass eigenstates, the neutrino mass Lagrangian becomes:

$$-\mathcal{L}_{M_\nu} = \frac{1}{2} \sum_{k=1}^{3+m} m_k (\bar{\nu}_{\text{mass},k}^c \nu_{\text{mass},k} + \bar{\nu}_{\text{mass},k} \nu_{\text{mass},k}^c) \quad (2.43)$$

$$= \frac{1}{2} \sum_{k=1}^{3+m} m_k \bar{\nu}_{M_k} \nu_{M_k}, \quad (2.44)$$

where $\nu_{M_k} = \nu_{\text{mass},k} + \nu_{\text{mass},k}^c$ satisfies the Majorana condition $\nu_{M_k} = \nu_{M_k}^c$.

In this mass basis, the original weak-interaction neutrino fields are related to the Majorana mass eigenstates by:

$$\nu_{Li} = P_L \sum_{j=1}^{3+m} V_{ij}^\nu \nu_{M_j}, \quad i = 1, 2, 3. \quad (2.45)$$

In the phenomenologically relevant limit where the eigenvalues of M_N are much larger than the electroweak scale, $M_N \gg v$, the diagonalization of M_ν yields three light neutrino states ν_l and m heavy neutrino states N :

$$-\mathcal{L}_{M_\nu} = \frac{1}{2} \bar{\nu}_l M^l \nu_l + \frac{1}{2} \bar{N} M^h N, \quad (2.46)$$

with approximate mass matrices:

$$M^l \simeq -V_l^T M_D^T M_N^{-1} M_D V_l, \quad (2.47)$$

$$M^h \simeq V_h^T M_N V_h, \quad (2.48)$$

and mixing matrix:

$$V^\nu \simeq \begin{pmatrix} \left(1 - \frac{1}{2}M_D^\dagger M_N^{*-1} M_N^{-1} M_D\right) V_l & M_D^\dagger M_N^{*-1} V_h \\ -M_N^{-1} M_D V_l & \left(1 - \frac{1}{2}M_N^{-1} M_D M_D^\dagger M_N^{*-1}\right) V_h \end{pmatrix}. \quad (2.49)$$

Here, V_l and V_h are 3×3 and $m \times m$ unitary matrices that describe mixing among the light and heavy neutrino sectors, respectively. The matrix V_l may be identified with the Pontecorvo–Maki–Nakagawa–Sakata (PMNS) matrix, which is discussed in detail in a later section.

The structure of the mass eigenvalues illustrates the origin of the term *seesaw*: the heavy neutrino masses scale with M_N , while the light neutrino masses are suppressed by M_N^{-1} . This mechanism is known as the Type-I seesaw, characterized by the introduction of heavy sterile neutrinos. It naturally produces light, predominantly left-handed neutrinos and heavy, predominantly right-handed neutrinos.

The Type-I seesaw mechanism therefore provides a compelling extension of the Standard Model that explains the smallness of neutrino masses without invoking extremely small Yukawa couplings. Furthermore, the heavy sterile neutrinos introduced in this framework may have important implications for physics beyond the Standard Model, including potential connections to dark matter.

2.3.4 Lepton Number Violation and Leptogenesis

A key consequence of Majorana neutrinos is the violation of lepton number. In the Standard Model, lepton number is an accidental global symmetry. This means that it's not imposed by construction, but instead emerges because no renormalizable operators that violate lepton number are allowed by the gauge symmetries and field content. Many extensions of the Standard Model, however, naturally incorporate lepton number violation.

Lepton number violation also plays a central role in leptogenesis, a proposed

explanation for one of the most fundamental questions in particle physics: why the observable Universe contains more matter than antimatter. A comprehensive review of the phenomenology of matter–antimatter asymmetry is beyond the scope of this chapter. Instead, a brief summary of the key observational and theoretical ingredients relevant to leptogenesis is presented here.

The baryon asymmetry of the Universe is inferred from two independent classes of observations. The first arises from measurements of the primordial abundances of light elements, such as D , ^3He , ^4He , and ^7Li , produced during Big Bang nucleosynthesis (BBN). These abundances depend on the baryon-to-photon asymmetry parameter η , which is measured to be [19]:

$$\eta^{\text{BBN}} \equiv \left. \frac{n_B - n_{\bar{B}}}{n_\gamma} \right|_0 = (4.7\text{--}6.5) \times 10^{-10} \quad (2.50)$$

The second constraint comes from observations of anisotropies in the cosmic microwave background (CMB) [20]. A key CMB observable is the speed of sound c_s in the photon–baryon fluid. Measurements of temperature fluctuations in the CMB determine the baryon energy density ρ_B , commonly expressed in terms of the baryon density parameter:

$$\Omega_B = \frac{\rho_B}{\rho_{\text{crit}}} \quad (2.51)$$

The corresponding baryon asymmetry inferred from CMB observations is:

$$\eta^{\text{CMB}} = 2.74 \times 10^{-8} \Omega_B h^2 = 6.1_{-0.2}^{+0.3} \times 10^{-10} \quad (2.52)$$

where $h = H_0/(100 \text{ km s}^{-1} \text{ Mpc}^{-1}) = 0.682 \pm 0.0028$ is the dimensionless Hubble parameter [21]. The remarkable agreement between the BBN and CMB determinations of the baryon asymmetry represents a major success of hot Big Bang cosmology.

Any dynamical mechanism responsible for generating the observed baryon asymmetry must satisfy three necessary conditions, first identified by Sakharov and now

known as the Sakharov conditions:

1. Baryon number violation
2. C and CP violation
3. Departure from thermal equilibrium

Although the Standard Model contains all three ingredients in principle, it fails to produce a baryon asymmetry of sufficient magnitude.

Leptogenesis provides a compelling beyond-the-Standard-Model framework in which these conditions can be satisfied. In this scenario, the heavy sterile neutrinos introduced in the Type-I seesaw mechanism undergo CP-violating, out-of-equilibrium decays that generate a net lepton asymmetry. Electroweak sphaleron processes subsequently convert a fraction of this lepton asymmetry into a baryon asymmetry, linking the origin of neutrino mass to the matter–antimatter asymmetry of the Universe.

2.4 Double Beta Decay

As discussed in the previous sections, the observation of neutrino oscillations establishes that neutrinos are massive and motivates extensions of the Standard Model that may violate lepton number. Double beta decay arises naturally in this context, providing an experimental probe that is simultaneously sensitive to neutrino properties and to the nuclear many-body dynamics governing rare weak processes. In particular, $0\nu\beta\beta$ offers a direct test of lepton number violation and the Majorana nature of neutrinos. However, the interpretation of $0\nu\beta\beta$ searches is fundamentally limited by uncertainties in the associated nuclear matrix elements (NMEs).

The $2\nu\beta\beta$ decay process, which is allowed within the Standard Model and has been experimentally observed in multiple nuclei, plays a critical complementary role. Measurements of this process provide an essential experimental benchmark for nuclear

structure calculations. Of particular interest are two-neutrino double beta decay transitions to excited states of the daughter nucleus, which offer an underexplored but highly informative probe of nuclear dynamics. Measurements or limits on these transitions directly test the same nuclear operators that appear in $0\nu\beta\beta$ decay and are therefore especially relevant for reducing theoretical uncertainties in $0\nu\beta\beta$ decay searches. In the following sections, the theoretical framework of double beta decay is reviewed, with emphasis on two-neutrino double beta decay to excited states and their connection to nuclear matrix elements relevant for $0\nu\beta\beta$.

2.5 Two-Neutrino Double Beta Decay

Most unstable nuclei decay through first-order weak processes such as single β^- decay or electron capture, converting a neutron into a proton or vice versa while conserving lepton number. In some even–even nuclei, however, single beta decay is energetically forbidden or strongly suppressed, while a second-order weak process involving the simultaneous conversion of two neutrons into two protons becomes allowed. This $2\nu\beta\beta$ process was first proposed by Goeppert-Mayer in 1935 and is permitted within the Standard Model [22].

The canonical $2\nu\beta\beta$ process proceeds as

$$(A, Z) \rightarrow (A, Z + 2) + 2e^- + 2\bar{\nu}_e, \quad (2.53)$$

conserving total lepton number. The decay changes the nuclear charge by two units while leaving the mass number unchanged and occurs only if the resulting daughter nucleus is more tightly bound than the parent. The available energy, or Q value, is given by

$$Q_{\beta\beta} = m_N(^A_Z X) - m_{N-2}(^A_{Z+2} X') - 2m_e \quad (2.54)$$

which sets the scale for the phase space available to the emitted leptons. Here, m_e is the electron mass in the rest frame, $m_N (^A_Z X)$ is the mass of the mother nucleus in the rest frame, and $m_{N-2} (^{A+2}_{Z+2} X')$ represents the mass of the daughter nucleus in the rest frame.

Not all nuclei are capable of undergoing double beta decay. Whether a given isotope can decay via the $2\nu\beta\beta$ process is determined by nuclear binding energies and the relative stability of neighboring isobars. Insight into this behavior can be obtained from the semi-empirical description of nuclear masses.

The mass of an atomic nucleus with mass number A and atomic number Z may be written as:

$$M = Zm_p + (A - Z)m_n - E(A, Z) \quad (2.55)$$

where m_p and m_n are the proton and neutron rest masses, respectively, and $E(A, Z)$ is the nuclear binding energy. The binding energy is well approximated by the semi-empirical mass formula:

$$E = a_v A - a_s A^{2/3} - a_C \frac{Z(Z-1)}{A^{1/3}} - a_A \frac{(N-Z)^2}{A} + \delta(N, Z) \quad (2.56)$$

which captures the dominant contributions to nuclear stability. The volume and surface terms describe the short-range attractive strong force, the Coulomb term accounts for proton–proton repulsion, and the asymmetry term reflects the energy cost of unequal numbers of protons and neutrons imposed by the Pauli exclusion principle.

The final contribution, $\delta(N, Z)$, represents the pairing energy and depends on

whether the nucleus contains even or odd numbers of protons and neutrons:

$$\delta(N, Z) = \begin{cases} -a_p A^{-1/2} & \text{even-even nuclei,} \\ 0 & \text{even-odd or odd-even nuclei,} \\ +a_p A^{-1/2} & \text{odd-odd nuclei} \end{cases} \quad (2.57)$$

This term favors nuclei with paired nucleons, making even–even nuclei systematically more tightly bound than their odd–odd neighbors.

As a result, nuclei with odd mass number A typically possess a single stable isobar and undergo ordinary beta decay if energetically allowed. In contrast, nuclei with even mass number exhibit two possible pairing configurations, leading to the familiar parabolic dependence of nuclear mass on Z for fixed A as shown in Figure 2·1. In some even–even nuclei, single β^- decay is energetically forbidden or strongly suppressed due to angular momentum and parity constraints, while the nucleus two units away in Z is more tightly bound. In such cases, the nucleus may decay directly to this lower-energy configuration through the simultaneous emission of two electrons and two antineutrinos.

This structure explains why $2\nu\beta\beta$ decay is observed only in a limited set of even–even nuclei and highlights the close connection between double beta decay and nuclear pairing effects. These same nuclear structure considerations also influence transitions to excited states of the daughter nucleus and play an important role in shaping the nuclear matrix elements relevant for both $2\nu\beta\beta$ and $0\nu\beta\beta$ decay.

The rate of $2\nu\beta\beta$ decay can be calculated using Fermi’s golden rule, treating the process as a second-order weak interaction involving the emission of four leptons in the final state. The inverse half-life for $2\nu\beta\beta$ decay may be written in the standard

factorized form:

$$\Gamma^{2\nu} \equiv (T_{1/2}^{2\nu})^{-1} = G^{2\nu}(Q_{\beta\beta}, Z) \left| \mathcal{M}_{GT}^{2\nu} + \frac{g_V^2}{g_A^2} \mathcal{M}_F^{2\nu} \right|^2 \quad (2.58)$$

where $G^{2\nu}(Q_{\beta\beta}, Z)$ is the phase-space factor, g_V and g_A are the vector and axial-vector weak coupling constants, and $\mathcal{M}_F^{2\nu}$ and $\mathcal{M}_{GT}^{2\nu}$ are the Fermi and Gamow–Teller nuclear matrix elements, respectively.

The phase-space factor $G^{2\nu}$ accounts for the integration over the energies and angles of the two emitted electrons and two antineutrinos and depends strongly on the available decay energy $Q_{\beta\beta}$ and the nuclear charge Z . These phase-space factors can be calculated with relatively high precision using relativistic electron wave functions and Coulomb corrections and are among the best-controlled theoretical inputs to the $2\nu\beta\beta$ decay rate [24, 25].

In contrast, the nuclear matrix elements encode the details of nuclear structure and many-body correlations. The Fermi matrix element $\mathcal{M}_F^{2\nu}$ corresponds to tran-

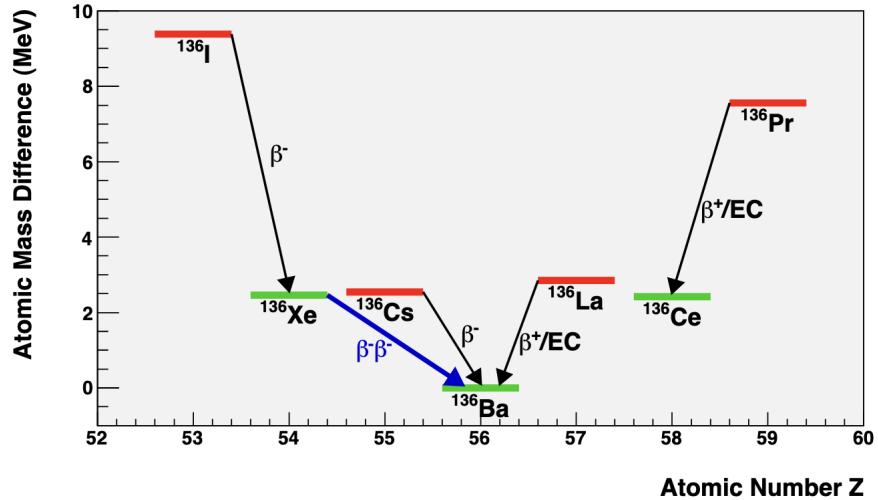


Figure 2·1: Atomic masses of $A = 136$ isotopes. Masses are given as differences with respect to the most bound isotope, ^{136}Ba . The red (green) levels indicate odd-odd (even-even) nuclei. Figure taken from [23].

sitions with no change in nuclear spin and arises from the vector component of the weak interaction, while the Gamow–Teller matrix element $\mathcal{M}_{GT}^{2\nu}$ corresponds to spin-changing transitions mediated by the axial-vector current. For two-neutrino double beta decay, Fermi transitions are strongly suppressed due to isospin conservation, as the dominant contribution proceeds through intermediate 1^+ states, corresponding to $0^+ \rightarrow 1^+ \rightarrow 0^+$ nuclear transitions. As a result, the decay rate is overwhelmingly dominated by the Gamow–Teller contribution.

Because $2\nu\beta\beta$ decay is a second-order weak process, its half-life is extremely long, with experimentally measured values typically in the range of 10^{19} to 10^{22} years [26]. While calculations of $G^{2\nu}$ are robust, theoretical predictions of $\mathcal{M}_{GT}^{2\nu}$ depend sensitively on the nuclear model employed and often fail to reproduce experimental half-lives without additional modifications. To account for this discrepancy, it is common to introduce an effective axial-vector coupling constant, g_A^{eff} , which is quenched relative to the free-nucleon value g_A . This is typically implemented through a rescaling of the Gamow–Teller matrix element,

$$\mathcal{M}_{GT}^{2\nu,\text{eff}} = \left(\frac{g_A^{\text{eff}}}{g_A} \right)^2 \mathcal{M}_{GT}^{2\nu}. \quad (2.59)$$

The magnitude and physical origin of this quenching remain subjects of active investigation and are thought to arise from a combination of missing many-body correlations, non-nucleonic degrees of freedom, and limitations of model spaces used in nuclear calculations [27]. Importantly, uncertainties associated with g_A^{eff} directly impact predictions for both $2\nu\beta\beta$ and $0\nu\beta\beta$ decay rates, further motivating experimental studies of $2\nu\beta\beta$ decay, including transitions to excited nuclear states.

2.6 Neutrinoless Double Beta Decay

Building on Goeppert-Mayer’s work on $2\nu\beta\beta$ decay, Wendell Furry proposed the neutrinoless mode, now known as $0\nu\beta\beta$ decay [28]:



Unlike the two-neutrino mode, this process violates total lepton number by two units and is therefore forbidden within the Standard Model. Observation of $0\nu\beta\beta$ would constitute direct evidence of lepton number violation and establish that neutrinos are Majorana particles.

From an experimental standpoint, $0\nu\beta\beta$ and $2\nu\beta\beta$ share many similarities. Both are second-order weak processes and occur in the same set of even–even nuclei for which single beta decay is energetically forbidden. In both cases, nuclear recoil is negligible, and the decay energy is carried almost entirely by the emitted electrons. The key experimental distinction is that while $2\nu\beta\beta$ produces a continuous electron energy spectrum extending up to the endpoint energy $Q_{\beta\beta}$, $0\nu\beta\beta$ would manifest as a monoenergetic peak at the endpoint, smeared only by detector energy resolution.

Although phase-space considerations alone would favor the neutrinoless mode, the requirement of lepton number violation renders the decay rate extremely small, leading to half-lives exceeding 10^{26} years for experimentally accessible isotopes. As a result, $0\nu\beta\beta$ is among the rarest processes sought in modern experimental physics.

In general, several mechanisms beyond the Standard Model could mediate $0\nu\beta\beta$ decay, including heavy particle exchange or other lepton-number-violating interactions. However, a model-independent result known as the Schechter–Valle (or “Black Box”) theorem demonstrates that the observation of $0\nu\beta\beta$, regardless of the underlying mechanism, necessarily implies that neutrinos possess a Majorana mass [29]. The theorem does not specify which mechanism dominates the decay rate, nor does

it require a direct connection to neutrino oscillation phenomenology. Specifically, it proposes the following:

- Should $0\nu\beta\beta$ be observed, its Feynman diagram must feature two electrons, two up-quark fields, and two down-quark fields. The process connecting these fields is arbitrary and is referred to as the "black box process". The theorem argues that this "black box process" effectively establishes the dimension-9 operator.
- The up and down quarks are contracted by the W boson.
- On the other end of the W boson propagators, electron fields are converted into neutrino fields.
- The entire diagram can be rotated to turn into a process that converts anti-neutrinos to neutrinos as shown in Figure 2·2.
- Finally, the possible cancelation of this process by other diagrams is dismissed by naturalness arguments.

The key conclusion of the black-box theorem is that should $0\nu\beta\beta$ be observed, even if the observed mechanism is not light Majorana neutrino exchange, the neutrino is a Majorana particle. It should be noted that since the theorem's original proposal,

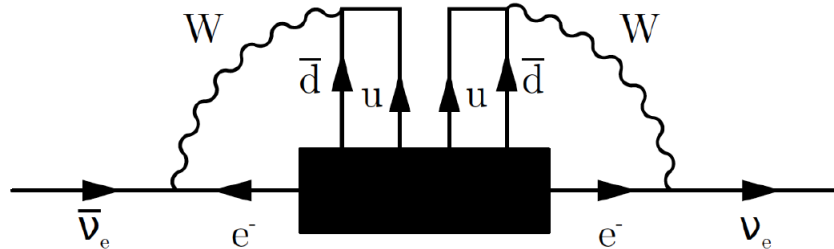


Figure 2·2: Depiction of the $0\nu\beta\beta$ black box theorem, the black box represents an arbitrary $0\nu\beta\beta$ process, which can be used to convert antineutrinos into neutrinos. Figure taken from Reference [30].

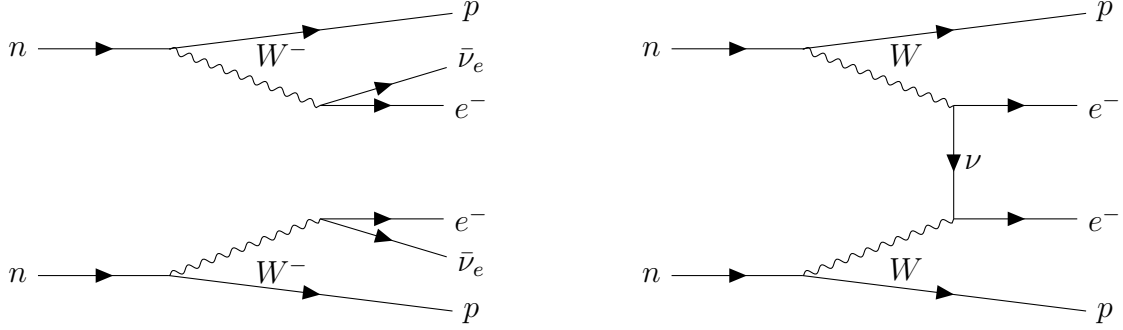


Figure 2.3: Feynman diagrams for $2\nu\beta\beta$ decay (Left) and $0\nu\beta\beta$ decay (Right).

counterexamples have been found allowing $0\nu\beta\beta$ without Majorana neutrinos [31], but the theorem still indicates potential links between $0\nu\beta\beta$, Majorana mass, and lepton number violation more broadly.

The most widely studied and experimentally motivated scenario is the light Majorana neutrino exchange mechanism. In this case, the decay proceeds through the exchange of a virtual neutrino between two Standard Model weak vertices as illustrated in comparison to $2\nu\beta\beta$ decay in Figure 2.3. The amplitude is nonzero only if neutrinos are massive and Majorana, as the process requires a helicity flip proportional to the neutrino mass. This mechanism provides a direct link between $0\nu\beta\beta$ decay and the absolute neutrino mass scale.

Under the assumption that light Majorana neutrino exchange dominates, the inverse half-life for $0\nu\beta\beta$ decay can be written in factorized form as:

$$(T_{1/2}^{0\nu})^{-1} = G^{0\nu}(Q_{\beta\beta}, Z) |\mathcal{M}^{0\nu}|^2 \left(\frac{m_{\beta\beta}}{m_e} \right)^2 \quad (2.61)$$

where $G^{0\nu}$ is the phase-space factor, $\mathcal{M}^{0\nu}$ is the nuclear matrix element, m_e is the electron mass, and $m_{\beta\beta}$ is the effective Majorana neutrino mass:

$$m_{\beta\beta} = |m_1 U_{e1}^2 + m_2 U_{e2}^2 e^{2i\xi_1} + m_3 U_{e3}^2 e^{2i\xi_2}| \quad (2.62)$$

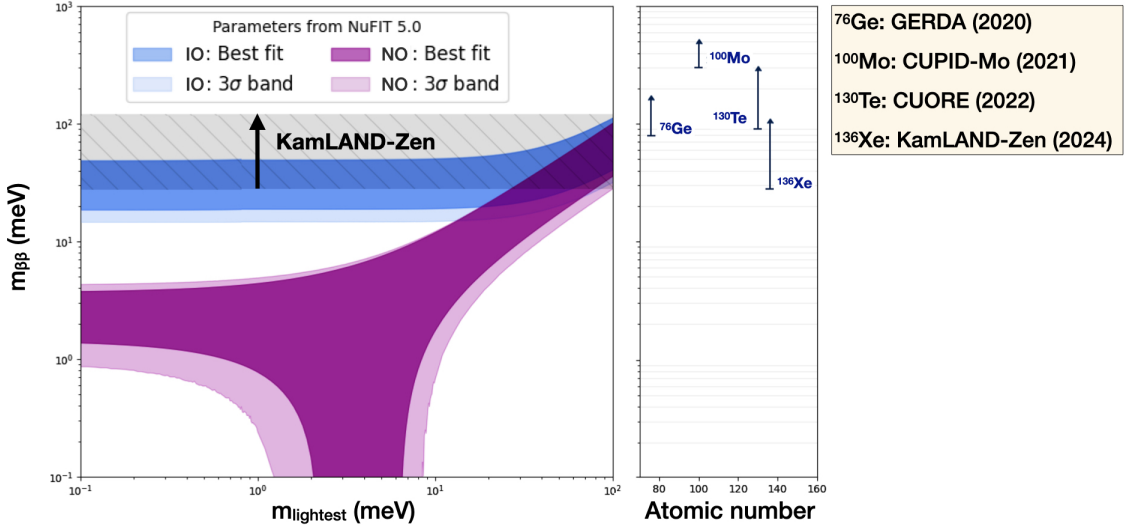


Figure 2.4: Possible Majorana masses for normal (magenta) and inverted (blue) mass orderings, calculated with mixing angles and mass differences from the PMNS matrix. The error bands come from uncertainties in the mixing parameters [11]. The KamLAND-Zen experimental limit on $m_{\beta\beta}$ is shown in gray. Recent limits [32, 33, 34] for other key isotopes are shown in the panel on the right. Figure taken from Reference [35].

Here, m_i are the light neutrino mass eigenvalues, U_{ei} are elements of the PMNS mixing matrix, and ξ_i are the Majorana CP-violating phases. Unlike neutrino oscillation experiments, which are insensitive to the absolute mass scale and Majorana phases, $0\nu\beta\beta$ decay probes both. The unknown values of the Majorana phases lead to allowed bands for $m_{\beta\beta}$ as a function of the lightest neutrino mass, with distinct regions corresponding to normal and inverted mass orderings. As a result, experimental limits on the $0\nu\beta\beta$ half-life translate into ranges of allowed $m_{\beta\beta}$ values rather than a single constraint which is illustrated in Figure 2.4.

While the phase-space factor $G^{0\nu}$ can be calculated with high precision, the NME $\mathcal{M}^{0\nu}$ remains the largest source of theoretical uncertainty in interpreting $0\nu\beta\beta$ searches. The calculation of $\mathcal{M}^{0\nu}$ requires detailed knowledge of nuclear wave func-

tions and many-body correlations and depends on the treatment of short-range physics, nuclear deformation, and the effective axial-vector coupling. For the standard light Majorana neutrino exchange mechanism, the NME can be written schematically as a sum of long- and short-range contributions:

$$\mathcal{M}_{\text{light}}^{0\nu} = g_A^4 (\mathcal{M}_{\text{long}}^{0\nu} + \mathcal{M}_{\text{short}}^{0\nu}) \quad (2.63)$$

The axial-vector coupling constant g_A governs the long-range weak interaction of nucleons and is factored out explicitly, serving as an important parameter in nuclear many-body calculations. The short-range contribution depends additionally on a two-nucleon coupling, g^{NN} , which is not written explicitly here. As in the case of $2\nu\beta\beta$ decay, the phase-space factors relevant for $0\nu\beta\beta$ are known with high precision for all experimentally relevant isotopes [24, 25]. In contrast, the NMEs themselves, along with some associated hadronic couplings, remain a dominant source of theoretical uncertainty despite significant recent progress.

The nuclear matrix elements (NMEs) encode the influence of nuclear structure on the rate of neutrinoless double beta decay and are obtained by combining nuclear wave functions for the initial and final states with the appropriate transition operators. In practice, NMEs are evaluated using nuclear many-body methods that attempt to capture correlations among nucleons across a wide range of length and energy scales. When limits on the $0\nu\beta\beta$ half-life are translated into constraints on the effective Majorana mass $m_{\beta\beta}$, the resulting uncertainty is presently dominated by the spread in available NME calculations rather than by experimental systematics. A detailed theoretical treatment of the construction of the transition operators, the treatment of short-range correlations, and the associated theoretical uncertainties lies beyond the scope of this thesis. Comprehensive reviews of modern NME calculations can be found in Reference [36].

In general, NME calculations proceed by first specifying an effective nuclear Hamiltonian that includes nucleon–nucleon interactions relevant to the decay process. A second step then introduces a framework for describing collective nuclear structure and many-body correlations beyond the mean-field level. The most widely used approaches are summarized below.

- The **Nuclear Shell Model (NSM)** has long served as a foundational tool for describing nuclear structure. In this framework, nucleons are treated as moving independently within a mean-field potential, augmented by a strong spin–orbit interaction. This potential, often modeled using harmonic oscillator or Woods–Saxon forms, represents the averaged interaction of a nucleon with the rest of the nucleus. The resulting single-particle states organize into energy shells, with particularly stable configurations occurring at so-called magic numbers. For practical calculations, the nucleus is typically separated into an inert core of filled shells and a smaller set of active valence nucleons. While the shell model provides a highly detailed description of nuclear correlations within the chosen model space, computational limitations restrict its applicability to relatively small valence spaces.
- The **Quasiparticle Random Phase Approximation (QRPA)** extends mean-field approaches by incorporating collective excitations and pairing correlations across a large set of nuclear orbitals. It is particularly well suited for medium and heavy nuclei, where shell-model calculations become computationally prohibitive. QRPA calculations rely on effective proton–neutron interactions, commonly parameterized by the coupling strength g_{pp} , which governs proton–neutron pairing. This parameter is often constrained by requiring agreement with experimentally measured $2\nu\beta\beta$ decay rates and subsequently applied to predictions of $0\nu\beta\beta$ decay. As a result, QRPA provides an explicit link be-

tween two-neutrino and neutrinoless decay calculations.

- **Energy Density Functional (EDF)** methods describe nuclei using energy functionals that depend on local densities and currents, extending the concept of mean-field theory in a self-consistent manner. These methods allow for the inclusion of important nuclear effects such as deformation, pairing, configuration mixing, and collective motion. EDF calculations have proven effective in describing medium and heavy nuclei, which are of primary interest for double beta decay searches. However, EDF-based NMEs are often among the largest reported values, in part because certain proton–neutron correlations are not treated explicitly.
- The **Interacting Boson Model (IBM)** provides a simplified, phenomenological description of nuclear structure by mapping pairs of valence nucleons onto bosonic degrees of freedom. In the context of double beta decay, the IBM has been extended to distinguish between proton and neutron bosons (IBM-2), enabling calculations of NMEs for even–even nuclei. While the model sacrifices microscopic detail, it offers a computationally efficient framework for exploring systematic trends across isotopic chains.
- ***Ab initio*** methods aim to describe nuclei starting from fundamental interactions derived from quantum chromodynamics via chiral effective field theory. These methods treat all nucleons explicitly and employ nuclear Hamiltonians with minimal phenomenological input. A key advantage of ab initio calculations is their systematic improvability and the ability to assess convergence. While these methods successfully reproduce properties of light and some medium-mass nuclei, extending them to the heavy nuclei relevant for $0\nu\beta\beta$ decay remains an active area of research [37].

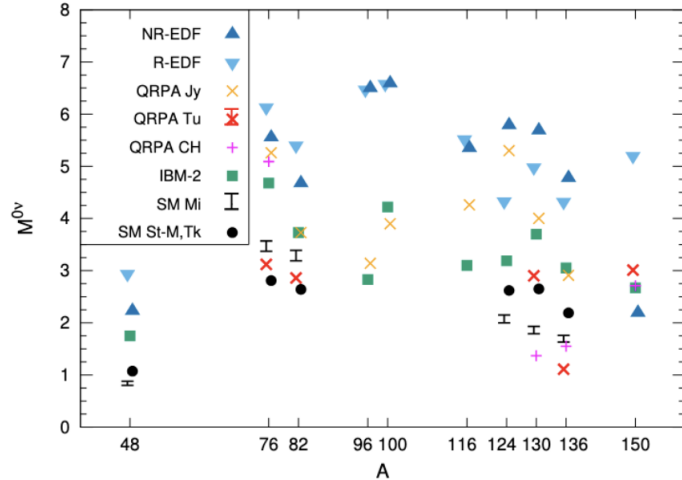


Figure 2·5: Results from various NME calculation of $M_{0\nu}$ on particular $0\nu\beta\beta$ decaying isotopes versus atomic mass. Figure taken from Reference [36].

To illustrate the level of agreement among different approaches, Figure 2·5 summarizes recent NME calculations for several candidate $0\nu\beta\beta$ isotopes. For a given nucleus, the predicted NMEs typically vary by factors of two to three across models. This spread constitutes one of the primary theoretical limitations in extracting neutrino mass information from $0\nu\beta\beta$ decay searches and provides strong motivation for experimental probes, such as two-neutrino double beta decay to excited states, that can help benchmark and constrain nuclear structure calculations.

Current nuclear structure methods yield values of $\mathcal{M}^{0\nu}$ that differ by factors of two to three for the same isotope. These discrepancies directly propagate into uncertainties on the extracted limits or measurements of $m_{\beta\beta}$. As a result, the physics reach of $0\nu\beta\beta$ experiments is no longer limited solely by exposure or background reduction, but increasingly by the reliability of nuclear matrix element calculations. Reducing these uncertainties has therefore become a central goal in the field.

2.7 Double Beta Decay to Excited States

An additional class of processes can provide valuable experimental input into NME calculations and aid in the interpretation of $0\nu\beta\beta$ decay searches: two-neutrino double beta decay to excited states of the daughter nucleus, denoted $2\nu\beta\beta^*$. In these Standard Model–allowed transitions, the parent nucleus undergoes double beta decay but populates an excited state of the daughter rather than its ground state. The subsequent de-excitation of the daughter nucleus produces a characteristic gamma-ray cascade.

Decays to excited states are suppressed by several orders of magnitude relative to ground-state transitions due to the reduced available phase space arising from the smaller effective Q value [38]. As a consequence, theoretical predictions for the corresponding half-lives span multiple orders of magnitude, reflecting the same nuclear-structure uncertainties that dominate predictions for $0\nu\beta\beta$ decay. Figure 2·6 illustrates representative predictions for $T_{1/2}^{2\nu^*}$ obtained using different nuclear models. An experimental observation of $2\nu\beta\beta^*$ in xenon would therefore provide a powerful constraint on nuclear matrix element calculations and help reduce theoretical uncertainties relevant to $0\nu\beta\beta$ searches.

The discussion below follows closely the formalism presented in Ref. [40], which explores the relationship between $2\nu\beta\beta$ and $0\nu\beta\beta$ NMEs within the NSM and the proton–neutron quasiparticle random-phase approximation (pnQRPA). The experimental signature of $2\nu\beta\beta^*$ consists of a standard $2\nu\beta\beta$ decay, followed (after a delay of order picoseconds) by the emission of one or more gamma rays as the daughter nucleus relaxes to its ground state. Experimentally, identifying this process requires either particle identification techniques capable of tagging the de-excitation gamma rays or the observation of distortions in the electron energy spectrum relative to the dominant ground-state $2\nu\beta\beta$ background. While challenging, these signatures provide

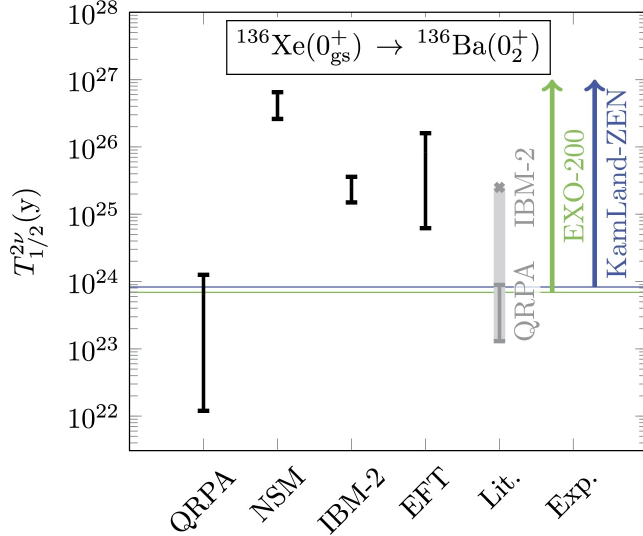


Figure 2.6: Predictions of $T_{1/2}^{2\nu*}$ using various NME calculation methods. Figure taken from [39].

additional handles for background discrimination compared to ground-state decays.

As mentioned in Section 2.5 the half-life for $2\nu\beta\beta$ decay can be reasonably approximated with a single nuclear matrix element [40]:

$$\mathcal{M}^{2\nu} = - \sum_k \frac{\left(0_f^+ \left\| \sum_a \tau_a^- \sigma_a \right\| 1_k^+ \right) \left(1_k^+ \left\| \sum_b \tau_b^- \sigma_b \right\| 0_i^+ \right)}{[E_k - (E_i + E_f)/2]/m_e} \quad (2.64)$$

where the indices a and b run over all nucleons, τ^- is the isospin-lowering operator converting neutrons into protons, and σ is the spin operator. The sum extends over all intermediate 1^+ states of the odd–odd nucleus, with the energy denominator involving the excitation energy of each intermediate state relative to the average of the initial and final nuclear energies.

In contrast, the $0\nu\beta\beta$ nuclear matrix element (assuming the standard light Majorana neutrino exchange mechanism) is conventionally decomposed into three spin–isospin components:

$$\mathcal{M}_L^{0\nu} = \mathcal{M}_{GT}^{0\nu} - \mathcal{M}_F^{0\nu} + \mathcal{M}_T^{0\nu}, \quad (2.65)$$

corresponding to Gamow–Teller (GT), Fermi (F), and tensor (T) contributions.

These components are defined in terms of two-body operators:

$$\mathcal{M}_K^{0\nu} = \sum_{k,ab} (0_f^+ \|\mathcal{O}_{ab}^K \tau_a^- \tau_b^- H_K(r_{ab}) f_{\text{SRC}}^2(r_{ab}) \| 0_i^+) \quad (2.66)$$

where $\mathcal{O}_{ab}^F = \mathbb{1}$, $\mathcal{O}_{ab}^{GT} = \sigma_a \cdot \sigma_b$, and

$$\mathcal{O}_{ab}^T = 3(\sigma_a \cdot \hat{r}_{ab})(\sigma_b \cdot \hat{r}_{ab}) - \sigma_a \cdot \sigma_b$$

The quantity r_{ab} denotes the distance between nucleons a and b , and $f_{\text{SRC}}(r)$ accounts for short-range correlations.

The neutrino potential $H_K(r_{ab})$ encodes the momentum dependence of the virtual neutrino exchange and is given by:

$$H_K(r_{ab}) = \frac{2R}{\pi g_A^2} \int_0^\infty \frac{h_K j_\lambda(pr_{ab}) p^2 dp}{\epsilon_K}, \quad (2.67)$$

where $\epsilon_K = p [p + E_k - (E_i + E_f)/2]$, $g_A = 1.27$, and $R = 1.2A^{1/3}$ fm. The structure of this potential introduces a characteristic radial dependence into the NME, allowing the matrix elements to be expressed in terms of radial distributions:

$$M_L^{0\nu}(1b) = \int_0^\infty C^{0\nu}(r) dr, \quad M^{2\nu} = \int_0^\infty C^{2\nu}(r) dr. \quad (2.68)$$

For $0\nu\beta\beta$ decay, the radial distribution may be decomposed as:

$$C^{0\nu}(r) = C_{GT}^{0\nu}(r) - C_F^{0\nu}(r) + C_T^{0\nu}(r), \quad (2.69)$$

with:

$$C_K^{0\nu}(r) = \sum_{k,ab} (0_f^+ \|\mathcal{O}_{ab}^K \tau_a^- \tau_b^- H_K(r_{ab}) f_{\text{SRC}}^2(r_{ab}) \delta(r - r_{ab}) \| 0_i^+). \quad (2.70)$$

Reference [41] demonstrated that the radial distributions $C^{2\nu}(r)$ and $C^{0\nu}(r)$ exhibit striking qualitative similarities across a wide range of nuclei and model assumptions.

Figure 2·7 shows representative radial distributions for ^{76}Ge calculated within the pnQRPA framework. The similarity in the spatial structure of the two matrix elements suggests that both processes probe related nuclear correlations, despite their different momentum transfers.

While neither $2\nu\beta\beta$ nor $2\nu\beta\beta^*$ decay rates are accurately predicted *a priori* by nuclear models, strong correlations between $2\nu\beta\beta$ and $0\nu\beta\beta$ NMEs have been observed. In practice, calculated $2\nu\beta\beta$ NMEs are often renormalized using an effective axial coupling to reproduce measured half-lives. Despite this adjustment, the relative trends among isotopes remain robust.

Figure 2·8 illustrates the correlation between $2\nu\beta\beta$ and $0\nu\beta\beta$ NMEs obtained using both NSM and pnQRPA calculations. The presence of a clear correlation across different nuclear models supports the idea that improved experimental constraints on $2\nu\beta\beta$, and especially on the more selective $2\nu\beta\beta^*$ transitions, can provide meaningful benchmarks for nuclear structure calculations relevant to $0\nu\beta\beta$ decay.

These theoretical insights provide strong motivation for experimental searches

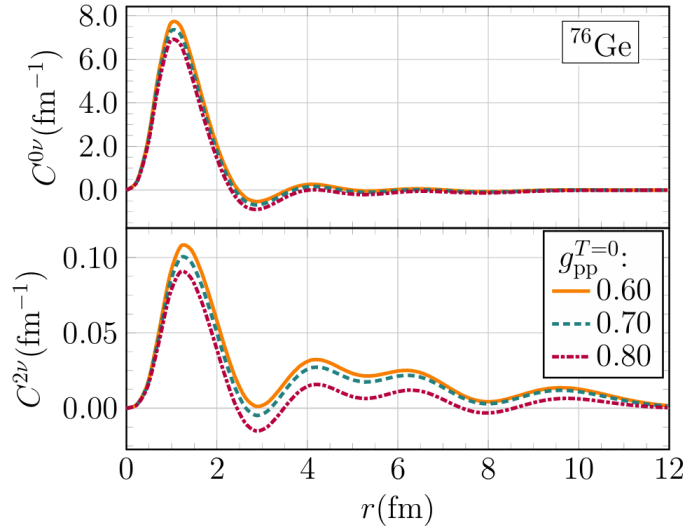


Figure 2·7: Radial distributions of $0\nu\beta\beta$ (top) and $2\nu\beta\beta$ (bottom) NMEs of ^{76}Ge obtained via pnQRPA. Figure taken from Reference [40].

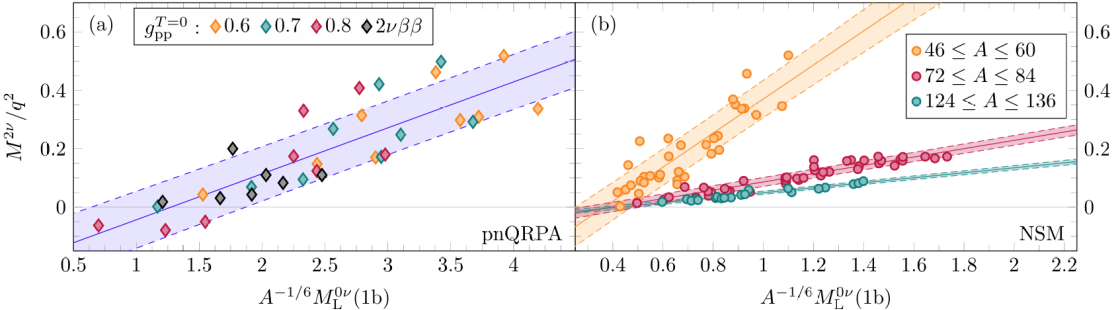


Figure 2.8: Correlation of $2\nu\beta\beta$ and $0\nu\beta\beta$ NME as calculated by NSM (Nuclear Shell Model) and pnQRPA (proton-neutron quasiparticle random-phase approximation) methods. Figure taken from Reference [42].

for $2\nu\beta\beta$ to excited states. Such measurements offer a unique opportunity to test nuclear many-body methods, constrain NME calculations, and ultimately improve the reliability of neutrino mass limits extracted from $0\nu\beta\beta$ decay experiments.

2.8 Double Beta Decay Experiments

If neutrinoless double beta decay ($0\nu\beta\beta$) exists, it is an extraordinarily rare process, with an expected half-life exceeding 10^{26} years for the most favorable isotopes. A confirmed observation would represent the slowest natural radioactive decay ever measured and would provide direct evidence for lepton number violation and the Majorana nature of neutrinos. The extreme rarity of this process imposes stringent requirements on experimental design. Successful $0\nu\beta\beta$ searches must simultaneously maximize signal efficiency while suppressing backgrounds to unprecedented levels. Several key criteria therefore define the performance of modern double beta decay experiments:

- **Excellent Energy Resolution:** The experimental signature of $0\nu\beta\beta$ is a monoenergetic peak at the decay Q value, coincident with the endpoint of the continuous $2\nu\beta\beta$ spectrum. Precise energy resolution is essential to minimize contamination from the $2\nu\beta\beta$ tail within the region of interest (ROI). State-of-

the-art experiments now achieve fractional energy resolutions of order $\sigma_E/E \simeq 0.1\%$, effectively eliminating $2\nu\beta\beta$ as a limiting background.

- **Large Isotope Mass:** Sensitivity to extremely long half-lives requires large exposures, motivating the deployment of tonne-scale quantities of double beta decaying isotopes. Achieving such isotope masses typically demands both isotopic enrichment and scalable detector technologies. In practice, enrichment cost and isotope availability often set the ultimate experimental scale.
- **Ultra-Low Background Environment:** Backgrounds from natural radioactivity and cosmic-ray interactions must be suppressed to levels below one count per tonne-year in the ROI. This necessitates operation in deep underground laboratories, stringent material screening, and detector designs that enable powerful background discrimination.

Among current-generation experiments, KamLAND-Zen has demonstrated world-leading sensitivity to $0\nu\beta\beta$ decay in ^{136}Xe . The most recent KamLAND-Zen result places a 90% confidence level limit on the effective Majorana neutrino mass of $m_{\beta\beta} < (28\text{--}122)$ meV, where the range reflects uncertainties associated with NME calculations. Figure 2.9 shows the corresponding constraints in the $m_{\beta\beta}$ – m_{lightest} plane for multiple NME models. The figure highlights the critical role of nuclear theory: for larger NMEs, the KamLAND-Zen limit begins to probe the non-degenerate region of the inverted neutrino mass ordering, whereas for smaller NMEs the constraint remains within the quasi-degenerate regime. KamLAND-Zen is currently the only $0\nu\beta\beta$ experiment whose sensitivity reaches the inverted-ordering parameter space for any NME calculation.

Two-neutrino double beta decay to excited states ($2\nu\beta\beta^*$) has been experimentally observed in only a small subset of known double beta decay isotopes. To date, positive detections have been reported for just two transitions:

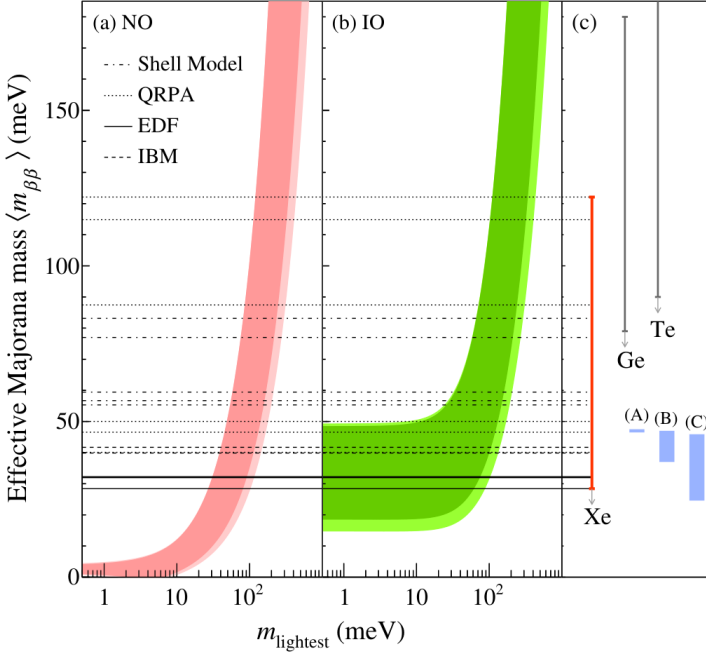


Figure 2.9: Effective Majorana neutrino mass as a function of the lightest neutrino mass state $m_{lightest}$. The shaded regions are based on best-fit values of neutrino oscillation parameters for (a) the normal ordering (NO) and (b) the inverted ordering (IO), the lighter shaded regions indicate the 3σ ranges based on oscillation parameter uncertainties. The horizontal lines indicate 90% C.L. limits on $m_{\beta\beta}$ considering multiple NME calculations. Figure taken from Reference [43].

- $^{100}\text{Mo} \rightarrow {}^{100}\text{Ru}(0_1^+)$, with $T_{1/2} = 5.9_{-0.6}^{+0.9} \times 10^{20}$ years,

- $^{150}\text{Nd} \rightarrow {}^{150}\text{Sm}(0_1^+)$, with $T_{1/2} = 1.33_{-0.26}^{+0.45} \times 10^{20}$ years.

The scarcity of observed $2\nu\beta\beta^*$ transitions reflects the substantial experimental challenges associated with these decays. Relative to ground-state $2\nu\beta\beta$, decays to excited states suffer from significantly reduced phase space and therefore much longer half-lives. However, their distinctive experimental signature, characterized by the coincident emission of de-excitation gamma rays, offers additional handles for background suppression and provides a powerful probe of nuclear structure.

To date, $2\nu\beta\beta^*$ decay has not been observed in ${}^{136}\text{Xe}$, the isotope used by KamLAND-Zen and the primary focus of this thesis. The current most stringent limit on this

process:

$$T_{1/2}^{2\nu}(0^+ \rightarrow 0_1^+) > 1.4 \times 10^{24} \text{ years} \quad (90\% \text{ C.L.})$$

was established by the EXO-200 experiment [44]. Figure 2.10 shows the EXO-200 spectral fits used to extract this limit. No statistically significant excess consistent with an excited-state signal was observed.

The analysis presented in this dissertation reports the latest search for $2\nu\beta\beta^*$ using KamLAND-Zen 800 data. Leveraging KamLAND-Zen's large ^{136}Xe mass, low background environment, and excellent energy resolution, this work achieves sensitivity beyond the existing EXO-200 limit. An improved constraint on $2\nu\beta\beta^*$ decay in ^{136}Xe would provide an important experimental benchmark for NME calculations and directly inform the interpretation of current and future $0\nu\beta\beta$ searches.

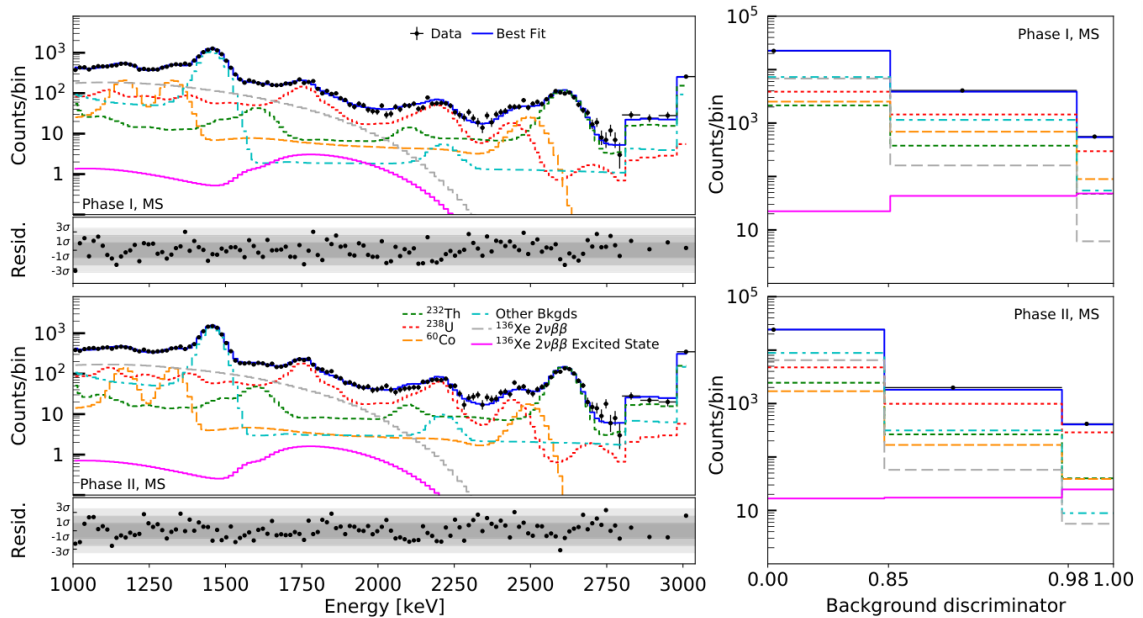


Figure 2.10: EXO-200's fit over energy spectrum (Left) and particle ID discriminator spectrum (Right) in two data-taking phases of the excited state signal and background. Figure taken from [44].

Chapter 3

The KamLAND-Zen Experiment

KamLAND, the **Kamioka Liquid-scintillator Anti-Neutrino Detector**, is a large liquid scintillator calorimeter located approximately 1 km underground beneath Mt. Ikenoyama in the Kamioka mine, Gifu Prefecture, Japan. In this chapter, the KamLAND detector and the surrounding experimental infrastructure are described, with emphasis on the modifications introduced for the KamLAND-Zen experiment. The roles of the detector subsystems are discussed in the context of the scientific goals of KamLAND-Zen and the analyses presented in this thesis.

3.1 KamLAND

The KamLAND detector can be viewed as a set of concentric spherical layers, each designed to shield and observe the innermost target volume. At the center of the detector resides the xenon-loaded liquid scintillator used by KamLAND-Zen for double-beta decay searches. The KamLAND detector is housed within a dedicated experimental area excavated in the Kamioka mine. Multiple caverns and passageways were constructed to accommodate the detector, purification systems, calibration facilities, and control electronics.

The KamLAND site is shown in Figure 3.1. The control room contains the networking, data acquisition, and monitoring equipment used by on-site shifters to oversee detector operation in real time. The first liquid scintillator (LS) purification area houses liquid–liquid extraction systems and nitrogen purging equipment, while the

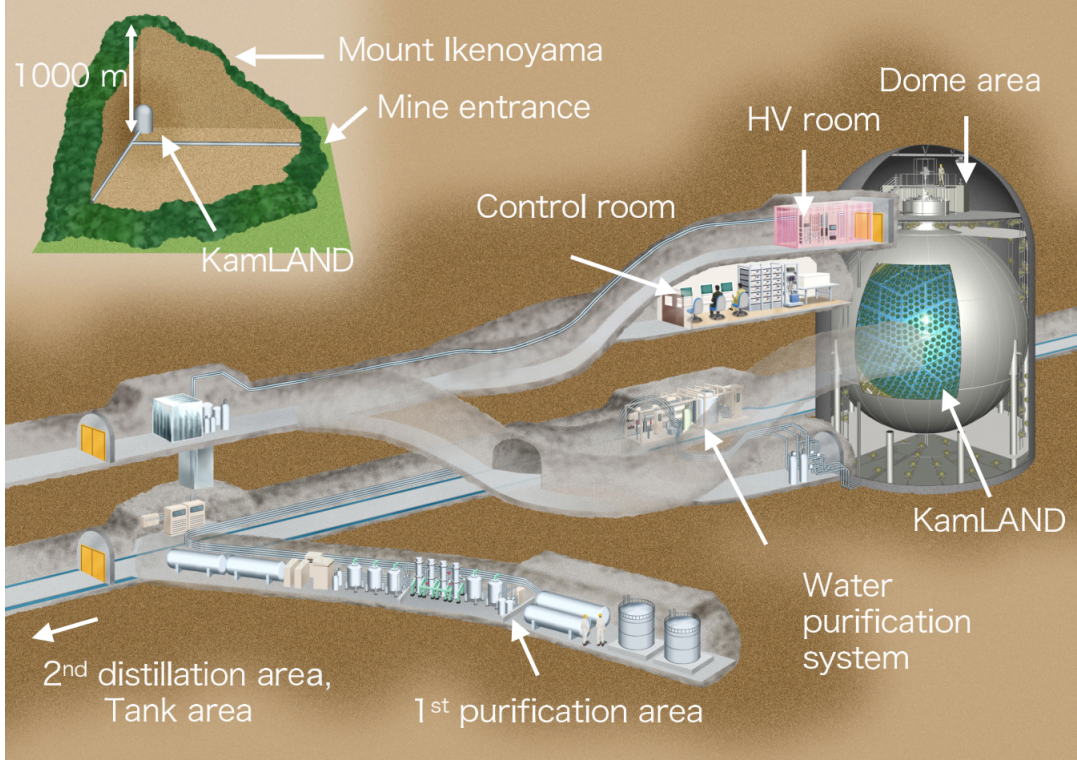


Figure 3·1: Illustration of the KamLAND site. Figure from Reference [45].

second purification area contains a large-scale distillation system. A dedicated xenon purification and handling area was constructed for KamLAND-Zen.

Above the detector, the dome area is maintained as a class-1000 clean environment and includes calibration source preparation facilities and the electronics hut (E-hut). At the center of the dome area, a secondary clean tent (class 100–1000) encloses the KamLAND chimney. All inner balloon installation and replacement operations were performed within this clean environment, most notably in August 2016 and May 2018.

The outer detector (OD) consists of a cylindrical water tank 20 m in height and 20 m in diameter, filled with ultra-pure water. The OD was refurbished in 2016, during which 140 new 20-inch Hamamatsu R3600 photomultiplier tubes (PMTs) were installed. The inner surface of the water tank and the exterior of the inner detector stainless-steel sphere are lined with highly reflective Tyvek sheets (Tyvek 1073B

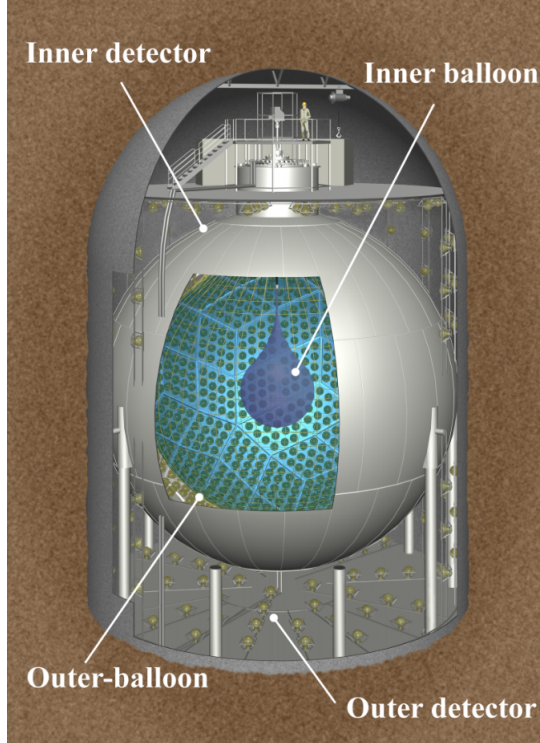


Figure 3·2: KamLAND-Zen detector. Figure from Reference [45].

and 1082D) to enhance light collection from cosmic-ray muons. The OD serves three primary functions: tagging cosmic-ray muons, shielding the inner detector from radioactivity and fast neutrons originating in the surrounding rock, and stabilizing the thermal environment of the inner detector.

The inner detector (ID), shown in Figure 3·2, is the primary scintillation detector of KamLAND. It consists of an 18 m-diameter stainless-steel spherical tank instrumented with 1,879 inward-facing PMTs: 1,325 17-inch PMTs and 554 20-inch PMTs. The PMTs are submerged in non-scintillating buffer oil (BO), which optically isolates the central scintillator volume from PMT-related radioactivity. An acrylic barrier divides the buffer oil into inner and outer regions, suppressing convective transport of radon emanating from PMT glass toward the detector center.

Photomultiplier tubes (PMTs) act as the photosensors of KamLAND, detecting

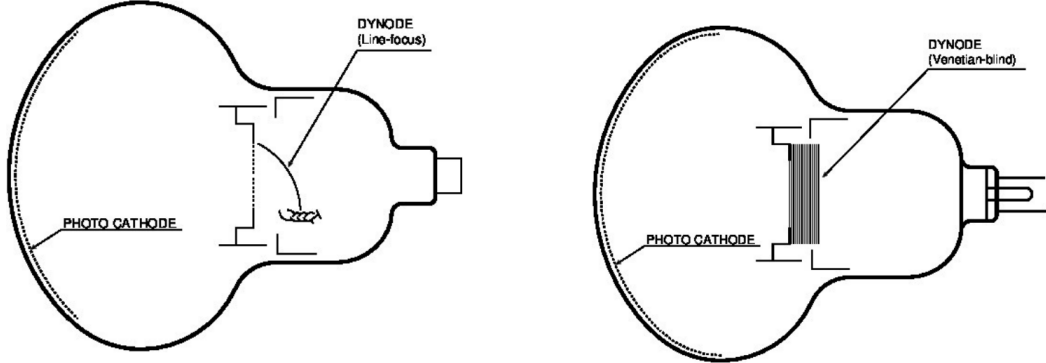


Figure 3·3: Schematics of the 17-inch and 20-inch PMTs. Figure from Reference [45].

scintillation photons produced by charged particles traversing the liquid scintillator. Incident photons striking the photocathode liberate photoelectrons, which are subsequently multiplied through a series of dynodes, producing an output charge of approximately 10^6 – 10^7 electrons per photoelectron. Should multiple photons hit the photocathode simultaneously, the output voltage increases proportionally. The resulting current pulse is transmitted via long coaxial cables to the front-end electronics. A schematic of the 17-inch and 20-inch PMTs is shown in Figure 3·3.

The 17-inch PMTs are Hamamatsu R7250 devices, while the 20-inch PMTs consist of Hamamatsu R1449 and R3600 models originally deployed in the Kamiokande experiment. All PMTs employ bialkali photocathodes sensitive to wavelengths between approximately 300 and 650 nm, well matched to the emission spectrum of the liquid scintillator. The 17-inch PMTs utilize a “box-and-line” dynode structure, whereas the 20-inch PMTs employ a “venetian-blind” design. As a result, the 17-inch PMTs exhibit superior transit-time spread, while the 20-inch PMTs provide higher photon collection efficiency. It should also be noted that the 17-inch and 20-inch PMTs both have the same physical footprint, where the 17-inch PMTs have a 20-inch-diameter-photocathode that is ‘masked’ down to a 17-inch diameter. This masking improves the overall timing resolution. The total photocathode coverage of the inner detector

is approximately 34%, with 23% contributed by the 17-inch PMTs.

The performance of large-area PMTs is sensitive to external magnetic fields. To mitigate distortions caused by the Earth’s magnetic field, KamLAND is equipped with a system of geomagnetic compensation coils. These coils reduce the residual magnetic field inside the detector volume to below 50 mG, rendering its effect on PMT performance negligible. An additional key parameter governing PMT performance is the quantum efficiency (QE), defined as the probability that an incident photon produces a photoelectron. The QE depends strongly on photon wavelength. To optimize light collection, the KamLAND liquid scintillator is doped with the wavelength shifter 2,5-diphenyloxazole (PPO), which shifts scintillation photons into the spectral region where PMT QE is maximal. Figure 3.4 compares the PMT QE curve with the PPO emission spectrum.

Another important characteristic of PMTs is their quantum efficiency (QE). The QE quantifies the probability that a photon arriving on the photocathode will produce a photoelectron. A PMT’s QE varies over the wavelength of the incoming light. To improve our light collection, KamLAND’s LS is doped with PPO to shift the wavelength of the incoming light to where the PMTs are most sensitive. Figure 3.4 shows the PMT QE curve and the PPO reemission spectrum.

Finally, the 13 m-diameter outer balloon (OB) is suspended at the center of the inner detector and immersed in the buffer oil. The OB contains approximately one kiloton of highly purified organic liquid scintillator, which serves as the primary active target volume of the KamLAND experiment. In the KamLAND-Zen configuration, this volume also provides the immediate shielding and detection medium surrounding the xenon-loaded inner balloon.

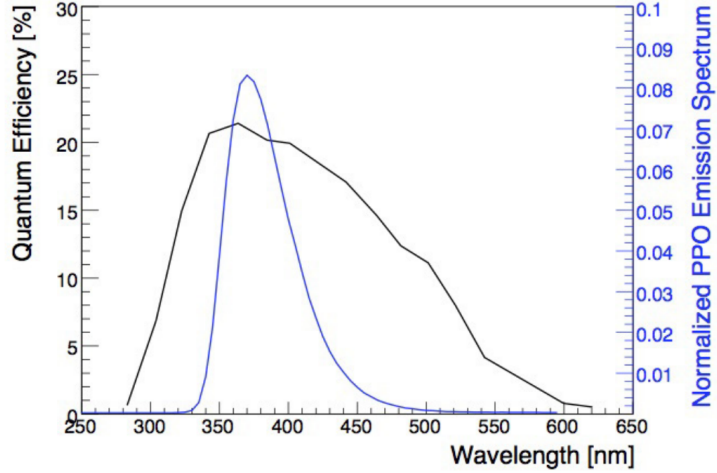


Figure 3·4: Quantum Efficiency of the KamLAND inner PMTs and PPO emission over wavelength. Figure from Reference [46].

3.1.1 Liquid Scintillator Targets

Liquid scintillator (LS) serves as the active detection medium of KamLAND and is essential for sensitizing the detector to low-energy radioactive processes. Charged particles traversing the LS excite molecular states that subsequently de-excite through the emission of scintillation photons. These photons are detected by the surrounding photomultiplier tubes, enabling precise reconstruction of event energy, position, and timing.

The KamLAND liquid scintillator (KamLS), which fills the volume between the outer balloon and the inner balloon, is composed of a carefully optimized mixture of organic compounds designed to maximize light yield, optical transparency, chemical stability, and radiopurity. The scintillator consists of 80.2% dodecane (D12) and 19.8% pseudocumene (PC), with the wavelength shifter 2,5-diphenyloxazole (PPO) added at a concentration of 1.36 ± 0.03 g/L. Pseudocumene acts as the primary scintillating solvent, while dodecane serves as a diluent that improves chemical stability and suppresses radioactive impurities.

Scintillation light produced in pseudocumene peaks in the ultraviolet region. PPO

absorbs this ultraviolet light and re-emits it at longer wavelengths, typically around 350–380 nm, where the quantum efficiency of the KamLAND PMTs is highest. This wavelength-shifting process significantly enhances photon detection efficiency and improves the detector’s energy resolution.

Achieving extremely low levels of radioactive contamination in the KamLS is critical for the success of KamLAND-Zen, as trace impurities from natural decay chains can mimic or obscure rare double-beta decay signals. Through extensive purification procedures, including water extraction, distillation, and nitrogen purging, KamLAND-Zen has achieved contamination levels of approximately 5×10^{-18} g/g for ^{238}U and 1.3×10^{-17} g/g for ^{232}Th . These values represent some of the lowest radioactive impurity concentrations ever realized in a large-scale liquid scintillator detector.

The chemical composition and relevant physical properties of the KamLAND liquid scintillator components are summarized in Table 3.1. The densities, boiling points, and flash points of the constituent materials are particularly important for detector safety, thermal stability, and purification system design.

	D12	PC	PPO
Chemical Formula	C ₁₂ H ₂₆	C ₉ H ₁₂	C ₁₅ H ₁₁ NO
Density [g/cm ³]	0.7526	0.8796	-
Boiling Point [°C]	216	169	360
Melting Point [°C]	-10	-44	72
Flash Point [°C]	83	54	-

Table 3.1: Composition and physical properties of the KamLAND liquid scintillator (KamLS). Values are taken from Reference [45].

3.1.2 KamLAND-Zen and XeLS

The KamLAND-Zen experiment modifies the central region of the KamLAND detector by introducing xenon-loaded liquid scintillator (XeLS) contained within a transparent inner balloon (IB) of radius approximately 1.9 m. This configuration places the double-beta decay isotope ^{136}Xe at the most radiopure and well-shielded location in the detector, maximizing sensitivity to neutrinoless double-beta decay.

The xenon gas is enriched to approximately 90% in ^{136}Xe and is dissolved into a modified version of the KamLAND liquid scintillator. The addition of xenon reduces the scintillation light yield by roughly 10%. To compensate for this effect, the PPO concentration in the XeLS is increased to approximately 4 g/L, restoring the overall light output and preserving energy resolution. The XeLS density is carefully adjusted to closely match that of the surrounding KamLS, thereby minimizing buoyant forces and mechanical stress on the inner balloon.

The precise chemical composition of the XeLS has evolved over different phases of the KamLAND-Zen experiment, reflecting changes in xenon loading and optimization of detector performance. Table 3.2 summarizes the relative concentrations of decane, pseudocumene, PPO, and xenon for KamLAND-Zen 400 Phase-1, Phase-2, and KamLAND-Zen 800. The increased xenon concentration in the KamLAND-Zen 800 phase significantly enhances the available source mass for double-beta decay while maintaining acceptable optical and mechanical properties.

3.2 Chemical Handling Infrastructure

Background mitigation is a central requirement for a successful search for neutrinoless double-beta decay ($0\nu\beta\beta$). In KamLAND-Zen, maintaining ultra-high chemical purity of all liquid volumes is essential, as trace radioactive contaminants can produce backgrounds in the energy region of interest or generate long-lived daughter isotopes

Material	Decane (%)	PC (%)	PPO (%)	Xe (%)
Zen 400 Phase-1	82.3	17.7	2.7	2.44/2.48
Zen 400 Phase-2	80.7	19.3	2.29±0.03	2.91
Zen 800	82.4	17.6	2.38±0.02	3.13

Table 3.2: Chemical composition of the xenon-loaded liquid scintillator (XeLS) for the different phases of the KamLAND-Zen experiment. Values are taken from Reference [47].

that are difficult to remove through event selection alone. In addition, gaseous impurities such as radon can diffuse into the detector and introduce time-dependent backgrounds.

To address these challenges, KamLAND and KamLAND-Zen employ a comprehensive chemical handling and purification infrastructure designed to remove radioactive contaminants, suppress radon ingress, and preserve the optical properties of the liquid scintillator and xenon-loaded liquid scintillator. In this section, the major purification and handling systems used for the liquid scintillator (LS), buffer oil, and XeLS are described.

3.2.1 Water Extraction

The first stage of purification for both the liquid scintillator and buffer oil is performed using a water extraction system, shown schematically in Figure 3.5. Prior to entering the extraction column, the liquids are filtered in two stages using filters with pore sizes of $1\text{ }\mu\text{m}$ and $0.1\text{ }\mu\text{m}$ to remove particulate contamination introduced during handling, circulation, or detector operations.

Following filtration, the liquids are passed through a counter-flow water extraction tower, where they are brought into contact with ultra-pure water. Many metallic impurities, including uranium, thorium, potassium, and their daughter isotopes, exhibit higher solubility in water than in the organic scintillator and preferentially migrate

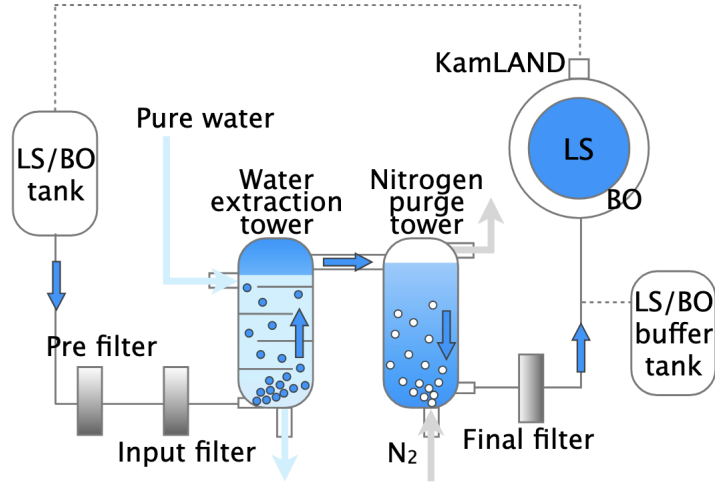


Figure 3·5: Flow diagram of the water extraction and nitrogen purge system. Figure from Reference [48].

into the aqueous phase. This process effectively removes a broad class of radioactive contaminants that cannot be eliminated through filtration alone.

After water extraction, the liquids are subjected to nitrogen purging using ultra-high-purity nitrogen gas. This step removes dissolved gases such as radon, oxygen, and other electronegative species. The removal of radon is particularly critical, as radon progeny can plate out onto detector surfaces or remain suspended in the scintillator, producing backgrounds in the $0\nu\beta\beta$ energy region. Oxygen removal also improves scintillation light yield and long-term optical stability.

3.2.2 Distillation

Further purification of the liquid scintillator is achieved using a dedicated distillation system, illustrated in Figure 3·6. Distillation provides one of the most powerful methods for removing both radioactive contaminants and optically active impurities, taking advantage of differences in boiling points between scintillator components and contaminants.

Liquid scintillator from KamLAND is continuously circulated through the distilla-

tion system during purification campaigns. In the distillation column, the scintillator mixture is heated and separated into its primary chemical components, most notably pseudocumene (PC) and PPO. Each component is distilled independently under controlled conditions, allowing heavy metal contaminants, oxidation products, and other non-volatile impurities to be efficiently separated and discarded.

After distillation, the purified components are recombined in a dedicated mixing tank to reproduce the original KamLAND liquid scintillator composition. The relative concentrations of PC, dodecane, and PPO are controlled with high precision, achieving density reproducibility at the level of 10^{-3} g/cm³. Maintaining precise density control is important both for detector stability and for matching the density of adjacent liquid volumes.

As in the water extraction stage, the recombined scintillator is purged with high-purity nitrogen gas prior to reintroduction into the detector. This final purge eliminates residual dissolved gases and minimizes the introduction of airborne radon during transfer. The distillation system has played a crucial role in achieving and maintain-

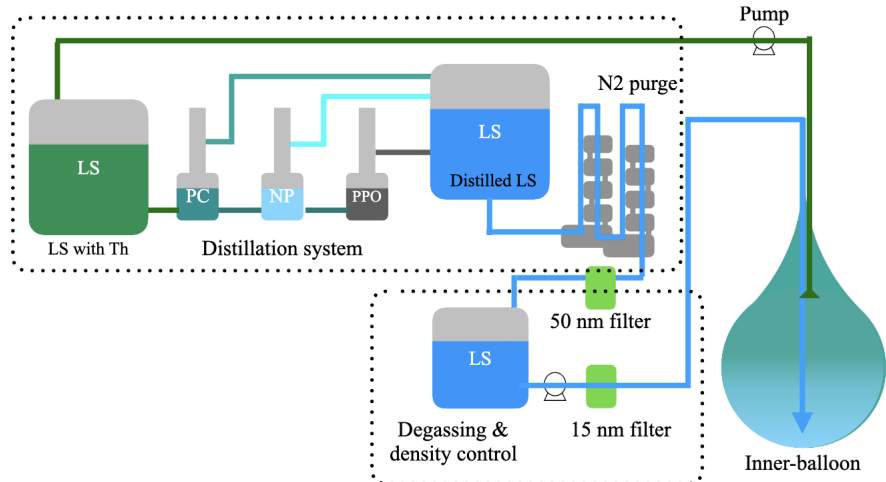


Figure 3·6: Flow diagram of the KLZ distillation and circulation system. Figure from Reference [45].

ing the ultra-low background levels required for KamLAND-Zen.

3.2.3 Xenon Handling

The handling of xenon-loaded liquid scintillator (XeLS) requires a specialized system capable of safely extracting, purifying, storing, and reintroducing xenon while preserving scintillator purity and maintaining precise control over chemical composition. A schematic overview of the XeLS handling system is shown in Figure 3.7.

The xenon handling system consists of several interconnected tanks and control components, each designed to perform a specific function in the xenon extraction and loading process:

- **Main Tank (1.1 m^3):** The main tank is directly connected to the KamLAND-Zen inner balloon. During xenon extraction, XeLS is transferred from the inner balloon into this tank, which serves as the initial collection and staging point for subsequent processing.
- **Reservoir Tank (1.1 m^3):** The reservoir tank is connected to the main tank via a vacuum pump and a liquid scintillator trap. The tank is cooled to approximately -50°C using liquid nitrogen, causing organic scintillator vapors to condense and be trapped while allowing xenon gas to pass through. This step effectively separates xenon from the scintillator without introducing additional chemical contaminants.
- **Storage Tank (25 m^3):** The degassed liquid scintillator remaining after xenon extraction is transferred to a large storage tank for temporary containment. This tank allows the scintillator to be stored safely while xenon purification or system maintenance is performed.
- **Sub-Tank (1.1 m^3):** The sub-tank serves as the primary mixing volume for

re-dissolving purified xenon gas into liquid scintillator. Xenon is introduced into the scintillator under controlled conditions to ensure uniform dissolution. The density and composition of the XeLS are continuously monitored during this process.

- **Control Tank (1.1 m^3):** The control tank is connected to the sub-tank and the second purification area and is used to fine-tune the chemical composition of the XeLS. By adjusting the relative concentration of dodecane, the control tank enables precise control of the XeLS density, ensuring compatibility with the surrounding KamLAND liquid scintillator. The tank is pressurized with high-purity nitrogen gas to prevent air ingress and radon contamination.

After mixing and density adjustment, the XeLS is filtered and gradually returned to the inner balloon. This carefully controlled procedure minimizes mechanical stress on the balloon, suppresses the introduction of impurities, and ensures stable long-term detector operation. The xenon handling system has been essential for multiple KamLAND-Zen phases, enabling xenon extraction, purification, and reloading campaigns while maintaining the radiopurity required for world-leading $0\nu\beta\beta$ searches.

3.3 Data Acquisition

3.3.1 KamLAND DAQ

The KamLAND data acquisition (DAQ) system is responsible for reading out, digitizing, triggering, and recording signals from the nearly 2,000 photomultiplier tubes instrumenting the detector. The DAQ must accommodate a wide dynamic range of event energies, from low-energy radioactive decays to high-energy cosmic-ray muons, while maintaining high livetime and stable operation over long data-taking periods.

To meet these requirements, KamLAND employs two DAQ systems operating in parallel. The primary system, KamFEE (KamLAND Front-End Electronics), has

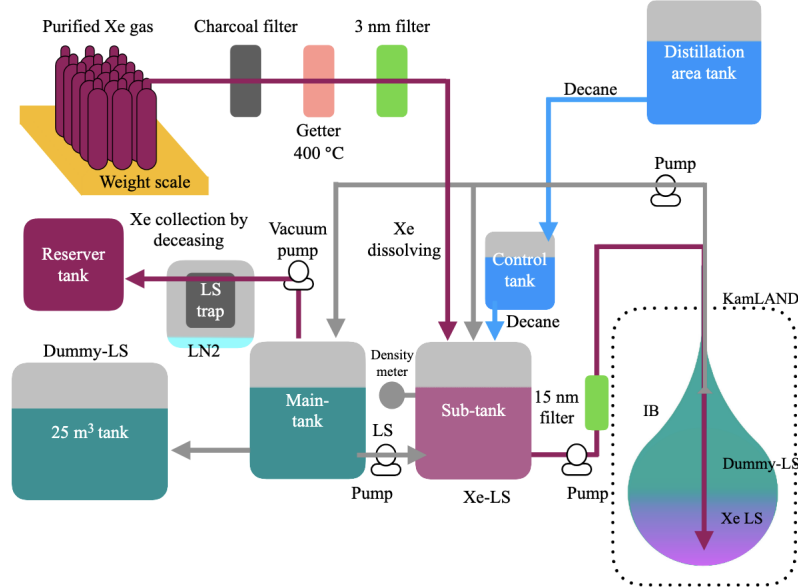


Figure 3.7: Flow diagram of the KLZ Xenon system. The purple lines denote the flow of Xe/XeLS, the blue line denotes the flow of decane, and the grey line denotes the flow of LS. Figure from Reference [45].

been used since the beginning of KamLAND physics data-taking and provides reliable readout for the majority of events. The secondary system, MoGURA (Module for General-Use Rapid Application), was developed to mitigate deadtime and waveform distortions following high-energy cosmic-ray muon events. An overview of the dual DAQ architecture and data flow is shown in Figure 3.8. Together, these systems ensure efficient readout across a broad range of event types and energies.

3.3.2 KamFEE DAQ

KamFEE constitutes the primary front-end electronics system for KamLAND and is responsible for reading out and controlling all inner detector PMTs. The KamFEE modules are implemented in VME 9U form-factor boards and are synchronized using a global 40 MHz system clock to ensure precise timing alignment across channels. Signals from each PMT are split into two parallel processing paths. The first path is routed to a discriminator, which registers a PMT hit when the signal exceeds a

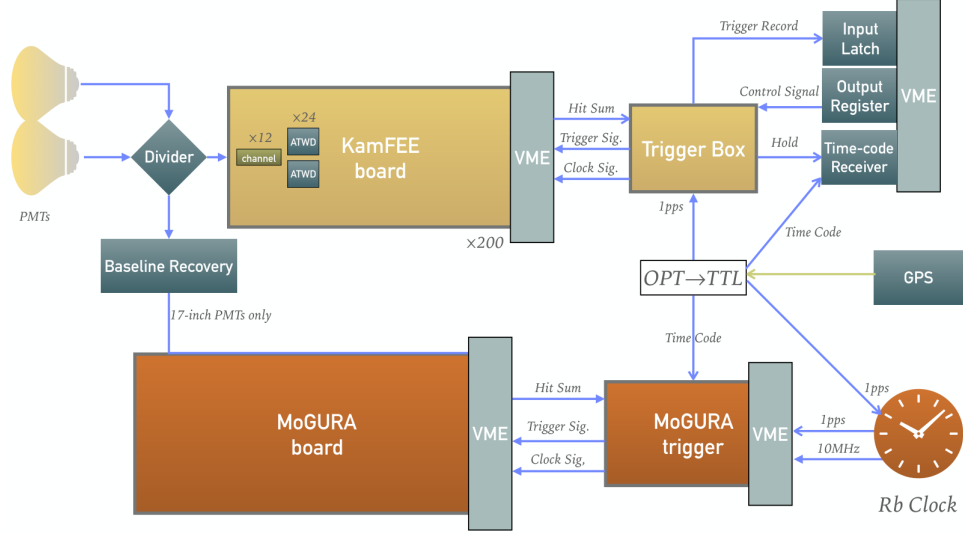


Figure 3.8: Flow diagram of the KamLAND data acquisition system, taken from Reference [49].

predefined threshold corresponding to approximately one-sixth of a single photoelectron. This low threshold allows KamLAND to maintain high efficiency for low-energy events while suppressing electronic noise.

The second signal path is delayed to allow time for the discriminator decision and is subsequently fed into three parallel amplification stages with gains of $\times 20$, $\times 4$, and $\times 0.5$. These gain stages provide sensitivity across a wide dynamic range, enabling accurate digitization of both small scintillation signals and large pulses from energetic events. The amplified signals are digitized by analog transient waveform digitizers (ATWDs). Each ATWD is a 10-bit digitizer that samples the waveform at 1.5 ns intervals for 128 consecutive samples, corresponding to a total waveform window of approximately 192 ns. The digitization of a single waveform requires approximately 128 μ s, during which time the ATWD cannot accept new signals.

To initiate digitization, each KamFEE board generates a “hitsum” signal that encodes the number of PMTs registering hits within a predefined time window. This hitsum is sent to the central KamFEE trigger logic, which applies global trigger con-

ditions based on the total number of hits. If the trigger condition is satisfied, a digitization command is issued back to the KamFEE boards. Because the ATWDs are inactive during digitization, KamFEE assigns two ATWDs to each channel and alternates between them, thereby reducing deadtime. Nevertheless, following large energy depositions—such as cosmic-ray muon events—the KamFEE system can experience extended deadtime due to waveform saturation and recovery effects. These limitations motivated the development of a complementary DAQ system optimized for post-muon recovery.

3.3.3 MoGURA

MoGURA is a secondary DAQ system designed to address limitations of the KamFEE system in the aftermath of high-energy cosmic-ray muon events. Although KamLAND is located deep underground, the residual cosmic muon rate is approximately 0.3 Hz. These muons deposit large amounts of energy in the detector, saturating front-end electronics and producing long-lasting after-pulses and waveform overshoots that can obscure low-energy signals occurring shortly afterward. To mitigate these effects, MoGURA incorporates several features beyond those of KamFEE:

- **Baseline Recovery:** Following a large energy deposition, PMT signals may exceed the digitization range, resulting in waveform saturation. As the signal returns to baseline, it often exhibits a pronounced overshoot, during which the baseline voltage drops below its nominal value. MoGURA implements baseline restoration techniques that allow reliable digitization of subsequent signals during this recovery period.
- **Adaptive Trigger Mode:** After the detection of a muon event, MoGURA activates a specialized trigger mode optimized for the identification of post-muon activity. This adaptive trigger relies on differential PMT hit patterns and

timing information to maintain sensitivity to low-energy events despite elevated noise and after-pulse rates.

In addition to mitigating deadtime, MoGURA plays a critical role in identifying neutrons produced by muon spallation in the detector. These neutrons are typically captured on protons, emitting a 2.2 MeV gamma ray with a characteristic delay. MoGURA’s improved post-muon sensitivity enables efficient tagging of these spallation neutrons, which are essential for rejecting cosmogenic backgrounds in KamLAND-Zen analyses.

The baseline recovery and neutron-tagging capabilities of MoGURA will be further enhanced in the planned MoGURA2 trigger system. MoGURA2 is designed as a next-generation replacement for both KamFEE and MoGURA in the KamLAND2-Zen experiment, incorporating modern digitization hardware and real-time processing. KamLAND2-Zen is expected to begin physics data-taking in the late 2020s, with MoGURA2 serving as a key component of its upgraded DAQ architecture.

3.4 KamLAND-Zen Phases

The KamLAND-Zen experiment has undergone multiple operational phases, each corresponding to significant upgrades in detector configuration, xenon mass, and background control. These phases were designed to incrementally improve sensitivity to $0\nu\beta\beta$ decay by increasing exposure while simultaneously reducing background levels. In this section, the major KamLAND-Zen phases are described, with emphasis on the evolution of detector design and background mitigation strategies.

3.4.1 KamLAND-Zen 400

The first implementation of KamLAND-Zen began in 2011 with the installation of an inner balloon and xenon-loaded liquid scintillator at the center of the KamLAND

detector, inaugurating the phase known as KamLAND-Zen 400. This configuration featured a spherical inner balloon with a diameter of approximately 3 m, filled with liquid scintillator loaded with about 3% xenon by weight. The xenon gas was enriched to approximately 91% in the double-beta decay isotope ^{136}Xe , corresponding to an active isotope mass of roughly 400 kg.

KamLAND-Zen 400 data-taking was divided into two distinct periods, referred to as Phase-1 and Phase-2, reflecting major differences in background conditions and purification status. During Phase-1, the data were affected by a significant background contribution from the metastable isotope $^{110\text{m}}\text{Ag}$. This contamination was traced to the inner balloon film, with the silver believed to have been introduced during balloon fabrication. The presence of $^{110\text{m}}\text{Ag}$ was likely associated with radioactive fallout from the Fukushima Daiichi nuclear accident, which occurred during the manufacturing period of the inner balloon and in the same geographic region of Japan. The long half-life of $^{110\text{m}}\text{Ag}$ and its beta decay energy made it a particularly challenging background for the $0\nu\beta\beta$ search. To address this issue, extensive purification of the xenon-loaded liquid scintillator was carried out through multiple distillation campaigns. These efforts reduced the $^{110\text{m}}\text{Ag}$ background by approximately a factor of 20, enabling the start of Phase-2 data-taking under significantly improved background conditions.

Phase-2 accumulated a total livetime of 534.5 days. The combined analysis of Phase-1 and Phase-2 data resulted in a lower limit on the neutrinoless double-beta decay half-life of ^{136}Xe of $T_{1/2}^{0\nu} > 1.07 \times 10^{25}$ years at 90% confidence level. This corresponds to an upper limit on the effective Majorana neutrino mass in the range $m_{\beta\beta} < 61\text{--}165\text{ meV}$, depending on the choice of nuclear matrix element calculation.

3.4.2 KamLAND-Zen 800

KamLAND-Zen 800 represents the second major phase of the KamLAND-Zen experiment and was designed to significantly extend sensitivity by increasing the xenon mass and improving radiopurity. Data-taking for KamLAND-Zen 800 began in January 2019 and continued through August 2024. Over this period, the experiment accumulated more than 2 kiloton·years of exposure.

The KamLAND-Zen 800 phase employed a substantially upgraded inner balloon and increased the xenon loading to approximately 745 kg of enriched xenon. In addition to the larger source mass, major emphasis was placed on improving inner balloon cleanliness and reducing contamination from both intrinsic radioactivity and cosmogenic backgrounds. Following the conclusion of data-taking, KamLAND-Zen 800 was decommissioned in the fall of 2024 and is currently in the process of disassembly.

A key upgrade in KamLAND-Zen 800 was the fabrication and deployment of a larger and significantly cleaner inner balloon. The balloon was manufactured at Tohoku University in a class-1 cleanroom to minimize particulate and radioactive contamination. It was constructed from panels of 25 μm -thick nylon-6 film, selected for its mechanical strength, chemical compatibility with liquid scintillator, and low intrinsic radioactivity. The inner balloon fabrication process consisted of multiple carefully controlled steps, several of which are listed below:

- **Washing:** The nylon film was cleaned twice using an ultrasonic bath and subsequently stored between protective cover films to prevent dust adhesion.
- **Welding:** Cleaned balloon panels were welded using a semi-automatic welding machine. For mechanically delicate regions, such as the balloon neck, a hand-operated welding machine was employed. After welding, the average tensile strength across the balloon surface was approximately 35 N/cm.

- **Helium Leak Check:** Helium gas was injected into the assembled balloon to identify leaks introduced during fabrication. Prior to this step, the protective cover films were removed. Identified leaks were repaired by patching the nylon film. In total, more than 900 leaks were detected and sealed.
- **Folding:** After leak checking, the inner balloon was folded into a cylindrical configuration and covered with protective sheath films to prevent contamination during transport. Teflon sheets and Vectran strings were used to secure the folded balloon.
- **Shipping:** The balloon and associated tools were transported in sealed silver gas bags to minimize exposure to airborne contaminants.

The inner balloon was installed on May 10, 2018. Prior to final installation, a full rehearsal deployment was performed in a swimming pool to validate procedures and minimize operational risk. During the final installation, the balloon was deployed through the 50 cm access port at the top of the KamLAND detector. After initial filling with KamLAND liquid scintillator, the protective Teflon sheets, sheath films, and Vectran strings were carefully removed. The entire deployment was monitored in real time using cameras and an endoscope.

The top of the inner balloon is connected to a corrugated tube fabricated from polyether ether ketone (PEEK), providing mechanical flexibility and chemical compatibility. The balloon is supported by twelve suspension belts that wrap around its full height. The tension in each belt is continuously monitored to ensure positional stability and to detect any mechanical abnormalities. A schematic of the inner balloon structure and its key dimensions is shown in Figure 3.9.

Once deployed and immersed in liquid scintillator, the inner balloon becomes extremely difficult to access or clean. Consequently, contamination control during

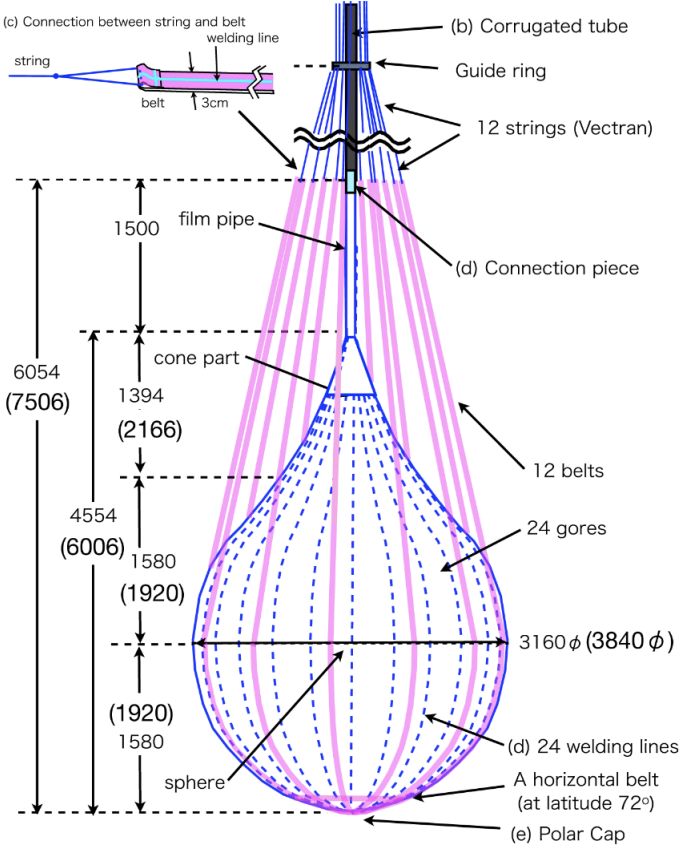


Figure 3.9: Inner balloon structure and measurements for KamLAND-Zen 800 configuration, taken from Reference [45].

fabrication, installation, and early operation is critical for long-term detector performance.

Following deployment, the inner balloon was initially filled with distilled liquid scintillator, during which the ^{232}Th contamination level was measured to be approximately 10^{-15} g/g , exceeding the target background concentration. Subsequent investigations identified the PPO distillation tower as a potential source of contamination. Detailed studies using inductively coupled plasma mass spectrometry (ICP-MS) and neutron activation analysis were performed at multiple locations along the distillation system to localize the contamination source. After extensive cleaning, filter replacement, and system refurbishment, additional liquid scintillator purification campaigns

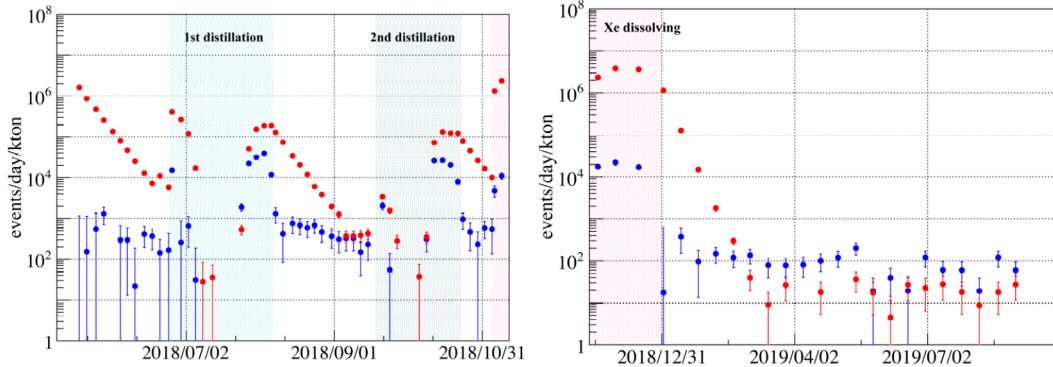


Figure 3.10: Coincidence event rate in KamLAND-Zen 800 during the first distillation campaign, second distillation campaign, and xenon loading phase. The red points denote ^{214}Bi and the blue points denote ^{212}Bi . Figure from Reference [49].

were conducted. Two major distillation campaigns resulted in a reduction of ^{238}U and ^{232}Th contamination levels by approximately an order of magnitude compared to KamLAND-Zen 400.

Residual contamination levels were monitored using delayed coincidence analyses of the $^{214}\text{Bi}-^{214}\text{Po}$ and $^{212}\text{Bi}-^{212}\text{Po}$ decay sequences. The time evolution of these coincidence event rates is shown in Fig. 3.10, and the resulting contamination levels for each KamLAND-Zen phase are summarized in Table 3.3.

KamLAND-Zen 800 was decommissioned in 2024 after accumulating more than 2 kiloton·years of exposure. The final analysis yielded a lower limit on the neutrinoless double-beta decay half-life of $T_{1/2}^{0\nu} > 3.8 \times 10^{26}$ years at 90% confidence level. This result corresponds to an effective Majorana neutrino mass constraint in the range

	^{238}U (10^{-17} g/g)	^{232}Th (10^{-17} g/g)
Zen 400 Phase-1	13 ± 2	190 ± 20
Zen 400 Phase-2	17 ± 1	5.5 ± 0.3
Zen 800	1.5 ± 0.4	30 ± 4

Table 3.3: Balloon film contamination levels from the last three phases of KamLAND-Zen. Values taken from Reference [45].

28–122 meV, depending on nuclear matrix element assumptions. As of mid-2025, this represents the world-leading limit on the effective Majorana mass from any double-beta decay isotope and provides the only experimental constraint fully covering the inverted neutrino mass ordering.

3.4.3 KamLAND2-Zen

KamLAND2 is the next-generation upgrade of the KamLAND experiment and will be constructed in the same underground cavern as the original KamLAND detector. Building on more than two decades of operational experience, KamLAND2 is designed to significantly improve detector performance through comprehensive upgrades to the photodetectors, optical coverage, inner balloon technology, and data acquisition system. The KamLAND2-Zen program, which incorporates a xenon-loaded liquid scintillator target, aims to reach a neutrinoless double-beta decay half-life sensitivity of $T_{1/2}^{0\nu\beta\beta} > 2 \times 10^{27}$ years, corresponding to sensitivity well into the inverted neutrino mass ordering region.

Achieving this goal requires both increased exposure and substantial reductions in background rates, particularly from the tail of the two-neutrino double-beta decay spectrum and residual radioactive contamination. To this end, most major detector components will be replaced or upgraded in the transition from KamLAND to KamLAND2. The most significant upgrades are summarized below.

- **Inner Detector PMTs:** All 1,879 inner detector PMTs will be replaced with modern photodetectors featuring significantly improved quantum efficiency and reduced transit time spread (TTS). These new PMTs are expected to provide higher photon detection efficiency and superior timing performance, leading to improved energy and vertex reconstruction. The reduction in TTS is particularly important for enhancing position resolution and background discrimination

in large-volume liquid scintillator detectors.

- **Light-Collecting Mirrors:** Winston cone light concentrators will be installed on each PMT to dramatically increase the effective photocathode coverage, approaching nearly 100% optical coverage of the inner detector. By redirecting otherwise lost photons onto the PMT photocathodes, these concentrators substantially increase light yield. Together with the upgraded PMTs, this improvement is expected to achieve a target energy resolution of approximately 2% at the ^{136}Xe $0\nu\beta\beta$ Q -value. Such an energy resolution would suppress the contribution from the high-energy tail of the two-neutrino double-beta decay spectrum by roughly two orders of magnitude, greatly reducing one of the dominant irreducible backgrounds.
- **Improved Inner Balloon:** The KamLAND2-Zen inner balloon will be constructed from polyethylene naphthalate (PEN), a material that exhibits intrinsic scintillation. Unlike nylon-based films used in previous phases, PEN allows radioactive decays occurring within the balloon film itself to produce detectable scintillation light. This property enables active tagging and rejection of background events originating from the balloon material, significantly reducing backgrounds associated with surface contamination while maintaining mechanical strength and chemical compatibility with liquid scintillator.
- **MoGURA2 DAQ System:** The existing dual DAQ architecture (KamFEE and MoGURA) will be replaced by MoGURA2, a newly developed, compact, deadtime-free data acquisition system based on RFSoC (Radio Frequency System-on-Chip) technology. MoGURA2 integrates high-speed digitization, real-time signal processing, and flexible trigger logic within a single platform. This system is designed to provide continuous waveform acquisition without deadtime,

improved post-muon recovery, and enhanced neutron tagging capability, all of which are critical for high-sensitivity rare-event searches.

With these upgrades, KamLAND2-Zen will combine increased source mass, improved energy resolution, and enhanced background rejection to achieve an unprecedented sensitivity to $0\nu\beta\beta$ decay. Construction and commissioning of KamLAND2-Zen are ongoing, with the start of physics data-taking currently planned for 2028.

Chapter 4

Event Reconstruction and Selection

Precise event reconstruction and robust background discrimination are essential for rare-event searches such as neutrinoless double-beta decay. In KamLAND-Zen, these tasks rely on a detailed understanding of the detector response, which is achieved through a combination of high-fidelity Monte Carlo (MC) simulations and calibration data. Detector simulations are performed using KLG4Sim, a GEANT4-based software framework that models particle interactions, scintillation light production, photon propagation, and photomultiplier tube (PMT) response in the KamLAND detector.

Simulated events are tuned using real calibration data to accurately reproduce the detector’s energy scale, resolution, timing response, and spatial reconstruction performance. Both simulated and physical events produce digitized PMT waveforms, which are reconstructed to extract higher-level observables such as event energy, vertex position, and event topology. These reconstructed quantities form the basis of event selection, background rejection, and spectral fitting.

This chapter describes the simulation framework, reconstruction algorithms, and event selection procedures used in the KamLAND-Zen 800 analysis. Emphasis is placed on the data processing flow from raw waveforms to physics-level observables, as well as the reconstruction techniques that enable precise energy and position determination in a large liquid scintillator detector.

4.1 Analysis Framework

The KamLAND-Zen analysis framework is designed to process large volumes of raw detector data and transform them into physics-ready datasets suitable for rare-event searches. This framework integrates data from multiple data acquisition systems, applies waveform-level reconstruction algorithms, and produces standardized analysis files used throughout the collaboration.

4.1.1 Data Flow

Figure 4·1 illustrates the data flow in KamLAND-Zen, from raw photomultiplier tube signals to high-level analysis variables. PMT signals are digitized by either the KamFEE or MoGURA data acquisition systems, as described in the previous chapter. These systems record waveform-level information with precise timing, enabling detailed reconstruction of scintillation light signals. The digitized PMT waveforms are stored in the Kinoko Data Format (KDF). Each KDF file contains trigger information, timestamped waveform data for all PMTs participating in an event, and run-dependent metadata such as detector configuration and operational conditions recorded in the file header. The KDF format serves as the lowest-level persistent data product in the KamLAND-Zen analysis chain.

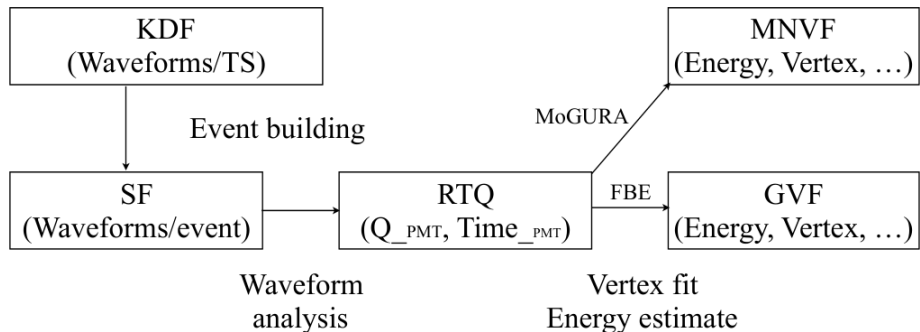


Figure 4·1: Data flow in KamLAND from raw waveforms to analysis variables such as energy, vertex, and total hit PMTs. Taken from Reference [45].

An EventBuilder process groups individual PMT waveforms belonging to a single trigger into a coherent event record and stores this information in a serialized event file. These event records are subsequently processed by a waveform analysis module, which extracts hit-level information from each PMT waveform. Specifically, the waveform analyzer reconstructs the hit time and integrated charge for each PMT pulse, producing time–charge (TQ) information. The reconstructed TQ information for all PMTs is stored in Raw-TQ (RTQ) files. RTQ files form the primary input for event-level reconstruction algorithms. Using the hit timing and charge information contained in the RTQ files, event vertex positions and visible energies are reconstructed through likelihood-based fitting procedures described later in this chapter.

In addition to primary vertex and energy reconstruction, several secondary reconstruction and classification algorithms are applied at the RTQ level. These include muon track reconstruction, flasher PMT identification, double-pulse fitting for pileup rejection, and selections targeting unphysical or poorly reconstructed events. The outputs of these reconstruction stages are consolidated into a high-level analysis format known as the General Vector File (GVF). GVF files are the primary datasets used for physics analyses, including the analysis presented in this thesis. They contain reconstructed event quantities, quality metrics, and auxiliary information required for background rejection and spectral fitting.

GVF files contain a comprehensive set of reconstructed and derived quantities for each event, including:

- **Run number and event number**, uniquely identifying each recorded event.
- **TimeStamp**, based on the DAQ clock time (25 ns resolution for KamFEE and 20 ns for MoGURA).
- **Unix time**, defined as the number of seconds since January 1, 1970, which is used for run-dependent vetoes and time-correlated background studies.

- **Trigger type**, recording which hardware or software trigger initiated the event readout.
- **Event vertex and reconstruction quality**, including the reconstructed position, radial distance from the detector center, and a vertex fit quality parameter known as *Badness*.
- **Energy estimates**, including the visible energy reconstructed using all PMTs and the energy reconstructed using only the 17-inch PMTs (energy17).
- **Total collected charge**, summed separately for inner detector PMTs, 17-inch PMTs, and outer detector PMTs.
- **Hit multiplicities**, including the total number of hit PMTs and the number of hit 17-inch PMTs.
- **NsumMax**, the maximum number of PMT hits within a single DAQ cycle during the event, corresponding to the peak hit multiplicity.
- **N200OD**, the maximum number of outer detector PMT hits within a 200 ns window, used for muon identification.
- **Muon reconstruction parameters**, including estimated entrance position and direction for reconstructed muon tracks.

Finally, events recorded by the MoGURA DAQ are temporally associated with muon events acquired by the KamFEE system and stored in a Muon–Neutron Vector File (MNVF). This association enables efficient identification of neutron capture events occurring shortly after cosmic-ray muons, which is critical for spallation background rejection in KamLAND-Zen analyses.

4.2 Event Reconstruction

Event reconstruction in KamLAND-Zen converts digitized PMT waveforms into physically meaningful observables such as hit time, charge, event vertex, and visible energy. This process relies on detailed waveform analysis, careful correction of PMT-specific effects, and likelihood-based fitting algorithms that account for the optical and timing properties of the detector. In this section, the reconstruction procedures used in the KamLAND-Zen 800 analysis are described.

4.2.1 Waveform Analysis

Each PMT waveform digitized by the KamLAND data acquisition system consists of 128 samples taken at 1.5 ns intervals, corresponding to a total digitization window of 192 ns. These waveforms are processed to extract hit-level timing and charge information, collectively referred to as TQ (time–charge) values. The waveform analysis proceeds through the following steps:

- **Smoothing:** Each waveform is smoothed using a running-average first derivative to suppress high-frequency electronic noise while preserving the shape of physical pulses.
- **Baseline Adjustment:** The baseline level for each PMT is determined at the beginning of each run using dedicated pedestal measurements. This baseline is subtracted from each waveform to correct for channel-dependent offsets.
- **Peak Finding:** Signal peaks are identified using running-averaged first, second, and third derivatives of the waveform. This multi-derivative approach improves robustness against noise and allows for reliable identification of overlapping pulses.

- **Leading- and Trailing-Edge Tagging:** The leading edge of a pulse is defined as 10 ns prior to the peak voltage, providing a stable reference point for timing. The trailing edge is identified as the point where the waveform returns to the baseline level. An example of this time-stamping procedure is shown in Figure 4.2.
- **Waveform Integration:** The waveform is integrated between the leading and trailing edges to obtain the total collected charge associated with the pulse.

When multiple hits occur within a single PMT waveform, the reconstruction algorithm returns the total integrated charge of all hits and the earliest hit time. This simplified representation is sufficient for primary vertex and energy reconstruction, which are dominated by the earliest-arriving photons. Information about multi-photoelectron (multi-p.e.) structure is retained for specialized analyses, including double-pulse fitting and muon shower identification.

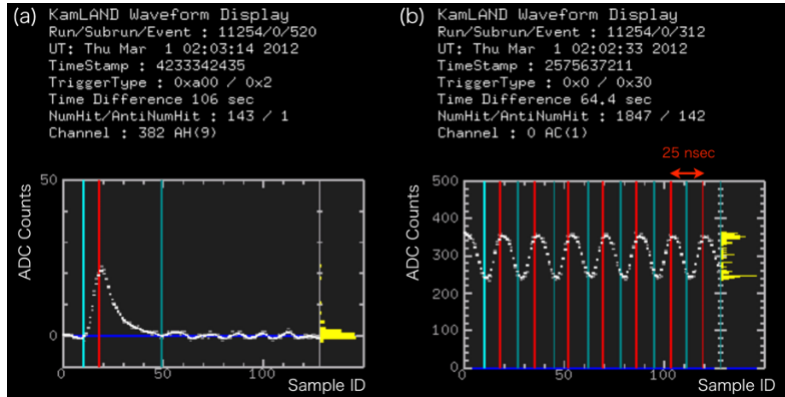


Figure 4.2: Example of waveform analysis from Reference [50]. (Left) ADC counts of a real PMT waveform after baseline subtraction. The left cyan line indicates the leading edge, the red line marks the peak position, and the right dark cyan line denotes the trailing edge. (Right) Clock calibration example illustrating 25 ns timing intervals.

4.2.2 PMT Corrections

Low Gain Problem and HV Reductions

Since approximately 2011, a gradual decrease in gain has been observed in a subset of the 17-inch PMTs. As PMT gain decreases, waveform amplitudes are reduced, degrading charge resolution and compromising the signal-to-background separation required for low-energy analyses. In many cases, PMTs were observed to enter a low-impedance state prior to the onset of gain loss. Each PMT channel is continuously monitored through high-voltage (HV) current and voltage readouts, enabling real-time detection of abnormal operating conditions. In many instances, a simple HV power cycle was sufficient to restore normal behavior. Beginning in 2016, an automatic HV power-cycling mechanism was implemented to mitigate this issue, although the underlying cause of the low-impedance behavior remains under investigation.

When a PMT repeatedly entered the low-impedance state, the applied high voltage was reduced in increments of 50–100 V to stabilize operation. Over time, some channels required cumulative HV reductions of up to 450 V. Figure 4.3 shows the evolution of the number of low-gain 17-inch PMTs prior to the KamLAND-Zen 800 phase. The gradual increase reflects aging effects, while the sudden steps correspond to HV reduction campaigns initiated after 2017.

Bad Channels

PMT channels exhibiting abnormal or unstable behavior are classified as bad channels and excluded from event reconstruction and physics analyses. A channel is designated as bad if it satisfies one or more of the following criteria:

- PMT pulses are recorded in fewer than 0.6% of all events.
- PMT pulses are recorded in fewer than 0.48% of non-muon events.

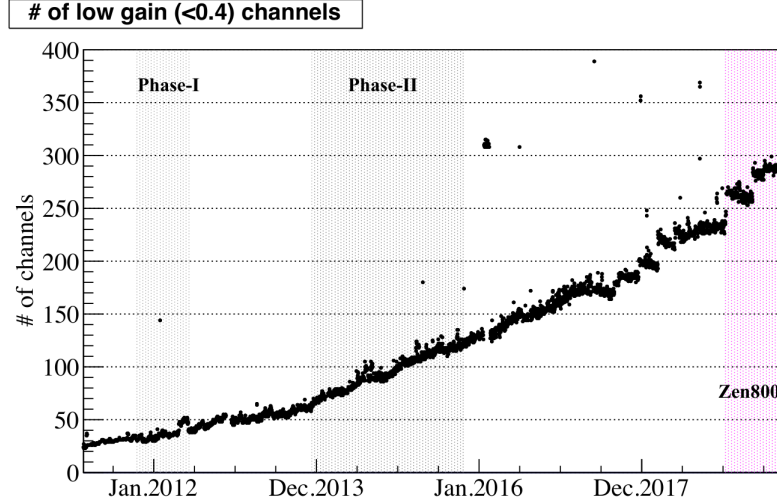


Figure 4.3: Trend in the number of low-gain 17-inch PMTs prior to KamLAND-Zen 800. The gradual increase reflects long-term PMT behavior, while sudden jumps correspond to HV reductions performed since 2017. Figure taken from Reference [45].

- PMT pulses are recorded in fewer than 80% of high-energy muon events.
- PMT waveforms are missing in more than 10% of events.
- A large discrepancy is observed between the two ATWD digitizations assigned to the channel.
- Excessively large charge is recorded during muon events. For this criterion, each run is divided into 100 muon intervals, and the following condition is applied:

$$\frac{1}{N_{\text{interval}}} \sum_{i=1}^{N_{\text{interval}}} \left(\frac{1}{N_{\mu\text{on}}} \sum_{j=1}^{N_{\mu\text{on}}} \frac{(Q_{\text{expected}} - Q_{\text{detected}})^2}{Q_{\text{expected}}} \right) > 1000 \text{ p.e.}$$

Here, Q_{detected} is the charge measured by the PMT and Q_{expected} is the average charge of neighboring PMTs. Channels flagged as bad are removed from all subsequent reconstruction and analysis steps.

Dark Hits

Thermal emission of electrons from the PMT photocathode can produce spontaneous signals known as dark hits. These hits constitute an unavoidable source of background at the single-PMT level. Although the underground environment and stable detector temperature help suppress dark rates, they remain non-negligible and must be accounted for in reconstruction algorithms. Dark hit rates are measured on a run-by-run basis and incorporated into the likelihood functions used for vertex and energy reconstruction. The dark rate for each PMT is estimated using a time window 50–100 ns before the rising edge of the waveform, where physical scintillation signals are not expected. An example PMT hit-time distribution and the dark-rate measurement window are shown in Figure 4·4.

4.2.3 Primary Vertex Fitter

The primary vertex fitter provides an initial estimate of the position of a scintillating event within the detector. This estimate serves as a seed for the more precise, but computationally intensive, secondary vertex reconstruction described in the next

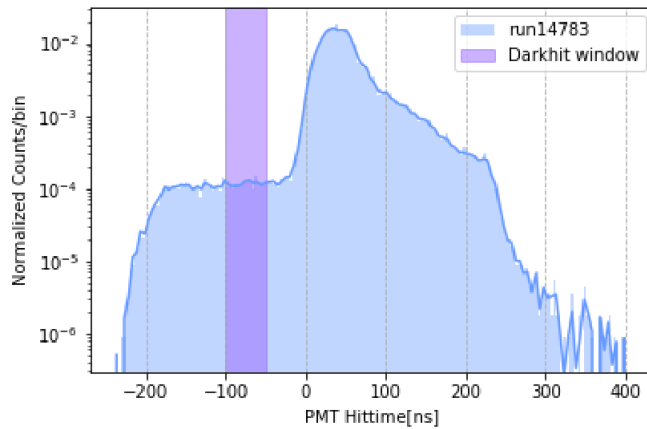


Figure 4·4: Example PMT hit-time distribution from data run 14783. The shaded region 50–100 ns before the rising edge is used to estimate the PMT dark hit rate. Figure taken from Reference [49].

subsection.

The primary fit is based on constructing a hit-time residual distribution for each PMT:

$$T_i^{\text{emit}} = T_i - \text{TOF}_i = T_i - \frac{|\mathbf{R}_i - \mathbf{r}_{\text{vertex}}|}{c_{\text{eff}}}, \quad (4.1)$$

Here, T_i is the measured hit time of the i th PMT, TOF_i is the time of flight for a scintillation photon traveling from the event vertex $\mathbf{r}_{\text{vertex}}$ to the PMT position \mathbf{R}_i , and c_{eff} is the effective speed of light in the scintillator medium. By adjusting $\mathbf{r}_{\text{vertex}}$ such that the distribution of T_i^{emit} matches the expected scintillation time profile, the primary fitter obtains an initial vertex estimate.

4.2.4 Secondary Vertex Fitter

The secondary vertex reconstruction, referred to as the V2 fitter, refines the event position and determines the absolute event start time T_0 using a likelihood-based approach. Starting from the primary vertex estimate, the fitter computes T_0 as a charge-weighted average of the PMT hit times:

$$T_0 = \frac{\sum_i (T_i^{\text{PMT}} - \text{TOF}_i^{\text{PMT}}) Q_i}{\sum_i Q_i} - \text{const.} \quad (4.2)$$

This T_0 represents the universal start time of the event. Using this reference, the time residual for each PMT hit is defined as:

$$\tau_i(x, y, z, T_0) = T_i^{\text{PMT}} - \text{TOF}_i^{\text{PMT}} - T_0. \quad (4.3)$$

The distributions of τ_i for 17-inch and 20-inch PMTs are characterized using probability density functions (PDFs) derived from calibration data, as shown in Figure 4.5. These PDFs account for differences in PMT transit-time spread and photon propagation effects. The likelihood contribution from an individual PMT is defined

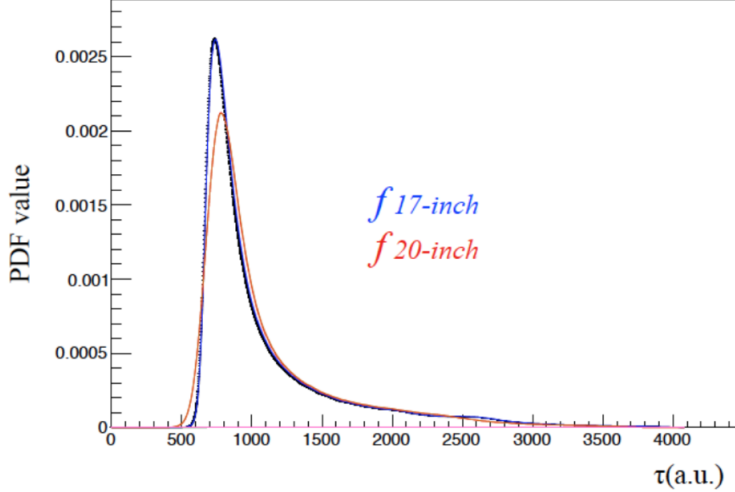


Figure 4.5: Probability density functions of 17-inch and 20-inch PMT hit-time residuals derived from calibration data. Figure taken from Reference [45].

as:

$$\phi_i = \frac{\mu f_i(\tau_i) + D_i}{\mu C_{17/20} + D_i}, \quad (4.4)$$

where μ is a pulse-shape normalization factor, $f_i(\tau_i)$ is the time residual PDF for the corresponding PMT type, D_i is the measured dark hit rate for the i th PMT, and $C_{17/20}$ is the normalization constant for the 17-inch or 20-inch PMT PDFs. The overall log-likelihood is then given by $\log \mathcal{L} = \sum_i \log(\phi_i)$. The V2 fitter maximizes this log-likelihood using the Newton–Raphson method, iteratively adjusting the parameters (x, y, z, T_0) to obtain the best-fit vertex position and event start time. The resulting V2-reconstructed vertex is used in all subsequent energy reconstruction and event selection steps.

4.2.5 Energy Reconstruction

Energy reconstruction in KamLAND-Zen is performed using a likelihood-based approach that combines information from PMT hit multiplicity, collected charge, and hit timing. This method allows for optimal use of the available detector information while accounting for position-dependent light collection, dark noise, and PMT

response variations. The reconstructed visible energy, E_{vis} , represents the total scintillation light produced by an event and serves as the primary observable for spectral analyses.

N_{hit} PDF

The expected number of detected photoelectrons at the i th PMT, μ_i , is modeled as a function of the event's visible energy and position:

$$\mu_i = a_i(x, y, z) \times E_{\text{vis}} + d_i, \quad (4.5)$$

where $a_i(x, y, z)$ is a position-dependent conversion factor that maps visible energy to the expected number of photons detected by PMT i . This factor encapsulates geometrical effects, optical attenuation, and PMT quantum efficiency, and is calibrated using neutron capture events. The term d_i represents the average dark noise contribution for PMT i , measured independently through electronic monitoring.

Assuming ideal Poisson statistics, the probability that j photoelectrons are detected by PMT i is given by

$$k_{ij} = \frac{(\mu_i)^j}{j!} e^{-\mu_i}. \quad (4.6)$$

In practice, KamLAND waveform analysis applies a software charge threshold of 0.3 p.e. to suppress dark noise. While effective for noise rejection, this threshold reduces the detection efficiency for single-photoelectron signals. As a result, the probability that PMT i registers at least one hit is reduced relative to the ideal Poisson expectation and is modeled as

$$P_{\text{hit},i} = 1 - v_i e^{-\mu_i}, \quad (4.7)$$

where v_i is an efficiency parameter that accounts for threshold-induced losses.

Hit Charge PDF

For PMTs that register a hit, the distribution of observed charge provides additional information about the event energy. The hit charge PDF for PMT i is modeled as a Gaussian distribution:

$$f_{i,j}(q_i) = \frac{1}{\sqrt{2\pi j\sigma^2}} \exp\left(-\frac{(q_i - j)^2}{2j\sigma^2}\right), \quad (4.8)$$

where q_i is the observed charge in photoelectron units, j is the assumed number of photoelectrons contributing to the signal, and σ is the single-photoelectron charge resolution. This approximation effectively captures the charge response for multi-photoelectron signals while remaining computationally efficient.

Hit Time PDF

PMT hit timing provides a powerful discriminator between scintillation photons originating from the physical event and accidental dark noise hits. The timing response of the detector is modeled using calibration data obtained from deployed radioactive sources.

The timing probability for PMT i is given by

$$P_{\text{time},i} = \frac{\psi(t_i) a_i E_{\text{vis}} + d_i}{\mu_i}, \quad (4.9)$$

where $\psi(t_i)$ is the normalized scintillation time profile evaluated at the PMT hit time t_i . This PDF is constructed as a weighted sum of the signal timing distribution and a constant dark noise contribution, ensuring proper normalization and robustness against accidental hits.

Energy Likelihood

The full energy likelihood function combines the probabilities for PMTs that did and did not register hits:

$$L = \prod_{\text{no hit PMTs}} P_{\text{no-hit},i} \prod_{\text{hit PMTs}} \left[P_{\text{hit},i} \left(\sum_{j=1}^{100} f_{i,j} \right) P_{\text{time},i} \right], \quad (4.10)$$

where the sum over j accounts for multi-photoelectron contributions up to $j = 100$. The reconstructed visible energy is defined as the value of E_{vis} that maximizes this likelihood. The maximization is performed using the Newton–Raphson method.

Energy reconstruction is carried out independently using the 17-inch and 20-inch PMT subsets. The final event energy is obtained as a weighted combination of the two estimates:

$$E_{\text{vis}} = (1 - \alpha)E_{\text{17inch}} + \alpha E_{\text{20inch}}, \quad (4.11)$$

with $\alpha = 0.3$, chosen to optimize overall energy resolution.

Bad Channels in Energy Reconstruction

The increasing number of low-gain PMTs over time has led to a gradual degradation of energy resolution when such channels are excluded entirely from reconstruction. In many cases, low-gain PMTs remain operational and detect scintillation photons, but their gain instability prevents reliable standard calibration. To recover useful information from these channels, a modified energy reconstruction approach was developed. The strategy proceeds as follows:

1. The change in gain alters the effect of the 0.3 p.e. threshold on hit probability.

To account for this, the no-hit probability is expanded as:

$$P'_{\text{no-hit},i} = \left(1 + \epsilon_1 \mu_i + \epsilon_2 \frac{\mu_i^2}{2!} + \epsilon_3 \frac{\mu_i^3}{3!} \right) e^{-\lambda \mu_i}. \quad (4.12)$$

This expression was initially motivated as a Taylor expansion of the standard no-hit probability but was subsequently modified phenomenologically to better reproduce observed data, resulting in the additional exponential suppression term.

2. The parameters ϵ_1 , ϵ_2 , ϵ_3 , and λ are determined using calibration data. Events satisfying the following selection criteria are used to estimate the no-hit probability as a function of expected charge:

- reconstructed radius $r < 6$ m,
- non-muon events and events occurring more than 2 ms after a muon,
- events with more than 120 hit 17-inch PMTs,
- PMT waveforms containing a single identified pulse.

Figure 4.6 shows an example fit of the adjusted no-hit probability model to low-gain PMT data. The fitting procedure is performed independently for each PMT and on a run-by-run basis.

3. The updated no-hit probability model is incorporated into the energy likelihood defined in Eq. 4.10, allowing low-gain PMTs to contribute statistically to energy reconstruction.

Incorporating information from low-gain PMTs improves the energy resolution by up to 3% [51]. Unless otherwise stated, all analyses presented in this work use energy reconstructed from the combined set of normal-gain and low-gain PMTs.

4.2.6 Muon Reconstruction

The identification and reconstruction of cosmic-ray muons and muon-correlated neutrons are essential for background rejection in KamLAND-Zen. Although KamLAND

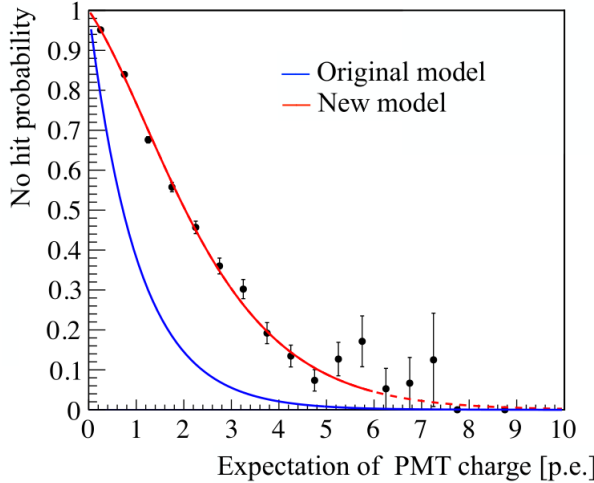


Figure 4.6: Fit of the no-hit probability as a function of expected charge μ for a low-gain PMT. The original model is shown in blue, while the modified model (red) provides improved agreement with data. Figure taken from Reference [47].

is located deep underground, a residual cosmic muon flux remains and produces a variety of backgrounds through spallation processes in the scintillator and surrounding materials. These processes generate radioactive isotopes and free neutrons that can mimic low-energy physics signals if not properly identified and vetoed. This section describes the selection criteria used to identify muon events, as well as the reconstruction techniques employed to determine muon trajectories through the detector. Accurate muon reconstruction enables effective application of spatial and temporal vetoes and provides the foundation for neutron tagging and spallation background suppression.

Muon Selection Criteria

Muon candidates are selected based on their large light output and/or coincident activity in the outer detector (OD). The selection criteria are defined as follows:

- Total collected charge from 17-inch PMTs, $Q_{17} \geq 10,000$ p.e.
- $Q_{17} \geq 500$ p.e. and the number of hit OD PMTs ≥ 9 .

The first criterion selects muons that traverse the liquid scintillator volumes of the detector and produce intense scintillation light. A total charge of 10,000 p.e. corresponds approximately to an event energy of 30 MeV, well above the energy range relevant for most low-energy KamLAND-Zen physics analyses.

The second criterion targets muons that pass primarily through the buffer oil or graze the detector (“clipping muons”). These muons do not produce scintillation light but generate Cherenkov radiation in the buffer oil and are efficiently tagged by the outer detector. In this case, a threshold of 500 p.e. corresponds to roughly 40 MeV of deposited energy in Cherenkov light.

Cosmic-Ray Muon Reconstruction

Unlike point-like energy depositions from radioactive decays, cosmic-ray muons traverse the detector along extended trajectories, producing elongated tracks of light. Muon reconstruction aims to estimate the entrance point, exit point, and direction of these tracks using PMT timing and charge information. A schematic overview of the reconstruction procedure is shown in Figure 4.7. The reconstruction proceeds through the following steps:

1. The inner detector PMT registering the earliest hit time is identified as a candidate for the muon entrance point. If the charge of this hit is anomalously low or temporally isolated from the bulk of the event activity, it is classified as a dark hit and excluded. A line is drawn from this earliest-hit PMT to the center of the KamLAND detector, and the intersection of this line with the outer balloon is defined as a temporary entrance point.
2. The PMT with the largest collected charge is then identified. This PMT is expected to register light later than the earliest-hit PMT and its neighboring channels, reflecting the muon’s progression through the detector. A line drawn

from this brightest-hit PMT to the detector center defines a temporary exit point at its intersection with the outer balloon.

3. A temporary muon track is constructed as the straight line connecting the temporary entrance and exit points. This track is subsequently refined by examining the correlation between the reconstructed track length and the total collected charge, which provides a consistency check on the assumed trajectory.
4. The quality of the reconstructed track is evaluated using several criteria:
 - whether both the earliest-hit and brightest-hit PMTs can be robustly identified,
 - whether the mean hit time of PMTs near the entrance point precedes that of PMTs near the exit point.

A reconstruction quality parameter, referred to as *badness*, is assigned based on these checks.

Approximately 15% of muon candidates are classified as poorly reconstructed according to the badness metric. These events are typically associated with complex topologies such as muon bundles, stopped muons, or waveform ringing effects in the PMTs. While poorly reconstructed muons are excluded from analyses requiring precise track geometry, they are still retained for muon–neutron correlation studies, where exact track information is less critical.

The average light yield produced by muons in the KamLAND detector has been studied in detail and is reported in Ref. [51]. The measured charge yield per unit track length is given by:

$$\langle dQ_C/dX \rangle = 28 \pm 5 \text{ p.e./cm} \quad (\text{Cherenkov muons}), \quad (4.13)$$

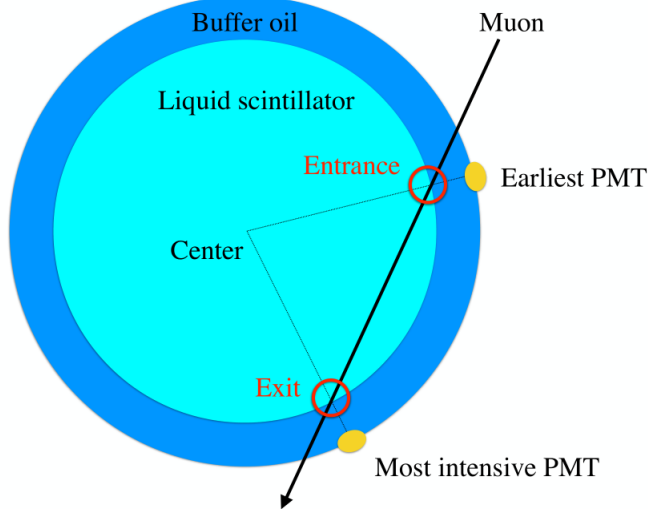


Figure 4.7: A schematic illustration of cosmic-ray muon reconstruction in the KamLAND detector, showing how the muon entrance and exit points are estimated using PMT information. Figure taken from Reference [47].

for muons producing predominantly Cherenkov radiation, and:

$$\langle dQ_S/dX \rangle = 338 \pm 12 \text{ p.e./cm} \quad (\text{scintillation muons}), \quad (4.14)$$

for muons traversing the liquid scintillator and producing scintillation light. The large difference between these values reflects the substantially higher light yield of scintillation relative to Cherenkov emission and provides a powerful handle for distinguishing muon topologies and validating reconstruction performance.

4.2.7 MoGURA Neutron Reconstruction

Neutrons produced by cosmic-ray muon spallation constitute an important class of correlated backgrounds in KamLAND-Zen. These neutrons are typically captured on protons, emitting a 2.2 MeV gamma ray with a characteristic delay of tens to hundreds of microseconds following the parent muon. Efficient identification of such neutron capture events is therefore essential for spallation background rejection.

Neutron capture signals are best recorded using the MoGURA data acquisition system, as the primary KamFEE-based front-end electronics (FBE) experience significant deadtime and waveform distortion immediately following high-energy muon events. Although MoGURA substantially improves post-muon sensitivity, PMT after-pulsing remains present and must be carefully rejected. To address this, an effective hit multiplicity parameter, denoted N_s , is introduced to statistically separate true neutron capture signals from after-pulse-induced fake hits. The neutron reconstruction procedure proceeds as follows:

1. A 200 ns-wide time window is opened in the MoGURA waveform data. Using the hit information contained within this window, a provisional event vertex is reconstructed with the LT vertex fitter.
2. Based on the reconstructed vertex, the time of flight (ToF) from the vertex to each PMT is calculated. The ToF-subtracted hit time residual distribution is then obtained.
3. The resulting residual time distribution contains contributions from both genuine scintillation light produced by the 2.2 MeV gamma ray following neutron capture and fake signals arising from PMT after-pulses. To quantify the signal significance, the number of hits inside a 30 ns-wide *on-time* window, N_{in} , and the number of hits in the remaining 170 ns *off-time* window, N_{out} , are counted. The effective number of signal hits is defined as

$$N_s = N_{\text{in}} - N_{\text{out}} \times \frac{30 \text{ ns}}{170 \text{ ns}}. \quad (4.15)$$

This subtraction statistically removes the contribution of uniformly distributed after-pulses from the on-time window.

4. The 30 ns on-time window is shifted in steps of 20 ns, corresponding to the

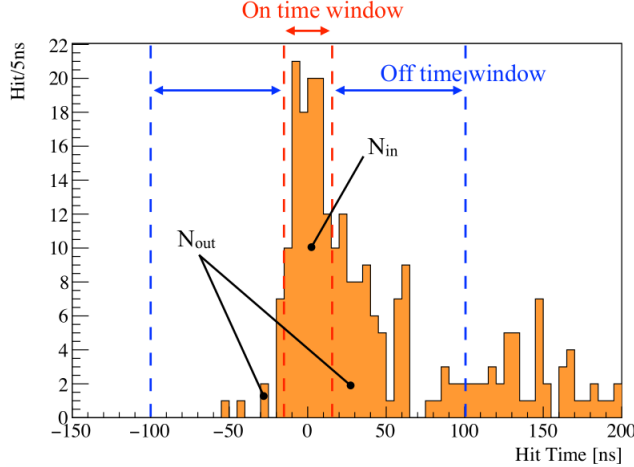


Figure 4.8: Time residual distribution for a neutron capture event recorded by MoGURA, illustrating contributions from genuine scintillation light and fake PMT after-pulses. The on-time and off-time windows used in the calculation of the effective hit multiplicity N_s are indicated. Figure taken from Reference [52].

MoGURA DAQ clock period, and the calculation of N_s is repeated for each shift.

5. The 200 ns reconstruction window is then shifted in time, and steps (1)–(4) are repeated. The combination of the 200 ns window and the 30 ns on-time window that maximizes N_s is identified. The vertex reconstructed using this optimal window configuration is taken as the final reconstructed neutron capture vertex.

Figure 4.8 displays a histogram of PMT hit times (horizontal axis, in nanoseconds) relative to a reconstructed event time, with the hit rate per 5 ns bin shown on the vertical axis. The distribution corresponds to a candidate neutron capture event recorded by the MoGURA data acquisition system.

4.2.8 Muon–Neutron Correlation

The neutron selection procedure described in the previous section contains a substantial contribution from accidental noise and PMT after-pulses. As a result, neutron

candidates identified by MoGURA are only used for background discrimination when they can be temporally associated with preceding cosmic-ray muons. In particular, MoGURA-based neutron tagging plays an important role in identifying xenon spallation products, which constitute a significant background for KamLAND-Zen analyses. To reliably associate neutron candidates with parent muon events, a dedicated muon–neutron correlation procedure is employed. This procedure accounts for the use of multiple data acquisition systems and the presence of gaps between KamLAND DAQ runs. The selection of muon–neutron pairs proceeds as follows:

1. The end Unix time of the previous KamLAND DAQ run and the start Unix time of the current run are checked to identify any gaps in KamFEE (FBE) data-taking.
2. MoGURA runs that acquired data during these gaps are collected. Muon events recorded by MoGURA are used to tag neutrons during KamFEE run gaps, while muon events recorded by KamFEE are used when KamFEE data are available.
3. A delayed coincidence analysis is performed to identify neutron candidates occurring shortly after muon events. Initial cuts are applied to remove obvious noise and after-pulse-dominated events by rejecting candidates with $dT > 2500\,\mu\text{s}$ or $N_s < 100$. The remaining events are then subjected to the detailed MoGURA neutron selection criteria described below.

The final neutron selection is illustrated in Figure 4·9, which shows the two-dimensional distribution of the effective hit multiplicity N_s versus the time delay dT between a neutron candidate and the preceding muon. Two key features are visible in this distribution. At very short dT , the event rate is elevated due to PMT after-pulses and electronic noise following muon events. In addition, neutron candidates with small N_s values are prevalent at short dT because baseline overshoot in the PMTs reduces

the apparent signal size. Based on these observations, the following selection criteria are applied to identify neutron capture events suitable for background rejection:

- $N_{\text{total}} = N_{\text{in}} + N_{\text{out}} > 150$ (minimum hit multiplicity requirement),
- $N_s > 50 \wedge 10 < dT < 1200 \mu\text{s}$ (rejection of after-pulses and accidental coincidences),
- Time-dependent N_s requirement to suppress after-pulses, where we accept an event if:

$$(10 < dT < 20 \mu\text{s} \Rightarrow N_s \geq dT + 70) \quad (4.16)$$

$$\wedge (20 < dT < 70 \mu\text{s} \Rightarrow N_s \geq -0.8dT + 106),$$

where the final condition removes regions of the N_s - dT parameter space dominated by residual noise and baseline recovery effects.

Figure 4.9 shows the dT distribution of MoGURA neutron candidates selected using the criteria above. The distribution is fit to an exponential decay between 500 and 1000 μs , corresponding to the expected neutron capture time on hydrogen. The fitted exponential is extrapolated to shorter and longer time delays to evaluate the selection efficiency. A visible suppression of events at short dT reflects the reduced neutron tagging efficiency immediately following muon events, where PMT after-pulsing and baseline overshoot degrade reconstruction performance. This inefficiency is taken into account when evaluating the overall neutron tagging efficiency used in background rejection.

4.3 Event Selection

Candidate $0\nu\beta\beta$ events must satisfy a series of event selection criteria designed to remove instrumental artifacts, unphysical events, and backgrounds that can mimic the

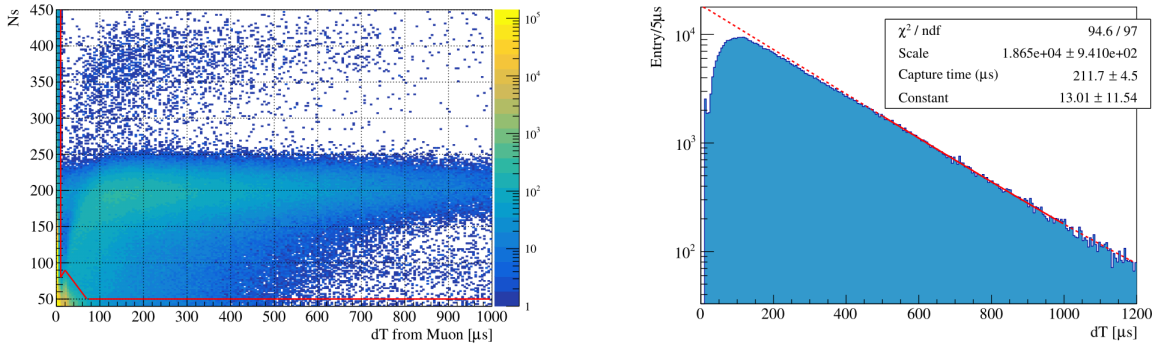


Figure 4.9: Muon–neutron correlation using MoGURA data. (Left) Two-dimensional distribution of effective hit multiplicity N_s versus time delay dT between neutron candidates and the preceding muon. Events above the red selection boundary are identified as MoGURA neutrons and used for background rejection. (Right) Time delay (dT) distribution of selected MoGURA neutrons, with an exponential fit performed between 500 and 1000 μs . Taken from Reference [52].

signal. These selections are divided into two broad categories: rejection of unphysical or poor-quality events, and removal of backgrounds arising from known physical processes. In this section, the event selections applied in this analysis are described in detail, followed by a discussion of the signal inefficiency introduced by these cuts.

4.3.1 Unphysical and Bad Quality Event Rejection

A significant fraction of events recorded by the KamLAND DAQ systems do not correspond to genuine physical energy depositions in the detector. In addition, some events arising from real physical processes are poorly reconstructed due to detector instabilities or electronic effects. This subsection describes the criteria used to identify and reject such unphysical and poor-quality events.

1. PMT flasher events

Photomultiplier tubes can occasionally emit light directly into the detector volume, producing so-called PMT flasher events. These events can arise from several mechanisms, including electrical discharge within the dynode structure or light emission from the epoxy surrounding the PMT base circuitry. Flasher

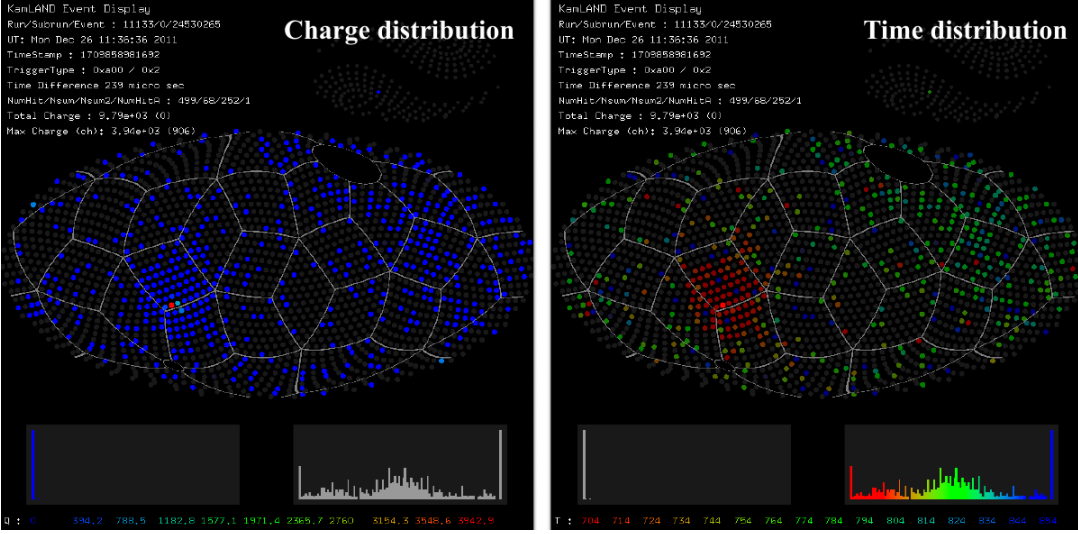


Figure 4.10: Event display of a PMT flasher event. The left panel shows the charge distribution, where one PMT exhibits an exceptionally large charge along with elevated charge in neighboring PMTs. The right panel shows the hit-time distribution, which is relatively flat since the light does not originate from scintillation. The hit times of the flasher PMT and its neighbors are characteristically early. Figures taken from Reference [52].

events exhibit a characteristic signature in which a single PMT records an exceptionally large charge, accompanied by elevated charge in nearby PMTs.

Figure 4.10 shows a typical flasher event display. The charge distribution is highly localized around the flashing PMT, while the timing distribution is relatively flat, reflecting the non-scintillation origin of the light. To reject these events, the following selection criteria are applied:

- Total charge of inner detector PMTs > 2500 p.e.,
- Maximum inner detector PMT charge divided by total inner detector charge $> 60\%$,
- Average charge of PMTs neighboring the brightest PMT > 20 p.e.

2. Post-muon events

Cosmic-ray muons deposit a large amount of energy in the detector, leading to temporary instabilities in the detector response. In particular, PMT after-pulsing and baseline overshoot result in a high rate of fake triggers and degrade the quality of event reconstruction immediately following a muon. To avoid contamination from these effects, all events occurring within 2 ms after a cosmic-ray muon are excluded from the excited-state analysis. Although these events are removed from the primary physics analysis, they are retained for specialized studies such as spallation background estimation.

3. Missing waveform events

High after-pulse rates following cosmic-ray muons can cause the ATWD digitizers to remain busy, preventing proper waveform acquisition. Events recorded under these conditions lack complete waveform information and are referred to as missing waveform events. In such cases, the number of hit 17-inch PMTs within 125 ns of the trigger, denoted `NsumMax`, is recorded even when waveforms are missing. For properly recorded events, `NsumMax` is proportional to the total number of hit 17-inch PMTs, `Nhit17`. Missing waveform events are therefore identified using the ratio between these two quantities. Figure 4.11 shows the distributions of `Nhit17` versus `NsumMax` for all physics events and for ^{214}Bi -tagged events. Events satisfying the following criteria are removed from the excited-state analysis:

- $\text{Nhit17} < \text{NsumMax} \times 0.99 - 25$,
- dT after a muon $< 2\text{ ms}$ if `NsumMax` < 1200 ,
- dT after a muon $< 2\text{ s}$ if `NsumMax` > 1200 .

The inefficiency introduced by this cut is evaluated using ^{214}Bi -tagged events and is found to be less than 0.01%.

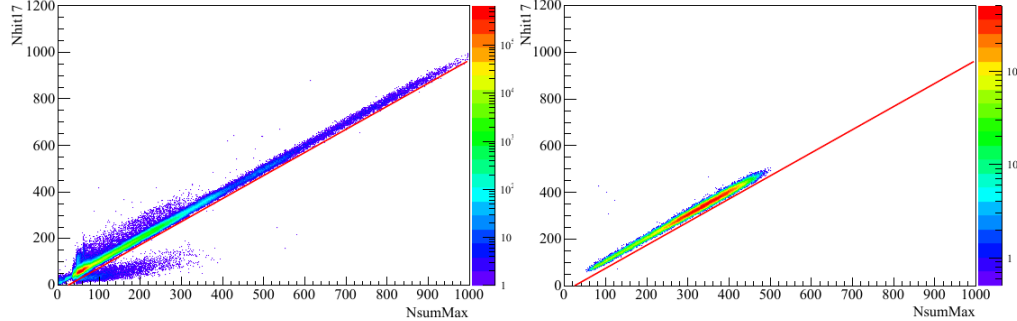


Figure 4.11: N_{hit17} versus N_{sumMax} distributions for all physics events (Left) and ^{214}Bi -tagged events (Right). The missing waveform cut removes events with incomplete waveform acquisition while introducing negligible inefficiency. Figure taken from Reference [52].

4. Post-PPS trigger events

A pulse-per-second (PPS) trigger is issued once per second for continuous monitoring of the detector and electronics stability. However, PPS triggers are known to induce elevated electronic noise and an increased DAQ trigger rate immediately afterward. To mitigate this effect, all events occurring within $100\ \mu\text{s}$ following a PPS trigger are excluded from the analysis.

5. Badly reconstructed events

The quality of an event's vertex reconstruction is quantified by the reconstruction quality parameter known as *Badness*. This parameter is calculated using nine observables that characterize deviations of the PMT hit timing and charge distributions from their expected behavior. Events with large Badness values are dominated by noise, pileup, or poorly reconstructed topologies. These events are removed using an energy-dependent Badness threshold defined as

$$\text{Badness} < 25.0 \times \exp(-4.5 \times E_{\text{vis}} [\text{MeV}]) + 3.1. \quad (4.17)$$

Figure 4.12 shows the Badness distributions for all physical events and for ^{214}Bi events identified using delayed coincidence tagging. The cut effectively removes

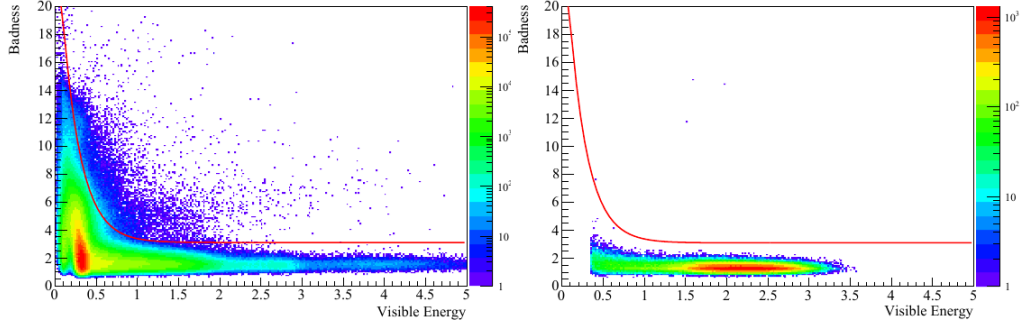


Figure 4.12: Badness distributions for all physics events (Left) and ^{214}Bi -tagged events (Right). Figure taken from Reference [52].

poorly reconstructed events while retaining high efficiency for genuine physical signals.

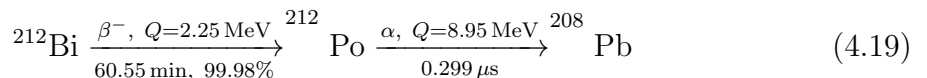
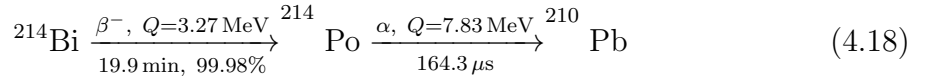
4.4 Background Rejection

4.4.1 Uranium/Thorium

The radioactive isotopes ^{214}Bi and ^{212}Bi are produced in the ^{238}U and ^{232}Th decay chains, respectively, and constitute some of the dominant internal backgrounds in KamLAND-Zen. These isotopes are introduced into the detector primarily through trace uranium and thorium contamination in the liquid scintillator, as well as radioactive impurities on the surface of the inner balloon. During the filling of the xenon-loaded liquid scintillator (XeLS), a small amount of ^{222}Rn was also introduced into the detector. Because ^{222}Rn has a relatively short half-life of 3.8 days, the radon-related ^{214}Bi background decayed away during the early stages of KamLAND-Zen 800 data-taking. This time dependence of the radon-induced background is explicitly modeled and accounted for in the physics analysis. Decays of ^{214}Bi and ^{212}Bi are tagged using two complementary techniques: a delayed-coincidence veto based on correlated Bi–Po decays, and a double-pulse fitting method that identifies pileup events in which the two decays occur within a single DAQ readout window.

Delayed Coincidence Veto

Both ^{214}Bi and ^{212}Bi β^- decays are followed by the rapid decay of short-lived polonium daughters, ^{214}Po and ^{212}Po , respectively:



Because the prompt β decay and delayed α decay are strongly correlated in both space and time, these events can be efficiently identified and vetoed using a delayed-coincidence analysis. The criteria applied in the KamLAND-Zen analysis are:

- delayed energy: $0.2 < E_d < 1.3$ MeV,
- distance between prompt and delayed vertices: $dR < 170$ cm,
- time delay between prompt and delayed events: $dT < 1.9$ ms.

Figure 4.13 shows the delayed-coincidence parameter distributions used in the ^{214}Bi selection. Coincident pairs with $dT < 10\text{ }\mu\text{s}$ are excluded from this selection and reserved for the ^{212}Bi analysis, reflecting the much shorter half-life of ^{212}Po . Two distinct peaks are observed in the delayed energy distribution. The lower-energy peak corresponds to polonium α decays in which a fraction of the energy is deposited in the inner balloon nylon film rather than in the liquid scintillator.

Figure 4.14 shows the delayed-coincidence parameter distributions used in the ^{212}Bi selection. For this selection, a tighter timing requirement of $dT < 10\text{ }\mu\text{s}$ is applied. The veto efficiency for $^{214}\text{Bi-Po}$ decays occurring in the XeLS is $99.89 \pm 0.03\%$, while the efficiency for decays occurring on the inner balloon film is $48.9 \pm 9\%$.

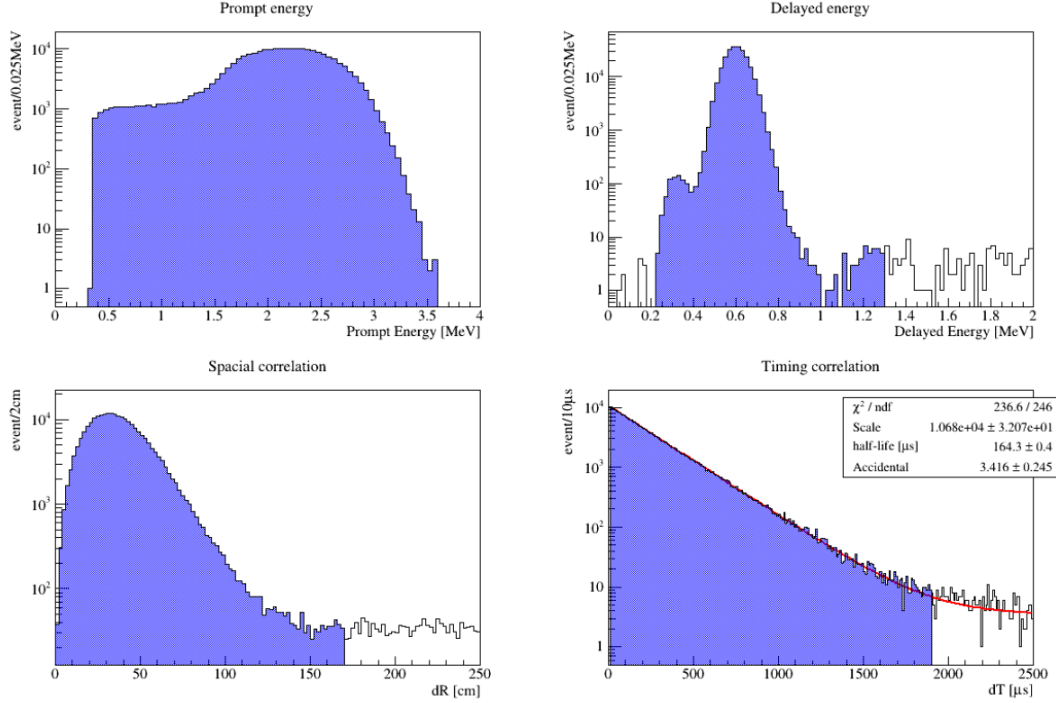


Figure 4.13: Delayed-coincidence selection parameter distributions for ^{214}Bi . The distributions of prompt energy, delayed energy, spatial separation, and delay time are shown. The blue shaded regions indicate tagged events. Events with $dT < 10 \mu\text{s}$ are excluded and reserved for $^{212}\text{Bi-Po}$ selection. Figures taken from Reference [52].

The reduced efficiency in the latter case arises because α particles deposit a significant fraction of their energy in the balloon film rather than in the scintillator. For ^{212}Po decays that occur with extremely short delay times, the events are instead identified using the double-pulse fitting technique described below.

Pileup Events

When the delay time dT between the prompt and delayed decays is sufficiently short, Bi–Po sequential decays may be recorded as a single event within the KamLAND DAQ readout window. In these cases, the delayed-coincidence selection of two separate events is ineffective. Such events are referred to as pileup events. Because pileup events contain the combined energy of the initial β decay and the subsequent α decay, their reconstructed visible energy can extend beyond the $0\nu\beta\beta$ region of interest,

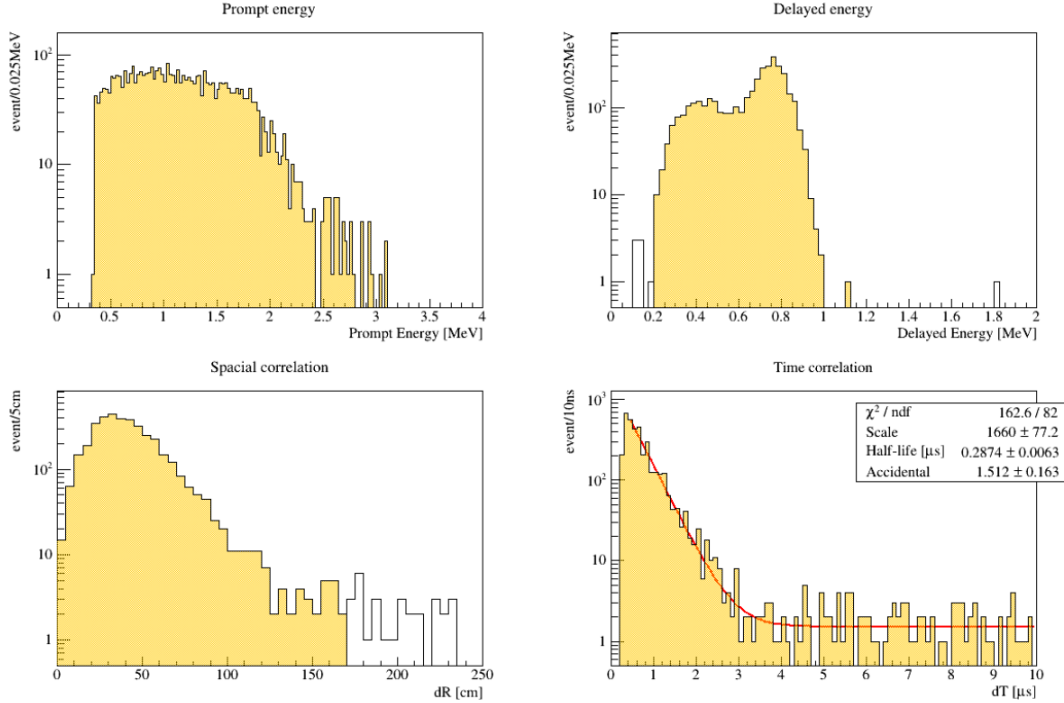


Figure 4.14: Delayed-coincidence selection parameter distributions for ^{212}Bi . The distributions of prompt energy, delayed energy, spatial separation, and delay time are shown. The yellow shaded regions indicate tagged events. Only events with $dT < 10 \mu\text{s}$ are used for this selection. Figures taken from Reference [52].

making them an important background to suppress. The energy spectrum of ^{212}Bi -Po pileup events is shown in Figure 4.14. To identify these events, a double-pulse fitting method has been developed that searches for hit-time distributions consistent with two distinct energy depositions. The procedure is as follows:

A double-pulse fitting method has been developed to identify pileup events in which two energy depositions occur within a single DAQ readout window. This method searches for events whose hit-time distributions exhibit signatures consistent with two temporally separated scintillation pulses. Specifically, the hit-time distribution of each candidate event is fitted using two reference waveforms according to the following procedure:

1. Construction of the reference time profile

A reference hit-time profile is constructed using $2\nu\beta\beta$ candidate events. These events are selected with $1.4 < E_{\text{vis}} < 1.6 \text{ MeV}$ and reconstructed radius less than 157 cm, after applying all $0\nu\beta\beta$ background vetoes. This reference waveform represents the characteristic timing response of a single energy deposition in the detector.

2. Construction of candidate event hit-time profiles

The hit-time profile of each candidate event is constructed using all recorded PMT hit times and associated charges. In standard reconstruction, only the first hit time per PMT is typically used. For the double-pulse fit, however, multi-hit information is retained to enhance sensitivity to multiple temporally separated pulses and to improve separation between prompt and delayed components.

3. Fitting of the hit-time profile

The candidate hit-time profile is fitted using two time-shifted reference waveforms corresponding to prompt and delayed energy depositions. The fit includes four free parameters: the prompt signal energy E_p , the prompt signal timing T_p , the delayed signal energy E_d , and the time separation between the two pulses ΔT . A maximum-likelihood optimization is performed by minimizing the following χ^2 function:

$$\chi^2 = \begin{cases} 2 \sum_i \left[-(x_i - f_i) + x_i \ln \left(\frac{x_i}{f_i} \right) \right], & (x_i > 0), \\ 2 \sum_i [-(x_i - f_i)], & (x_i = 0), \end{cases} \quad (5.27) \quad (4.20)$$

where i indexes the 1 ns-wide time bins, x_i denotes the observed number of PMT hits in the i th bin, and f_i is the expected number of hits in that bin. The

expected hit distribution is modeled as

$$f_i = |E_p| R(i - T_p) + |E_d| R(i - T_p - \Delta T) + D, \quad (4.21)$$

with $R(i)$ representing the reference waveform and D denoting the global PMT dark rate, estimated from off-time windows. The χ^2 minimization is performed using the MINUIT package within the ROOT analysis framework. For each tested pair of $(T_p, \Delta T)$ values, the parameters E_p and E_d are allowed to float, and the optimal set of four parameters is determined.

4. Correction of reconstructed energies

The fitted parameters E_p and E_d serve as relative scaling factors for the reference waveforms but do not provide accurate absolute energy estimates for the individual pulses. Instead, the total reconstructed visible energy E_{vis} , obtained using the standard energy reconstruction described in Section 4.2.5, is redistributed between the prompt and delayed components according to:

$$E_{p'} = E_{\text{vis}} \times \frac{E_p}{E_p + E_d} \quad E_{d'} = E_{\text{vis}} \times \frac{E_d}{E_p + E_d} \quad (4.22)$$

This procedure assigns the appropriate fraction of the total event energy to the prompt and delayed pulses based on the results of the double-pulse fit.

5. Pileup candidate selection

Finally, pileup events are identified based on their reconstructed time separation ΔT and delayed energy component $E_{d'}$. The selection criteria are optimized using Monte Carlo simulations while limiting the inefficiency for $0\nu\beta\beta$ events to approximately 0.1%. Figure 4.15 shows the selection regions overlaid on Monte Carlo distributions. The fraction of $^{212}\text{Bi}-\text{Po}$ events surviving the pileup rejection is estimated to be $2.3 \pm 0.5\%$.

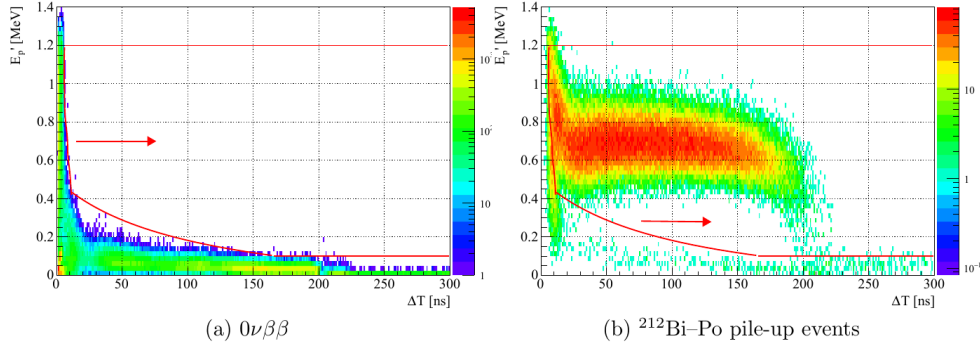


Figure 4.15: Selection criteria in the $(E_{d'}, \Delta T)$ plane used to identify pileup events. The distributions are shown for Monte Carlo $0\nu\beta\beta$ events (Left) and $^{212}\text{Bi}-\text{Po}$ events (Right). Events within the red boundaries are rejected as pileup. Figure taken from [52].

4.4.2 Antineutrinos

The original physics objective of the KamLAND experiment was the detection of electron antineutrinos produced by nuclear reactors, as well as antineutrinos from geo-physical and astrophysical sources. In both KamLAND and KamLAND-Zen, electron antineutrinos are detected via the inverse beta decay (IBD) reaction:

$$\bar{\nu}_e + p \rightarrow e^+ + n. \quad (4.23)$$

In an IBD interaction, the prompt signal is produced by the positron, which deposits its kinetic energy in the liquid scintillator and subsequently annihilates with an electron, emitting two 511 keV γ rays. The neutron undergoes thermalization through elastic scattering and is eventually captured on a proton, emitting a 2.2 MeV γ ray with an average capture time of $\tau = 207 \mu\text{s}$. This characteristic two-stage signature provides a powerful handle for identifying IBD events using a delayed-coincidence technique.

In the original KamLAND antineutrino analyses, IBD events were selected using a likelihood-based approach. In KamLAND-Zen, however, a simpler and robust box-

cut selection is sufficient due to the relatively low antineutrino rate and the distinct delayed-coincidence signature. The IBD selection criteria applied in this analysis are:

- delayed energy: $E_d > 1.5 \text{ MeV}$,
- distance between prompt and delayed vertices: $dR < 200 \text{ cm}$,
- time delay between prompt and delayed events: $dT < 1.0 \text{ ms}$.

Following the 2011 Tohoku earthquake and subsequent shutdown of Japanese nuclear power plants, the reactor antineutrino flux at the Kamioka site was significantly reduced. As a result, the rate of IBD events within a fiducial radius of $r < 550 \text{ cm}$ is less than 0.2 events per day. The efficiency of the IBD box-cut selection is 99.14%, and the residual antineutrino background in KamLAND-Zen analyses is therefore negligible.

4.4.3 Short-lived Spallation Products

High-energy cosmic-ray muons traversing the detector can induce spallation reactions in the liquid scintillator and surrounding materials, fragmenting nuclei into lighter radioactive isotopes and producing secondary particles such as neutrons. Several of these spallation products, particularly those originating from ^{12}C , constitute dominant backgrounds in the $2\nu\beta\beta^*$ and $0\nu\beta\beta$ analyses. Multiple tagging and veto techniques have therefore been developed to identify and suppress these short-lived spallation backgrounds.

^{12}B Veto

The β^- decay of ^{12}B is a significant contributor to the background in the $0\nu\beta\beta$ region of interest. In KamLAND, the cosmic-ray muon rate is approximately 3 Hz, leading to frequent production of ^{12}B through muon-induced spallation of ^{12}C . The half-life

of ^{12}B is 20.2 ms, allowing for efficient suppression through a simple post-muon veto. In this analysis, all events occurring within 150 ms following a muon are vetoed. This window corresponds to approximately five lifetimes of ^{12}B and effectively removes the vast majority of these decays. The associated loss of livetime is treated as detector deadtime and is accounted for in the exposure calculation.

MoGURA Neutron Veto

Muon-induced spallation reactions frequently produce neutrons in addition to radioactive isotopes. These neutrons are strongly correlated in time and space with the parent muon and with subsequent spallation products. The MoGURA DAQ system is used to identify neutron capture events occurring shortly after cosmic-ray muons, enabling an additional veto of short-lived spallation backgrounds. In particular, correlations with MoGURA-tagged neutrons are used to identify decays of isotopes such as ^{10}C , ^6He , and ^8Li . Candidate events are vetoed if they satisfy the following criteria:

- distance between the candidate decay and the spallation neutron: $dR < 160 \text{ cm}$,
- time delay between the candidate decay and the spallation neutron: $dT < 180 \text{ s}$,

where the timing window corresponds to approximately five lifetimes of ^{10}C , the longest-lived isotope among the targeted short-lived spallation products.

^{137}Xe Veto

Neutrons produced by muon spallation can also be captured on ^{136}Xe nuclei in the xenon-loaded liquid scintillator, producing ^{137}Xe . The subsequent β^- decay of ^{137}Xe has a Q -value of 4.2 MeV and a half-life of 3.82 minutes, making it a potentially dangerous background in the $0\nu\beta\beta$ region of interest. The ^{137}Xe background is suppressed using a triple-coincidence tagging method involving the parent muon, the

neutron capture on ^{136}Xe , and the delayed β decay. Candidate events are vetoed according to the following selection criteria:

- distance between the candidate decay and the spallation neutron: $dR < 160\text{ cm}$,
- time delay between the candidate decay and the spallation neutron: $dT < 1620\text{ s}$.

Because neutron capture on ^{136}Xe releases a cascade of γ rays with a total energy of approximately 4 MeV—significantly higher than the 2.2 MeV γ emitted in neutron capture on protons—the neutron selection criteria are adjusted accordingly. Neutron candidates associated with ^{137}Xe production are required to have an effective hit multiplicity $N_s > 240$ to ensure robust identification of xenon capture events. A schematic illustration of the spallation veto strategy for carbon- and xenon-based isotopes is shown in Figure 4-16.

4.4.4 Shower Veto

As a cosmic-ray muon traverses the detector, its energy loss along the track is not uniform. Instead, localized regions of enhanced energy deposition—commonly referred to as electromagnetic or hadronic “showers”—occur where the muon interacts more strongly with detector material. These shower regions are associated with increased production of spallation isotopes, and subsequent radioactive decays are spatially correlated with the location of maximal energy loss along the muon track. The shower veto exploits this correlation by identifying regions of large energy deposition along reconstructed muon tracks and rejecting candidate events that occur near these locations.

$$\text{PDF}(dE/dX, dL)$$

The energy deposition per unit length along the muon track, dE/dX , and the distance dL between the muon track and a candidate decay event are correlated for spallation products. To quantify this correlation, a two-dimensional probability density function (PDF), $\text{PDF}(dE/dX, dL)$, is constructed using muon data according to the following procedure:

1. Cosmic-ray muons are selected and their trajectories are reconstructed using the muon reconstruction algorithm described in Section 4.2.6.
2. The time at which the muon enters the inner detector, denoted T_0 , is calculated from the reconstructed muon track and PMT timing information.
3. For each detected photon, the distance L from the muon entrance point to the

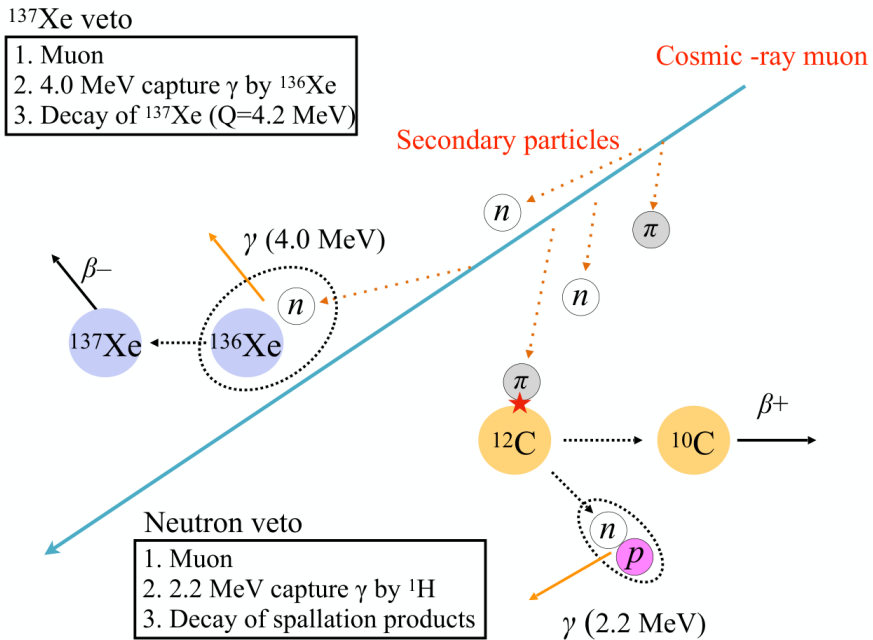


Figure 4·16: Schematic illustration of the spallation veto strategy using MoGURA-tagged neutrons for carbon- and xenon-based spallation products. Figure taken from Reference [52].

photon production point along the muon track is calculated. Figure 4.17 illustrates the geometry of photon production along a muon track. The calculation is based on the relations:

$$x_2^2 = r^2 + s_1^2 - 2s_1r \cos \theta, \quad (4.24)$$

$$s_1 + nx_2 = c(t - T_0), \quad (4.25)$$

where r is the distance from the detector center to the PMT, θ is the angle between the muon track and the PMT direction, n is the refractive index of the liquid scintillator, t is the PMT hit time, and c is the speed of light in vacuum. Solving these equations yields s_1 , which corresponds to the longitudinal distance L along the muon track. In standard event reconstruction, only the first photon arrival time at each PMT is used. For the shower veto, however, all photon hits recorded by each PMT are utilized in a so-called multiTQ analysis. This approach improves sensitivity to localized energy deposition by allowing L to be calculated for multiple photons per PMT.

^{12}B decays are used to construct and validate the PDF($dE/dX, dL$), as ^{12}B can be efficiently tagged using the short time-delay selection following muon events. Figure 4.18 shows an example of a reconstructed dE/dX distribution along a muon track, where a localized region of enhanced energy deposition is clearly visible. An accidental background likelihood is also constructed using off-time events that are uncorrelated with muon activity. Spallation background candidates are rejected by computing the logarithmic likelihood ratio between the spallation hypothesis and the accidental hypothesis. Events with a spallation-to-accidental log-likelihood ratio less than -1.8 are classified as spallation-induced backgrounds and are rejected from the analysis.

4.4.5 Xenon Spallation Products

Spallation products of xenon constitute an important background in searches for both $0\nu\beta\beta$ and $2\nu\beta\beta^*$ decays. In particular, these backgrounds obscure the endpoint region of the $2\nu\beta\beta$ spectrum and can populate the $0\nu\beta\beta$ region of interest. Suppressing xenon spallation backgrounds is therefore critical for both double-beta decay analyses. Unlike carbon spallation products, xenon spallation isotopes are generally heavier and can have half-lives of several hours or longer. As a result, simple time-based vetoes and the MoGURA neutron veto—effective for short-lived spallation products—are largely ineffective for these long-lived backgrounds.

To address this challenge, a dedicated likelihood-based selection has been developed to identify and statistically separate long-lived xenon spallation products from accidental background events. This method exploits correlations between candidate events and post-muon neutron activity, as well as their temporal and spatial proximity to the parent muon.

Muon-induced spallation of ^{136}Xe is typically accompanied by the emission of

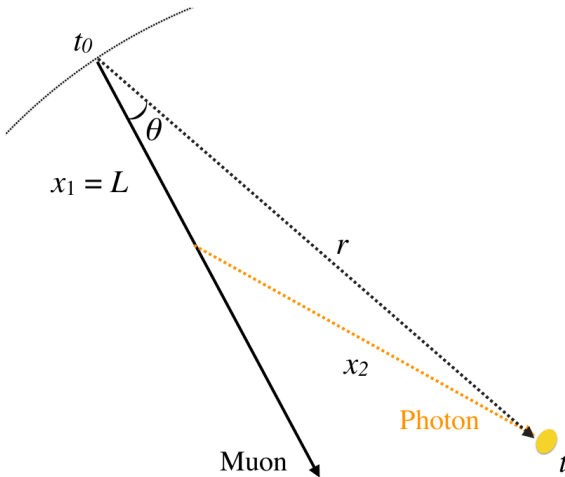


Figure 4.17: Schematic illustration of photon production along a cosmic-ray muon track and the geometry used for dE/dX reconstruction. Figure taken from Reference [52].

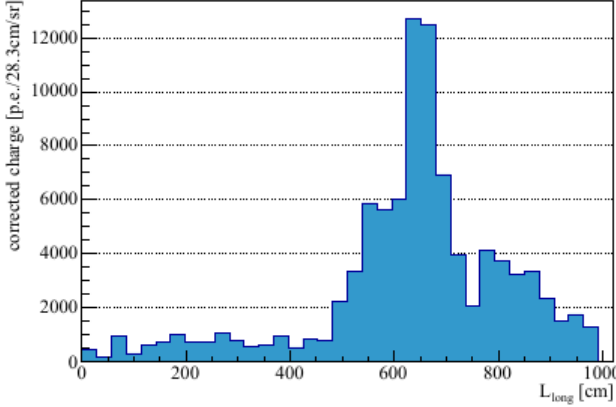


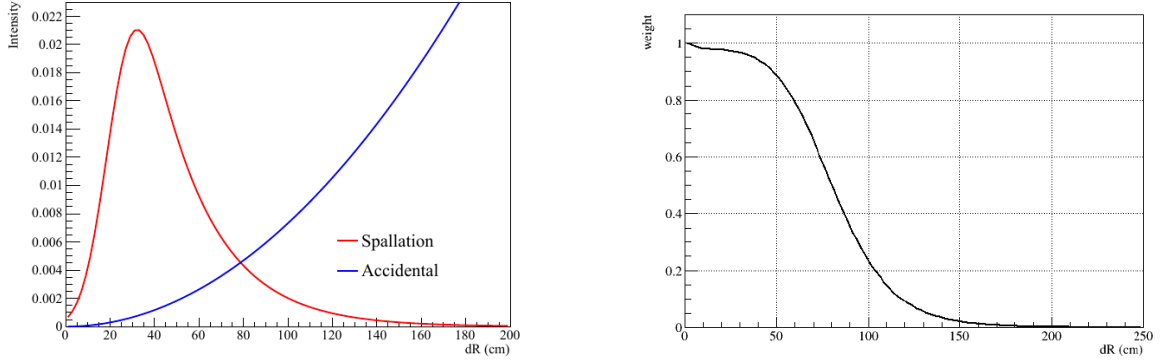
Figure 4.18: Example of a reconstructed dE/dX distribution along a muon track. The region of maximum energy deposition is observed at $L_{\text{long}} \approx 600$ cm. Figure taken from Reference [47].

multiple free neutrons. These neutrons are captured in the detector following the muon and provide a powerful handle for identifying xenon spallation events. However, the neutron sample also contains a significant contribution from accidental neutron-like signals and detector noise. To quantify the likelihood that observed neutrons are associated with a given candidate event, the Effective Number of Neutrons (ENN) variable is introduced. Each neutron detected after a muon is assigned a weight based on its spatial correlation with the candidate event. The ENN is defined as the sum of these weights over all neutrons following a given muon:

$$ENN = \sum_{\text{neutrons}} \frac{PDF_{\text{spl.}}(dR)}{PDF_{\text{spl.}}(dR) + PDF_{\text{acc.}}(dR)}, \quad (4.26)$$

where dR is the spatial distance between the candidate event and a neutron capture event. Spallation products and neutrons originating from the same muon are expected to be spatially correlated, while accidental neutrons are approximately uniformly distributed in space.

The probability density function $PDF_{\text{spl.}}(dR)$ describing spallation-correlated neu-



(a) Spatial separation dR for spallation-correlated and accidental neutrons

(b) Long-lived candidate events

Figure 4.19: Spatial distributions and weighting functions used in the ENN calculation. Figures taken from Reference [47].

trons is modeled using an exponentially modified Gaussian distribution, while the accidental neutron distribution $PDF_{acc.}(dR)$ is modeled as a quadratic function under the assumption of spatial uniformity. The spallation PDF is given by:

$$f(x; \mu, \sigma, \lambda) = \frac{\lambda}{2} \exp\left[\frac{\lambda}{2}(\mu + \lambda\sigma^2 - 2x)\right] \operatorname{erfc}\left(\frac{\mu + \lambda\sigma^2 - x}{\sqrt{2}\sigma}\right), \quad (4.27)$$

where $\operatorname{erfc}(x) = 1 - \operatorname{erf}(x)$ is the complementary error function. The free parameters (μ, σ, λ) are determined using ^{10}C spallation data. The sum in Equation 4.26 is performed over all neutron candidates within a fixed time window following each muon, and the resulting ENN value is assigned to that muon. Figure 4.19 shows the dR distributions and the resulting weighting function used in the ENN calculation.

Long-Lived Spallation Likelihood

Long-lived spallation backgrounds are not removed via a hard veto. Instead, candidate events are separated into a long-lived spallation dataset (LD) and a singles dataset (SD), which are simultaneously fit in the final spectral analysis. This sepa-

ration is achieved using a likelihood ratio defined to be:

$$R_L = \frac{L_{\text{spl.}}}{L_{\text{acc.}} + L_{\text{spl.}}}, \quad (4.28)$$

where $L_{\text{spl.}}$ and $L_{\text{acc.}}$ are the likelihoods for spallation and accidental hypotheses, respectively. The spallation likelihood is constructed as:

$$L_{\text{spl.}}(dR_{\text{near}}, ENN, dT) = \sum_{\text{spallation isotopes}} PDF(dT) \times PDF(dR_{\text{near}}, ENN), \quad (4.29)$$

where the sum runs over all spallation isotopes listed in Table 5.3. An implicit assumption is made that the time-dependent component $PDF(dT)$ is independent of the joint spatial–neutron distribution $PDF(dR_{\text{near}}, ENN)$. The accidental likelihood is assumed to be uniform in time and is defined to be:

$$L_{\text{acc.}}(dR, ENN, dT) = PDF(dR, ENN). \quad (4.30)$$

The likelihood PDFs are constructed using a combination of FLUKA simulations and real muon data from KamLAND-Zen. Spallation PDFs are informed by FLUKA simulations of isotope production and neutron emission, while accidental PDFs are derived from off-time data following muon events. Figure 4·20 shows the resulting two-dimensional likelihood profiles. To avoid numerical instabilities arising from bins with zero likelihood, bin smoothing is applied to both PDFs to ensure nonzero support across the full parameter space.

Figure 4·21 shows the distributions of log-likelihood ratios obtained from toy Monte Carlo studies, in which 10^6 events are generated for each PDF. The log-likelihood ratio is defined as:

$$\log_{10} \left(1 - \frac{L_{\text{acc.}}}{L_{\text{acc.}} + L_{\text{spl.}}} \right). \quad (4.31)$$

With this definition, smaller values correspond to a higher probability of being a long-lived spallation event, while larger values indicate accidental-like events.

Figure of Merit

The optimal threshold on the likelihood ratio is determined using a Figure of Merit (FOM) defined as:

$$\text{FOM} = \frac{S(t)}{\sqrt{S(t) + B(t)}}, \quad (4.32)$$

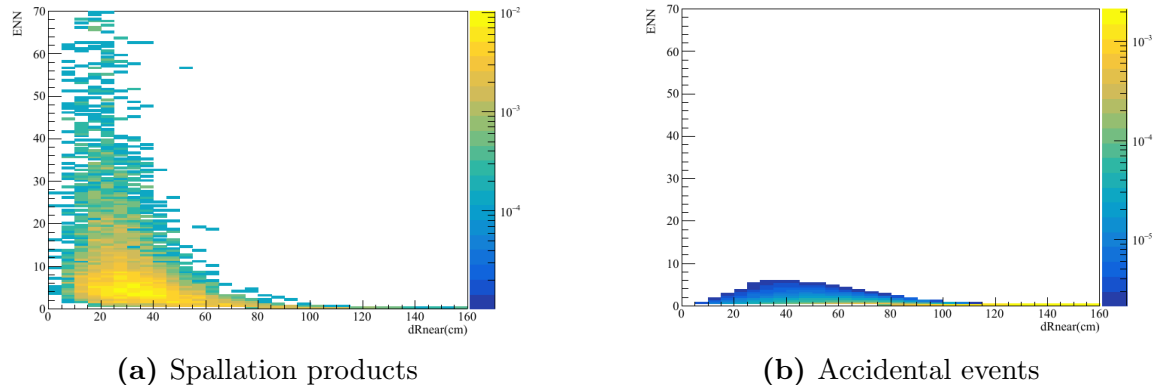


Figure 4.20: Two-dimensional likelihood PDFs in (dR, ENN) space for spallation and accidental hypotheses. Figure taken from Reference [47].

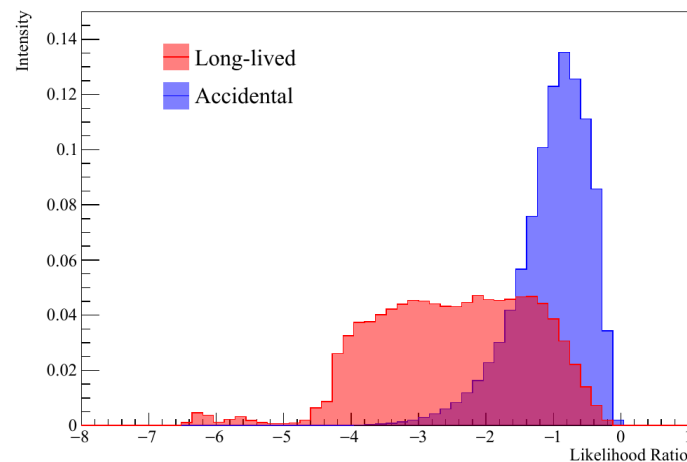


Figure 4.21: Log-likelihood ratio distributions generated using toy Monte Carlo simulations, demonstrating clear separation between spallation and accidental hypotheses. Figure taken from Reference [47].

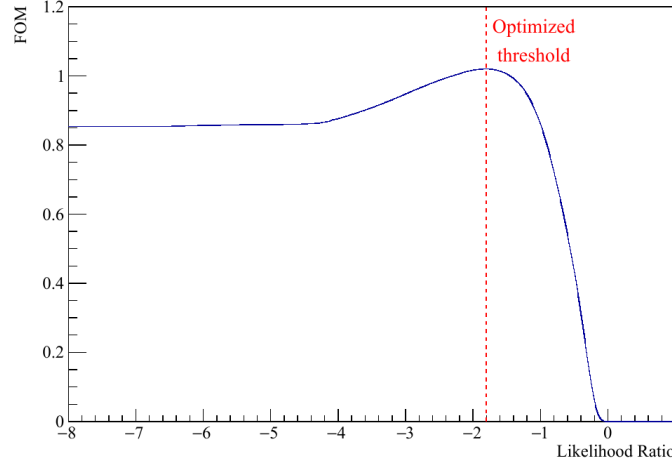


Figure 4.22: Figure of Merit used to determine the optimal likelihood ratio threshold for long-lived spallation background separation. Figure taken from Reference [47].

where $S(t)$ and $B(t)$ are the integrated signal and background distributions above a threshold t . Due to variations in detector conditions, including MoGURA livetime and neutron-tagging efficiency, the dataset is divided into three time periods, and the likelihood threshold is optimized independently for each period.

Veto Efficiency

The veto efficiency for long-lived spallation backgrounds is estimated for each isotope using toy Monte Carlo simulations informed by FLUKA. Simulated isotope production and neutron correlations are convolved with the measured KamLAND-Zen energy and vertex resolution before applying the likelihood selection.

Additional background rejection is provided by other vetoes, including the pileup veto and the MoGURA neutron veto. Their contributions are summarized below:

- **Pileup veto:** The double-pulse fitting method is sensitive to ortho-positronium decays from β^+ -emitting isotopes. Using production rates and lifetimes from Ref. [53], the average rejection efficiency is estimated to be 4.01%.
- **MoGURA neutron veto:** Long-lived spallation isotopes that decay within

the MoGURA neutron veto window are rejected. FLUKA and GEANT4 simulations indicate an average efficiency of 6.6%.

Uncertainties

Table 4.1 summarizes the estimated systematic uncertainties associated with the FLUKA simulation of long-lived spallation isotope production. The dominant contribution arises from uncertainties in the spallation modeling itself.

4.4.6 Signal Inefficiency

The cumulative effect of all background rejection vetoes on the $0\nu\beta\beta$ signal must be quantified in order to correctly determine the effective exposure of the analysis. This effect is expressed as the signal inefficiency, which is evaluated through the calculation of the analysis livetime.

The livetime is determined by applying the full set of event selection criteria to toy Monte Carlo (MC) events that are uniformly distributed in time and space throughout the detector volume. For vetoes that depend on correlations with real detector activity—such as muon–neutron pairs, delayed-coincidence selections, pulse-per-second (PPS) triggers, and missing waveform events—real detector data are used to model the corresponding deadtime. The livetime is defined as the fraction of the total runtime that remains after all event selection cuts are applied:

Source	Uncertainty
Time-bin dependence	2.9%
Neutron detection efficiency	2.73%
FLUKA vs. beam data comparison	7.5%
MoGURA energy resolution	5.67%

Table 4.1: Systematic uncertainties associated with FLUKA-based simulations of long-lived spallation backgrounds. Values taken from Reference [47].

Event selection	Deadtime ratio [%]
Spallation veto	14.64
MoGURA neutron veto	4.91
${}^8\text{Xe}$ veto	1.33
Shower veto	7.37
${}^{12}\text{B}$ veto	3.11
Xe spallation veto	8.56
Detector deadtime veto (post-PPS, post-muon, missing waveforms)	9.47
Hardware-related deadtime	0.0078
Delayed-coincidence radon veto	0.0013
Delayed-coincidence reactor veto	0.0010
Total	29.52

Table 4.2: Summary of deadtime contributions from background rejection vetoes. Values taken from Reference [47].

$$\text{Livetime} = \frac{(\text{Number of toy MC events surviving all selections})}{(\text{Number of generated toy MC events})} \times (\text{Runtime}) \quad (4.33)$$

The $2\nu\beta\beta^*$ spectral fit is performed simultaneously on long-lived spallation-enriched and spallation-depleted event samples. For proper relative normalization between these two datasets, the livetime is calculated independently for each sample. The resulting deadtime contributions from individual vetoes are summarized in Table 4.2.

The signal inefficiencies associated with the double-pulse fitting method and the vertex Badness selection are not included in Table 4.2. This omission reflects the fact that the toy MC livetime study is not performed at the individual PMT hit level, which is required to model these effects accurately. As demonstrated in Sections 4.4.1 and 4.3.1, the signal inefficiency introduced by these selections is negligible and does not significantly impact the overall exposure.

Chapter 5

Detector Calibration and MC Tuning

Accurate modeling of physics events and detector response is essential for the correct interpretation of KamLAND-Zen experimental data. This chapter describes the detector calibration strategy and Monte Carlo (MC) tuning procedures used in this analysis. Since the commissioning of KamLAND-Zen 800, no deployed laser or radioactive calibration sources have been used. This decision was made to minimize the risk of introducing radioactive contamination into the detector through source deployment systems. As a result, naturally occurring and cosmogenic backgrounds provide the primary tools for detector calibration and performance monitoring.

5.1 Detector Calibration

The KamLAND detector has been in operation for over two decades, during which its energy scale, nonlinearity, resolution, vertex reconstruction bias, and spatial resolution have been extensively calibrated and studied. Nevertheless, long-term variations in detector performance must be continuously monitored. Changes in detector conditions—including photomultiplier tube (PMT) gain adjustments, high-voltage (HV) reductions, channel failures, and maintenance activities—can affect energy and vertex reconstruction if left uncorrected. This section focuses on monitoring and correcting time-dependent variations in detector performance using intrinsic calibration sources available during normal physics data-taking.

5.1.1 Variation of Energy Scale Over Time

As PMT channels are lost, degrade, or undergo gain adjustments, the detector energy scale can vary over time. Over the analysis period spanning from 2019 to the end of KamLAND-Zen 800 data-taking in 2024, the overall energy scale exhibited variations at the level of approximately 3%. These variations are corrected using calibration handles that are continuously available throughout data-taking. Figure 5·1 shows the time dependence of the reconstructed energy scale using ^{40}K decays originating from detector materials. After correction, residual run-to-run fluctuations are constrained to within approximately 1%.

^{40}K PEEK Gammas

Reconstruction of the ^{40}K γ -ray peak originating from the polyether ether ketone (PEEK) material used in the balloon support structure provides a stable reference for monitoring the energy scale over time. The PEEK material is located approximately 550 cm above the detector center and contains trace amounts of naturally occurring

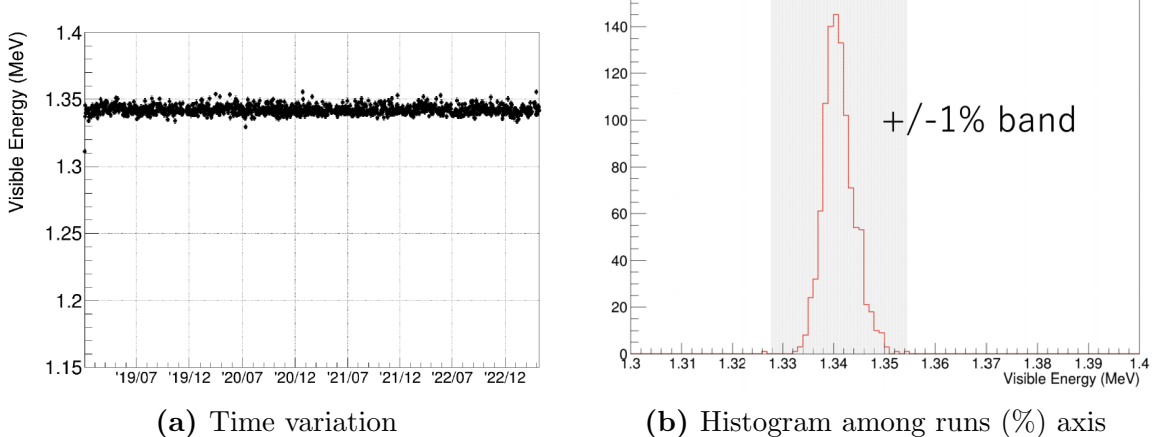


Figure 5·1: Time variation of ^{40}K peak after correction. (Left) Time variation of energy scale is corrected using ^{40}K and this figure is a check using ^{40}K itself. (Right) Fluctuations among runs are within 1% (gray band). Figure taken from Reference [47].

^{40}K , making it a persistent and well-localized calibration source. The electron-capture decay of ^{40}K to ^{40}Ar has a Q -value of $Q_{\text{EC}} = 1504 \text{ keV}$. Due to position-dependent light collection and optical attenuation, this peak is observed at a lower visible energy, around $E_{\text{vis}} \approx 1.35 \text{ MeV}$, at the PEEK location in KamLAND-Zen. The ^{40}K PEEK events are selected using the following criteria:

- pass the flasher veto,
- pass the muon veto,
- pass a 2 ms veto following muons,
- satisfy a cylindrical fiducial selection around the PEEK material ($450 < z < 600 \text{ cm}$, $\rho < 250 \text{ cm}$).

The stability of the reconstructed ^{40}K peak provides a sensitive probe of time-dependent variations in detector response.

Neutron Capture Gammas

The absolute energy scale of KamLAND is primarily anchored using the 2.2 MeV γ ray emitted following neutron capture on hydrogen. Figure 5.2 shows the time variation of the reconstructed neutron capture energy in both the xenon-loaded liquid scintillator (XeLS) and the surrounding KamLAND liquid scintillator (KamLS). Neutron capture events are selected in a time window following cosmic-ray muons. Due to detector instabilities immediately after muon events—such as elevated after-pulsing rates, PMT ringing, and baseline shifts—the earliest post-muon period is excluded. An on–off time subtraction method is used to remove accidental backgrounds and isolate the neutron capture signal.

- On-time window: $400 < dT < 1500 \mu\text{s}$,

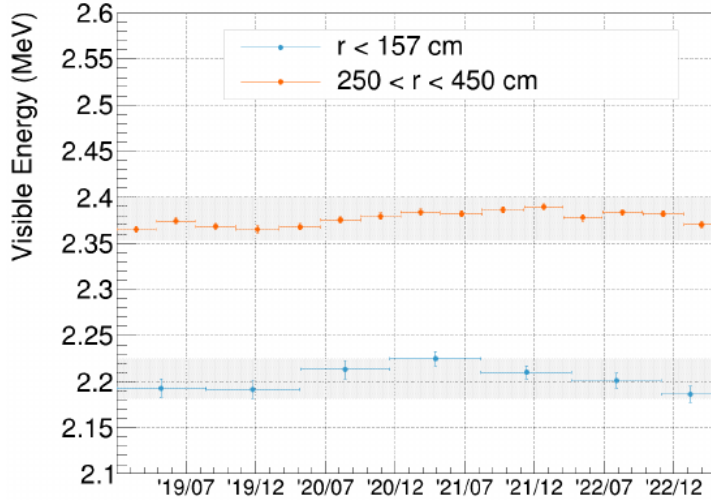


Figure 5.2: Neutron capture energy over KLZ-800 data-taking. The blue and orange points correspond to XeLS and KamLS respectively. Gray bands show $\pm 1\%$ deviation from the average. Note that the energy scale is 7% higher in KamLS due to the higher scintillator light-yield. Figure taken from Reference [47].

- Off-time window: $2800 < dT < 4000 \mu\text{s}$.

The reconstructed neutron capture peak is observed to be stable within $\pm 1\%$ throughout the data-taking period. The energy scale in KamLS is approximately 7% higher than in XeLS due to the higher intrinsic scintillation light yield in the absence of xenon loading.

$2\nu\beta\beta$ Rate

The high-statistics tail of the $2\nu\beta\beta$ decay spectrum provides an additional, independent check of the energy scale stability over time. In the absence of xenon leakage from the inner balloon, the event rate in a fixed energy window is sensitive to shifts in the reconstructed energy scale. All standard $0\nu\beta\beta$ analysis selections are applied, followed by an additional energy requirement of $1.85 < E_{\text{vis}} < 2.35 \text{ MeV}$ to isolate a region dominated by $2\nu\beta\beta$ decays. Figure 5.3 shows that the event rate in this region exhibits only minor statistical fluctuations and no significant long-term trend.

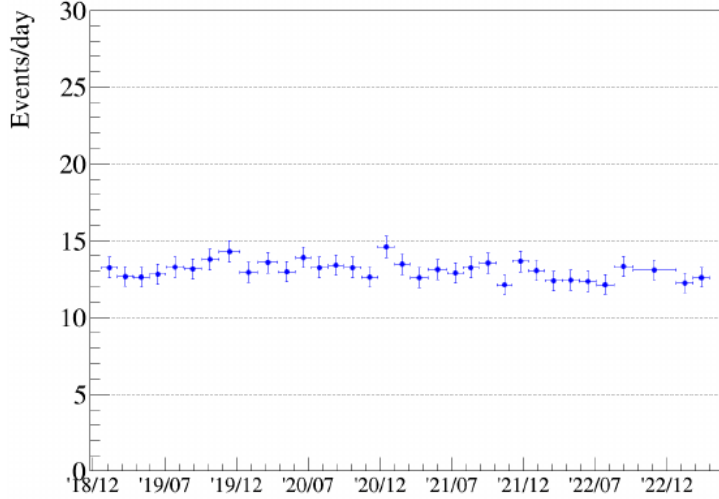


Figure 5.3: The event rate in the $2\nu\beta\beta$ dominant energy region over KLZ-800 data-taking. Figure taken from Reference [47].

5.1.2 MoGURA Stability

Cosmic-ray muon-induced spallation reactions provide a continuous and well-understood source of calibration signals in KamLAND-Zen. The MoGURA data acquisition system, with its dead-time-free readout, is capable of recording neutron capture events occurring much closer in time to the parent muon than is possible with the KamFEE DAQ. This enhanced tagging efficiency results in a larger and cleaner neutron sample, which can be exploited to monitor detector and DAQ stability over time.

The stability of MoGURA performance is characterized primarily by the neutron capture rate and the associated reconstructed energy and timing distributions. Figure 5.4 shows the time evolution of the neutron capture rate and the neutron tagging efficiency throughout the KamLAND-Zen 800 data-taking period. The neutron reconstruction and selection procedure employed by MoGURA is described in detail in Section 4.2.7.

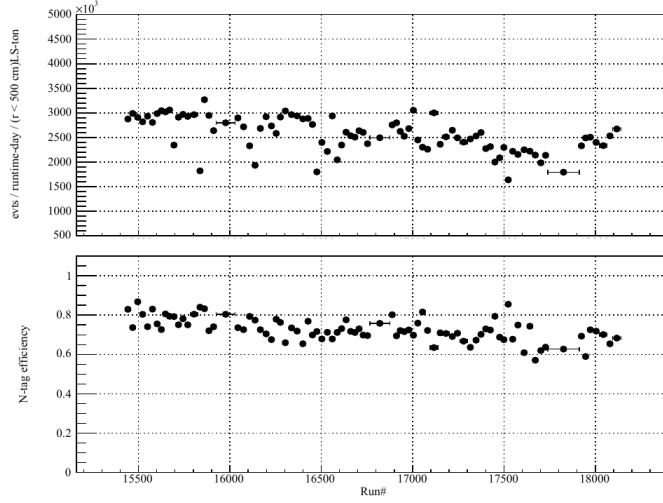


Figure 5.4: Time evolution of the neutron capture rate and neutron tagging efficiency measured by MoGURA over KamLAND-Zen 800 data-taking. Figure taken from Reference [47].

^{10}C Tagging Stability

The cosmogenic isotope ^{10}C provides an additional, well-characterized probe of detector and reconstruction stability. Due to its relatively short half-life and distinctive production mechanism, ^{10}C can be efficiently tagged using a triple-coincidence method involving the parent muon, an associated spallation neutron, and the subsequent β^+ decay. The ^{10}C tagging procedure used in the $0\nu\beta\beta$ background rejection is described in Section 4.4.3. For the purpose of stability monitoring, the ^{10}C selection is modified relative to the $0\nu\beta\beta$ analysis to obtain a higher-purity sample at the expense of overall efficiency. The selection criteria applied in this study are:

- events reconstructed in the KamLS volume ($250 < r < 400$ cm), with an additional veto of the corrugated tube region ($r > 250$ cm \wedge $z > 0$),
- visible energy in the range $2.0 < E_{\text{vis}} < 5.0$ MeV,
- on-time window: $10 < dT < 90$ s,
- off-time window: $300 < dT < 1000$ s.

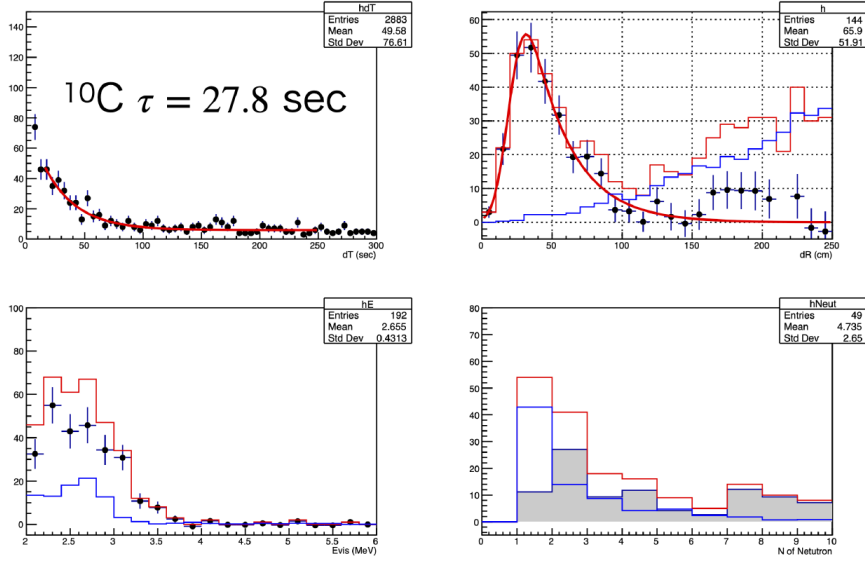


Figure 5.5: Characteristic distributions of ^{10}C decay candidates. Red and blue histograms correspond to on-time and off-time events, respectively. The black markers (or gray histograms) show the background-subtracted distributions (on-time minus off-time). Figure taken from Reference [47].

The lower bound of the on-time window is chosen to exclude contributions from ^6He , which has a half-life of 1.16 s and a β -decay Q -value of 3.5 MeV. The off-time window provides a measure of the accidental background, which is subtracted from the on-time sample. Figure 5.5 shows the characteristic distributions used to identify the ^{10}C sample. The decay rate is extracted by fitting an exponential function plus a constant background to the dT distribution. The spatial correlation between ^{10}C candidates and the nearest neutron capture, quantified by the distance dR , is modeled using an exponentially modified Gaussian (*exGaussian*) function. The time evolution of the fitted ^{10}C decay rate and the mean of the exGaussian dR distribution are shown in Figure 5.6. The absence of significant long-term trends demonstrates the stability of MoGURA neutron tagging and associated reconstruction performance over the full KamLAND-Zen 800 data-taking period.

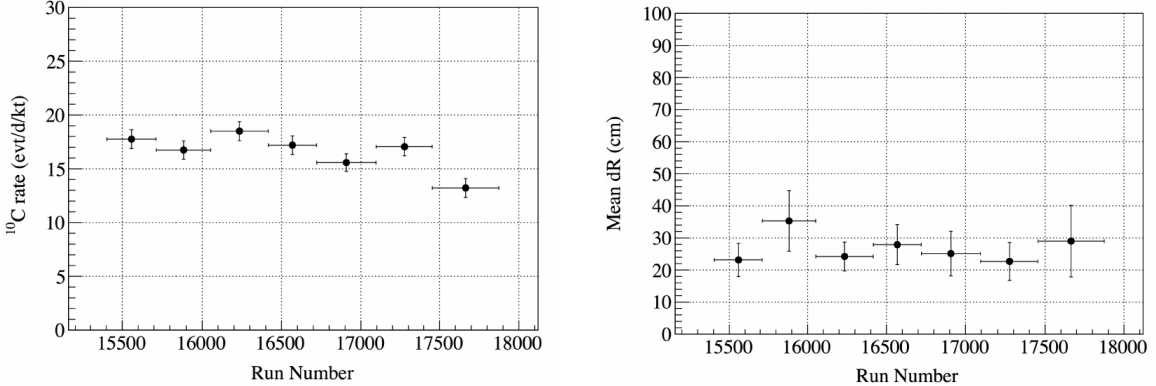


Figure 5.6: Time evolution of the ^{10}C decay rate (Left) and the shape of the dR distribution (Right) over KamLAND-Zen 800 data-taking. Figure taken from Reference [47].

5.2 MC Tuning

The KamLAND physics simulation framework is built on two complementary simulation tools: GEANT4 and FLUKA. GEANT4 is used to simulate radioactive signal and background decays, particle propagation, energy deposition, and scintillation light production and transport within the KamLAND detector [54]. The KamLAND-specific GEANT4-based simulation chain is referred to as `KLG4Sim`. The FLUKA simulation package is used to model cosmic-ray muon-induced spallation processes, including neutron multiplicity, neutron topology, and spallation isotope production [55, 56, 57, 58]. These simulations provide essential inputs for modeling cosmogenic backgrounds and for constructing spallation likelihoods used in background rejection.

5.2.1 Geant4 (KLG4)

The `KLG4Sim` parameters used in this analysis were tuned in prior KamLAND-Zen studies, most notably in References [45] and [52]. This section summarizes the calibration data and procedures used in those works to tune the detector response model. No additional tuning was performed specifically for this thesis.

KamLS Tuning

The properties of KamLAND liquid scintillator (KamLS), which constitutes the outer scintillator volume without dissolved xenon, were tuned using radioactive source calibration data acquired on January 16, 2018. During this calibration campaign, a composite radioactive source was deployed along the detector z -axis from -550 cm to $+550\text{ cm}$ in 50 cm increments, with approximately 20 minutes of data-taking at each position. The deployed source, designated Kam-41, consisted of a combination of ^{137}Cs , ^{68}Ge , and ^{60}Co isotopes. The composition and activity of the source at the time of data-taking are summarized in Table 5.1.

Figure 5.7 shows the distributions of the number of hit PMTs (N_{hit}) and total collected charge for the composite source. Distinct γ -ray peaks corresponding to the source isotopes are clearly visible. These peaks are used to constrain the energy scale nonlinearity in KamLS. The same figure also shows the tuned `KLG4Sim` spectra, which reproduce the data well after tuning.

The spatial dependence of the detector response was also studied using the deployed source data. These measurements were used to tune optical properties of the detector, including attenuation length, scattering probability, re-emission probability, and other light-transport parameters. Figure 5.8 shows the position dependence of

Construction date	Aug. 24, 2015		
DAQ date	Jan. 16, 2018		
Source ID	Kam-41 (composite source)		
	^{137}Cs	^{68}Ge	^{60}Co
Particle	1γ	2γ	2γ
Energy (keV)	661.7	511.0	1173.2, 1332.5
Initial intensity (Bq)	181	419	322
Estimated intensity (Bq)	180	356	234

Table 5.1: Summary of the radioactive calibration sources. Estimated intensities correspond to January 17, 2018, the date of the calibration DAQ.

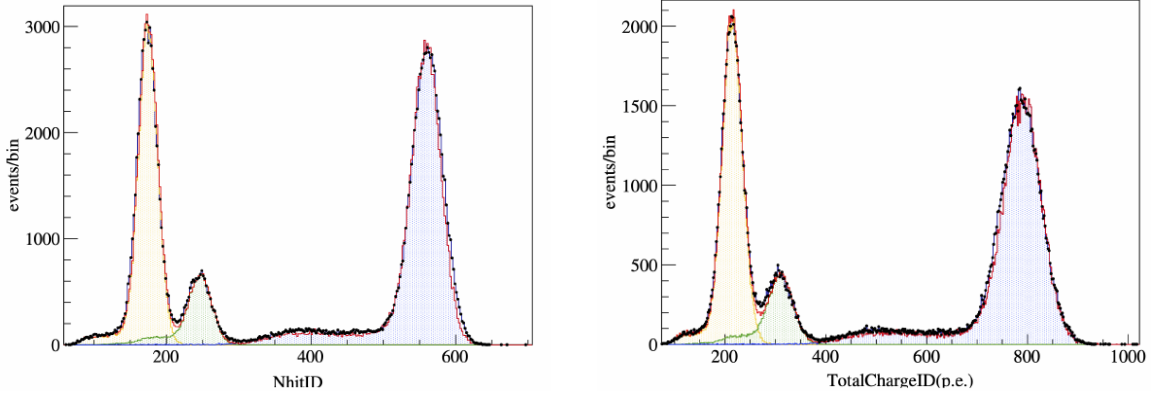


Figure 5.7: N_{hit} and total charge distributions from source calibration data. Black points show data, while colored histograms (orange: ^{137}Cs , green: ^{68}Ge , blue: ^{60}Co) show MC simulations. The tuned MC reproduces the data well in both observables. Figures from Reference [45].

the total charge peak for each source isotope. While deviations between data and simulation increase toward the edge of the detector, the agreement within the central region is within 2%. The physics analyses presented in this thesis are restricted to events with reconstructed radius $r < 250$ cm, where the simulation reproducibility is well controlled.

XeLS Tuning

No deployed radioactive calibration sources are available within the xenon-loaded liquid scintillator (XeLS). Instead, naturally occurring backgrounds are used to calibrate the detector response in this volume. During xenon handling and recirculation operations, ^{222}Rn can be introduced into XeLS through emanation from pipelines or buffer tanks. The subsequent $^{214}\text{Bi-Po}$ decay sequence can be efficiently tagged using delayed-coincidence techniques and occurs exclusively within XeLS. Because ^{222}Rn has a half-life of 3.8 days, this calibration handle is available only during the first several months following xenon handling operations. The high-statistics $^{214}\text{Bi-Po}$ sample collected during this radon-rich period is used to tune XeLS-specific detector param-

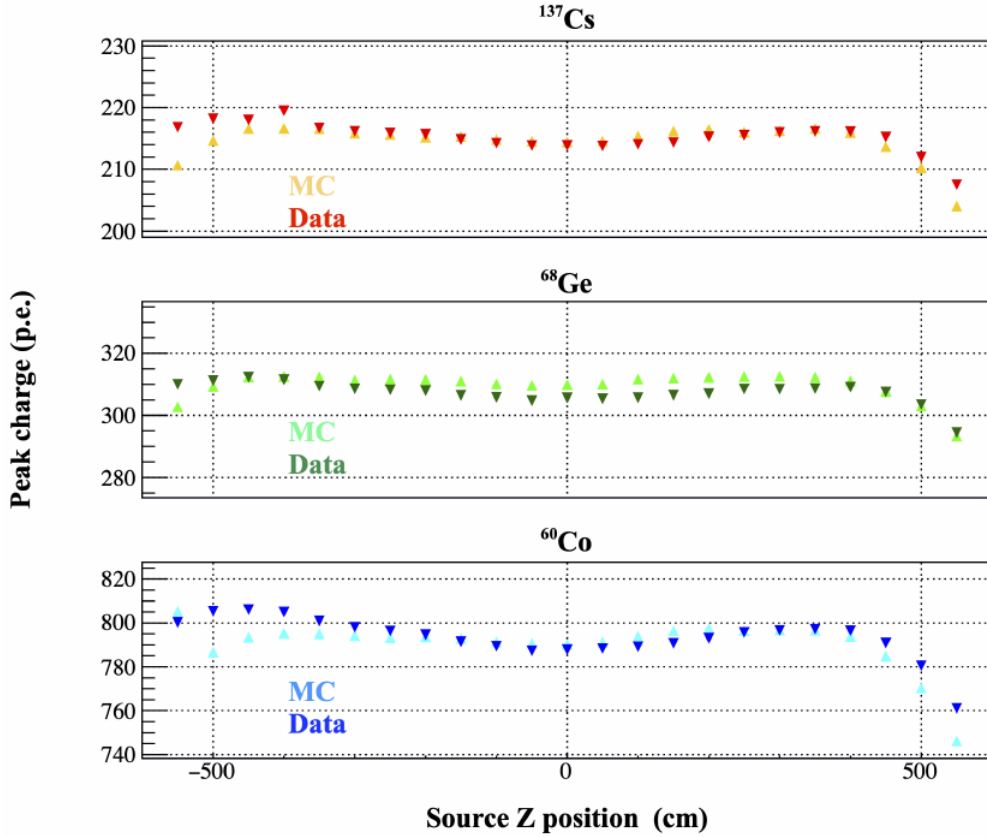


Figure 5.8: Position dependence of the total charge peak for each calibration source isotope. Figure from Reference [45].

eters, including Birks' constant, optical attenuation length, scattering probability, scintillator time profile, and re-emission probability.

Position-dependent Energy Correction

A position dependence of the reconstructed visible energy in XeLS is observed as a function of radius and polar angle. This effect is studied using the α decay peak of ^{214}Po . Figure 5.9 shows the radius dependence of the total collected charge for data and simulation. The observed deviations from the detector center are reproduced by KLG4Sim. Additional correction factors are applied to the simulation to ensure that the reconstructed $0\nu\beta\beta$ decay peak in XeLS does not exhibit residual position

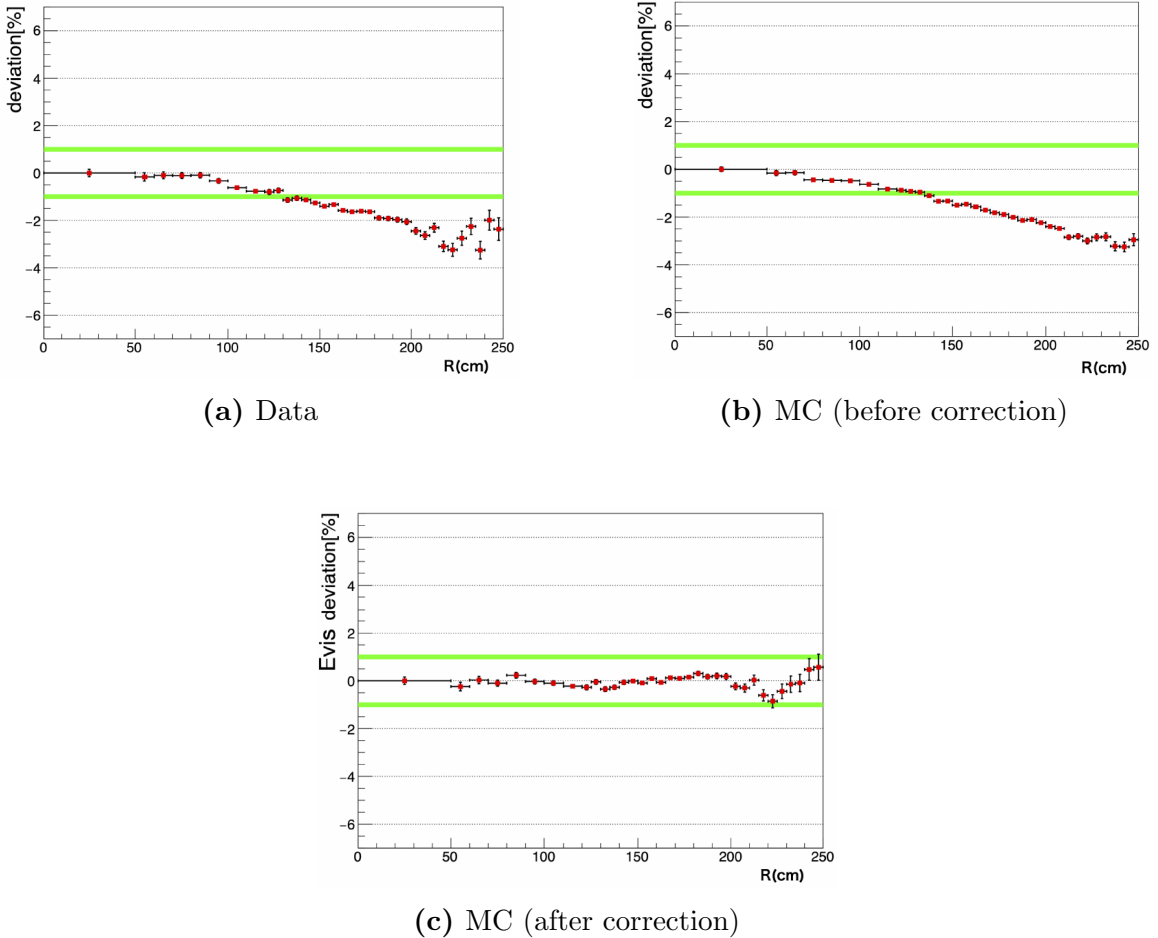


Figure 5.9: Radius dependence of the total collected charge for ^{214}Po α decays. Figures from Reference [45].

dependence. Figure 5.9 illustrates the agreement between data and simulation before and after applying these corrections.

Energy Non-Linearity

The relationship between visible energy and deposited energy in liquid scintillator is nonlinear due to scintillation quenching and the contribution of Cherenkov radiation. This behavior is described by Birks' law:

$$\frac{dL}{dx} \propto \frac{dE/dx}{1 + k_B \cdot (dE/dx)}, \quad (5.1)$$

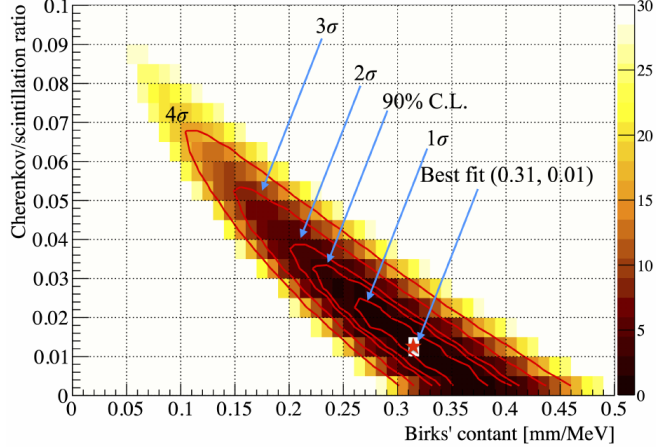


Figure 5.10: $\Delta\chi^2$ scan over Birks' constant k_B and the Cherenkov-to-scintillation ratio R . Figure taken from Reference [47].

where dL/dx is the light yield per unit path length, dE/dx is the energy loss per unit length, and k_B is Birks' constant, which depends on the scintillator composition. Charged particles also produce Cherenkov radiation; the fraction of total light yield attributed to Cherenkov light is parameterized by the Cherenkov-to-scintillation ratio R . Tagged ^{214}Bi decays in XeLS, primarily from the early radon-rich period, are used to tune k_B and R . This tuning procedure was performed in References [45, 52]. Figure 5.10 shows a $\Delta\chi^2$ scan over (k_B, R) , with a best-fit value of $(k_B, R) = (0.31, 0.01)$. These values are used for all signal and background simulations in this analysis. Figure 5.11 shows the result of the XeLS tuning, demonstrating good agreement between data and simulation for both the ^{214}Bi β energy spectrum and the spatial correlation of delayed-coincidence Bi–Po decays.

Energy Scale

The absolute energy scale in both KamLS and XeLS is calibrated using the 2.2 MeV γ ray emitted following neutron capture on hydrogen. This calibration is identical to that used for monitoring the time dependence of the energy scale. Due to additional quenching introduced by dissolved xenon, the light yield in XeLS is slightly reduced

relative to KamLS. Figure 5.2 shows the reconstructed neutron capture peaks used to anchor the absolute energy scale in both scintillator volumes.

5.2.2 FLUKA

The FLUKA simulation package is used to model cosmic-ray muon–induced spallation processes in KamLAND-Zen, including the production of radioactive isotopes and secondary neutrons. The FLUKA version used in this analysis is `FLUKA 2011.08.patch`. Details of the simulation setup and results for xenon spallation are presented in Reference [59], while earlier studies and measurements performed in KamLAND liquid scintillator (KamLS) are described in Reference [60].

Simulation Configuration

The physics models enabled in the FLUKA spallation simulation are listed in Table 5.2. FLUKA is used exclusively to simulate the initial muon interactions, including spallation isotope production and neutron generation. Radioactive decays of the produced isotopes, as well as neutron thermalization and capture γ emission, are disabled in FLUKA and instead handled by the GEANT4 simulation framework described in the previous section.

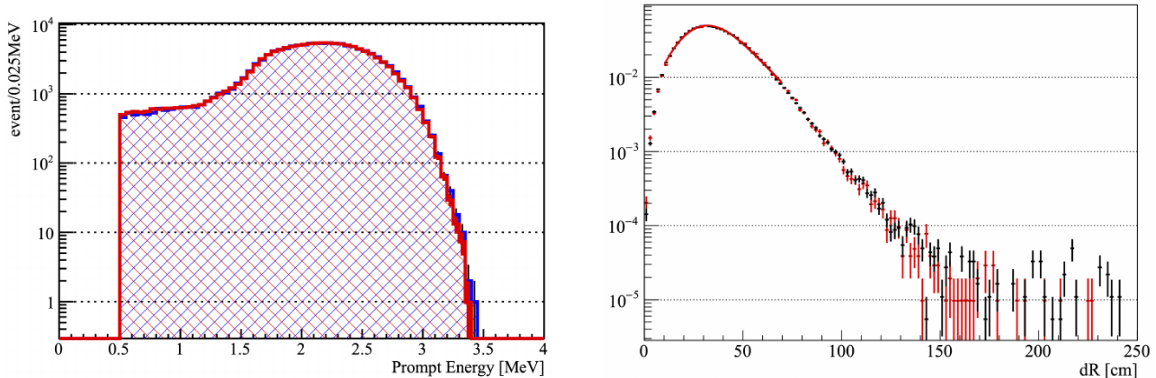


Figure 5.11: Tuned ^{214}Bi β -decay energy spectrum and spatial correlation of delayed-coincidence Bi–Po decays. Figures from Reference [52].

Cosmic-ray muon spallation is simulated by injecting muons into a cylindrical XeLS volume with a radius of 10 m and a height of 40 m. This volume significantly exceeds the physical size of the KamLAND-Zen inner balloon (radius ~ 2 m) in order to avoid boundary effects. Events occurring within 10 m of the cylindrical side walls or within 5 m of the exit surfaces are excluded from the analysis. The cosmic-ray muon energy and angular distributions are generated using the MUSIC package [61], which incorporates a detailed geometric description of the Kamioka mine. The resulting muon energy spectrum is passed to FLUKA as input. The mean simulated muon energy is 260 ± 1 GeV, consistent with expectations for the Kamioka overburden. The simulation reproduces a neutron capture time of $\tau = 207.0 \pm 0.3$ μ s, in agreement with the measured value in KamLAND. The muon charge ratio is fixed to $\mu^+/\mu^- = 1.3$, following Reference [62].

Card	Physics description	Status
DEFAULTS	A set of physics models	PRECISIO(n)
PHOTONNUC(lear)	Gamma interactions with nuclei	Activated
MUPHOTON	Muon photonuclear interaction	Activated
PHYSICS	Emission of light fragments	Activated by COALESCE(nse)
PHYSICS	Emission of heavy fragments	Activated by EVAPORAT(ion)
PHYSICS	Ion electromagnetic dissociation	Activated by EM-DISSO(ciation)
PHYSICS	Decay and isomer production	Activated by RAD-DECAY

Table 5.2: FLUKA physics processes enabled in the spallation simulation. From Reference [59].

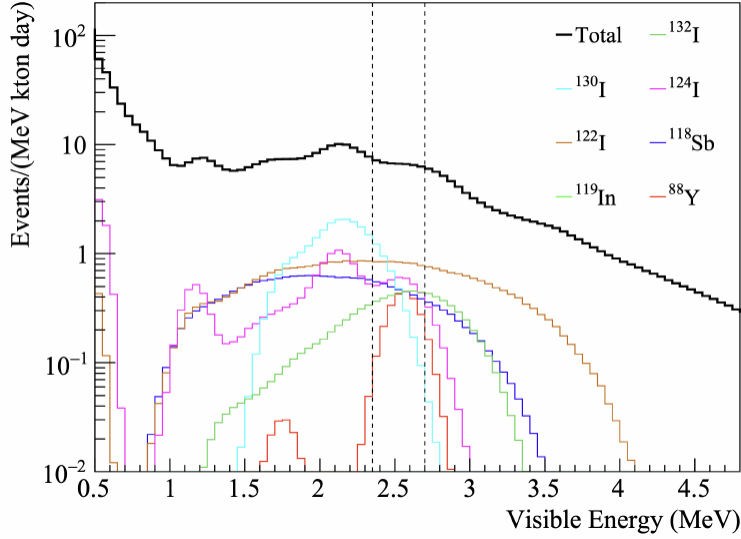


Figure 5.12: Simulated energy spectra of ^{136}Xe spallation products including their decay chain. Figure from Reference [47].

Radioactive Decays

As described above, FLUKA provides only the production locations and yields of spallation isotopes and neutrons. The subsequent radioactive decays and neutron capture γ rays are simulated using the `RadioactiveDecay` package in GEANT4. The GEANT4 version used is `Geant4.10.6.p01`, together with the evaluated nuclear structure data library `G4ENSDFSTATE2.2` [63]. Table 5.3 lists the xenon spallation products included in this analysis. Isotopes with production rates exceeding $0.01 \text{ (day}\cdot\text{kton})^{-1}$ in the Region of Interest (ROI) are selected, resulting in a total of 32 isotopes. The simulated visible energy spectra of these spallation products, including their full decay chains, are shown in Figure 5.12.

Tuning With ^{10}C

While FLUKA accurately models spallation production and neutron yields, it does not include detector effects such as vertex reconstruction uncertainty or neutron detection efficiency. In particular, FLUKA outputs the true neutron capture positions rather

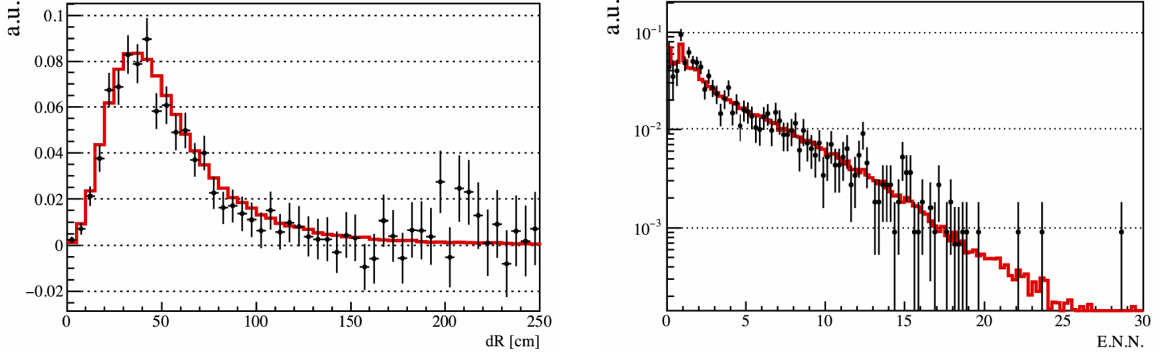


Figure 5.13: Comparison of tuned FLUKA simulations (red curves) and data (black points) for the ^{10}C dR (Left) and ENN (Right) distributions. Figures from Ref. [47].

than reconstructed vertices. To account for reconstruction effects, the true neutron capture positions from FLUKA are convolved with a Gaussian spatial resolution function. In addition, the neutron detection efficiency is modeled empirically as a function of muon charge:

$$\epsilon(\log_{10} Q_\mu) = \epsilon \left(1 - \frac{1}{1 + e^{-\sigma(\log_{10} Q_\mu - a)}} + b \right), \quad (5.2)$$

where Q_μ is the total muon charge. This parameterization reflects the fact that neutron detection efficiency is strongly affected by baseline fluctuations immediately following a muon event. Since the baseline recovery time depends on the muon energy deposition, the efficiency is assumed to depend on Q_μ .

The sigmoid function $(1 + e^{-\sigma x})^{-1}$ approximates an error-function-like turn-on behavior, with σ controlling the steepness of the transition. The free parameters σ , a , and b are tuned to reproduce the observed distributions of ^{10}C decay candidates. Two observables are used in the tuning procedure: dR , the spatial distance to the nearest neutron capture associated with a given muon shower, and ENN , the effective number of tagged neutrons. The dR distribution is sensitive to vertex resolution, while ENN is primarily influenced by neutron tagging efficiency. Figure 5.13 shows the tuned FLUKA predictions compared with data.

isotope	decay mode	Q-value (MeV)	half-life (s)	ROI (day-kton) ⁻¹	Total (day-kton) ⁻¹
⁸⁸ Y	EC/ β^+/γ	3.62	9.212×10^6	0.110	0.136
^{90^m} Zr	IT	2.31	8.092×10^{-1}	0.012	0.093
⁹⁰ Y	EC/ β^+/γ	6.11	9.212×10^5	0.024	0.095
⁹⁶ Tc	EC/ β^+/γ	2.97	3.698×10^5	0.012	0.059
⁹⁸ Rh	EC/ β^+/γ	5.06	5.232×10^2	0.011	0.076
⁹⁸ Rh	EC/ β^+/γ	3.63	7.488×10^4	0.088	0.234
¹⁰³ Ag	EC/ β^+/γ	4.28	4.152×10^3	0.012	0.160
^{104^m} Ag	EC/ β^+/γ	4.28	2.010×10^3	0.018	0.111
¹⁰⁷ Cd	EC/ β^+/γ	3.43	1.944×10^3	0.019	0.135
¹⁰⁸ In	EC/ β^+/γ	5.16	3.480×10^3	0.089	0.194
¹¹⁰ In	EC/ β^+/γ	3.89	1.771×10^4	0.053	0.236
^{110^m} In	EC/ β^+/γ	3.89	4.146×10^3	0.066	0.351
¹¹⁰ Sn	EC/ β^+/γ	3.85	1.080×10^3	0.027	0.122
¹¹³ Sb	EC/ β^+/γ	3.92	4.002×10^2	0.036	0.231
¹¹⁴ Sb	EC/ β^+/γ	5.88	2.094×10^2	0.020	0.297
¹¹⁵ Sb	EC/ β^+/γ	3.03	1.926×10^3	0.031	0.839
¹¹⁶ Sb	EC/ β^+/γ	4.71	9.480×10^2	0.071	0.939
¹¹⁸ Sb	EC/ β^+/γ	3.66	2.160×10^2	0.165	1.288
¹¹⁶ Te	EC/ β^+/γ	2.90	5.201×10^6	0.016	0.054
¹¹⁵ Te	EC/ β^+/γ	4.64	3.489×10^2	0.012	0.124
¹¹⁷ Te	EC/ β^+/γ	3.54	3.720×10^3	0.052	0.584
¹¹⁹ I	EC/ β^+/γ	3.51	1.146×10^3	0.053	0.533
¹²⁰ I	EC/ β^+/γ	5.62	4.896×10^3	0.091	0.953
¹²² I	EC/ β^+/γ	4.23	2.178×10^2	0.289	1.965
¹²⁴ I	EC/ β^+/γ	3.16	3.608×10^5	0.190	1.654
¹⁰⁸ I	β^-/γ	2.95	4.450×10^4	0.195	1.188
¹³² I	β^-/γ	3.58	8.262×10^3	0.148	0.427
¹³⁴ I	β^-/γ	4.18	3.150×10^3	0.043	0.183
¹²¹ Xe	EC/ β^+/γ	3.75	2.406×10^3	0.100	0.540
¹²⁵ Cs	EC/ β^+/γ	3.09	2.802×10^3	0.012	0.266
¹²⁶ Cs	EC/ β^+/γ	4.82	9.840×10^1	0.011	0.080
¹²⁸ Cs	EC/ β^+/γ	3.93	2.196×10^2	0.031	0.229

Table 5.3: Breakdown of ¹³⁶Xe spallation products. Isotopes with production rates exceeding 0.01 /day/XeLS-kton in the Region of Interest (ROI) were considered and included in the background model. Values from Reference [47].

Chapter 6

Backgrounds

In the search for excited-state double-beta decays in KamLAND-Zen, the signal is extracted through a fit to the reconstructed visible energy spectrum. While Chapter 4 described the event selection criteria applied to suppress background contributions in the data, the purpose of this chapter is to describe how the residual backgrounds that pass those selections are modeled and quantified. This chapter presents the expected energy distributions of all relevant background processes, together with the methods used to estimate their rates and associated uncertainties. These background models are implemented in the spectral fit described in Chapter 7, along with any independent constraints—such as delayed-coincidence measurements or external calibration studies—that can be placed on their intensities.

In many KamLAND-Zen analyses, spatial information—particularly the reconstructed radial distribution—is used as an additional discriminator between signal and background. However, due to limitations in the modeling of the radial distribution for this analysis, only the innermost region of the detector is used. As a result, the background discrimination relies primarily on spectral shape rather than spatial separation. Further discussion of the fiducial volume selection adopted for the excited-state analysis is provided in Chapter 7.

6.1 $2\nu\beta\beta$: Double-Beta Decay

Two-neutrino double-beta decay ($2\nu\beta\beta$) constitutes by far the dominant background in the search for excited-state double-beta decays ($2\nu\beta\beta$ s). In practice, the excited-state analysis is largely reduced to a search for small distortions in the continuous $2\nu\beta\beta$ energy spectrum, making an accurate modeling of this background essential. In KamLAND-Zen, two xenon isotopes undergo $2\nu\beta\beta$ decay: ^{136}Xe and ^{134}Xe . Of the xenon dissolved in the xenon-loaded liquid scintillator (XeLS), approximately 90% is ^{136}Xe and about 9% is ^{134}Xe . The remaining fraction consists of other xenon isotopes at negligible levels.

The $2\nu\beta\beta$ decay of ^{136}Xe has been observed and precisely measured by KamLAND-Zen and other experiments. In this analysis, the overall normalization of the ^{136}Xe $2\nu\beta\beta$ background is allowed to float freely in the spectral fit. This approach accounts for uncertainties in exposure, detection efficiency, and possible correlations with other background components. In contrast, the $2\nu\beta\beta$ decay of ^{134}Xe has not yet been observed. The current world-leading limit on its half-life is $T_{1/2} > 8.2 \times 10^{20}$ years at 90% confidence level [64]. If this limit is saturated, the corresponding decay rate in KamLAND-Zen XeLS would be approximately 2.7×10^4 events/day/kton.

Although ^{134}Xe decay could represent a secondary physics goal of KamLAND-Zen, its contribution is effectively unobservable in the present analysis. The expected signal is completely masked by residual low-energy backgrounds, most notably from ^{85}Kr and ^{210}Bi contamination in the detector. Furthermore, theoretical calculations predict the ^{134}Xe $2\nu\beta\beta$ half-life to be approximately three orders of magnitude longer than that of ^{136}Xe , implying a correspondingly smaller decay rate. For these reasons, the contribution of ^{134}Xe $2\nu\beta\beta$ decays is neglected in this analysis, and only the ^{136}Xe $2\nu\beta\beta$ component is included in the background model.

6.2 Radioactive Contamination

Radioactive contamination from naturally occurring radionuclides constitutes an important class of backgrounds in KamLAND-Zen. These backgrounds originate from trace impurities in detector materials, including the liquid scintillator volumes, balloon films, and structural components. This section describes the modeling and treatment of the dominant radioactive contaminants that contribute to the excited-state double-beta decay analysis.

6.2.1 ^{238}U Series

^{238}U is a naturally occurring radionuclide with a half-life of $T_{1/2} = 4.468 \times 10^9$ years and is responsible for approximately 40% of the radioactive heat generated within the Earth. As an omnipresent contaminant, trace amounts of ^{238}U are present in essentially all detector materials.

The ^{238}U decay chain includes a sequence of radioactive daughters such as Th, Pa, Ra, Rn, Po, Pb, Bi, and Tl. In the background model, all decays in the chain that produce visible energy above 0.5 MeV are included. Following standard KamLAND-Zen practice, the decay chain is divided into two sub-series based on the presence of ^{222}Rn . Decays occurring upstream of ^{222}Rn are referred to as *Series 1* ($^{238}\text{U}_{\text{s}1}$), while decays downstream of ^{222}Rn are referred to as *Series 2* ($^{238}\text{U}_{\text{s}2}$). The Series 1 component is introduced into the detector primarily through material contamination during detector construction and is therefore assumed to be in secular equilibrium. In contrast, the Series 2 component is introduced into the detector predominantly through ^{222}Rn ingress during the initial xenon loading into the XeLS. Because the mechanisms and histories of introduction differ, the rates of $^{238}\text{U}_{\text{s}1}$ and $^{238}\text{U}_{\text{s}2}$ are treated as independent parameters in the spectral fit.

In this analysis, the $^{238}\text{U}_{\text{s}1}$ rate is allowed to float freely and is determined di-

rectly from the energy spectrum. The $^{238}\text{U}_{\text{s}2}$ rate is constrained using the measured rate of tagged ^{214}Bi decays identified via the delayed-coincidence technique described in Chapter 4. This constraint is implemented as a penalty term in the likelihood function.

6.2.2 ^{232}Th Series

^{232}Th is another naturally occurring radioactive contaminant that contributes to the background in KamLAND-Zen. As with the ^{238}U chain, the ^{232}Th decay series is divided into two sub-series to account for possible breaks in secular equilibrium. Decays occurring upstream of ^{228}Th are referred to as *Series 1*, while those downstream of ^{228}Th are referred to as *Series 2*. All decays with visible energy above 0.5 MeV are included in the background model.

The rates of the two ^{232}Th sub-series are treated as independent free parameters in the spectral fit. In the higher-energy region between 3 and 5 MeV, the dominant contribution arises from the β^- decay of ^{208}Tl . As a result, the ^{208}Tl rate can be well constrained by the spectral fit, and the rates of other decays in the ^{232}Th chain are determined relative to the fitted ^{208}Tl activity.

6.2.3 ^{40}K

^{40}K is a common naturally occurring radionuclide that decays via β^- decay with an 89.28% branching ratio and via electron capture with a 10.72% branching ratio. Its half-life is $T_{1/2} = 1.248 \times 10^9$ years. As with other primordial radionuclides, ^{40}K may be present in detector materials such as the XeLS, balloon films, and KamLS. Due to the high level of purification achieved for the liquid scintillator, the contamination of ^{40}K within the scintillator volumes is expected to be negligible. Consequently, the dominant contribution of the ^{40}K background is assumed to originate from the inner balloon film. A dedicated study was performed to estimate the magnitude of

this film-related ^{40}K contamination. The most relevant feature of ^{40}K decay for the excited-state analysis is the 1.46 MeV γ ray emitted following electron capture. In the KamLS region outside the inner balloon, this monoenergetic peak is sufficiently prominent to be resolved above the continuous $2\nu\beta\beta$ background.

To estimate the contribution of film-related ^{40}K events reconstructed within the innermost XeLS volume, the radial distribution of events near the inner balloon boundary was examined. Spherical shells just inside and just outside the inner balloon were defined with equal volumes, and the energy spectrum in each shell was independently fitted using a simplified version of the full KamLAND-Zen spectral model.

The fitting model is a reduced version of the full spectral fit described in Chapter 7. The simplified fit configuration is summarized in Table 6.1. The model is designed to capture the dominant spectral features in the low-energy region. The fit is performed over the energy range 0.5–2.8 MeV, which includes the low-energy ^{85}Kr and ^{210}Bi contributions, the ^{11}C bump, the ^{136}Xe $2\nu\beta\beta$ spectrum and endpoint, and the ^{40}K gamma peak. Although the simplified model does not provide accurate estimates for all individual background components, the ^{40}K electron-capture peak is sufficiently distinct to allow a reliable determination of its contribution. The fit is performed using the same maximum-likelihood method as the full spectral analysis, minimizing the same χ^2 with respect to the reduced set of fit parameters.

The purpose of these fits is to measure the relative strength of the ^{40}K electron-capture peak as a function of radius. Each fit of a radial shell yields a measured number of ^{40}K events at that radius. The resulting radial dependence is compared with the expected distribution obtained from KLG4Sim simulations. A least-squares “fit-of-fits” procedure is then used to extract the overall ^{40}K activity associated with the inner balloon film. An example fit is shown in Figure 6.2.

An initial deviation from the expected radial distribution was observed, however,

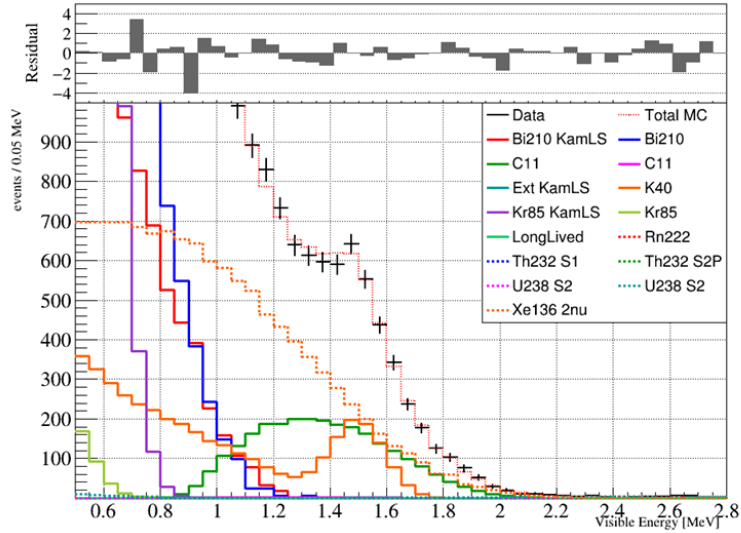


Figure 6·1: An example ^{40}K fit performed at $r = 15 \text{ m}^3$, outside the IB.

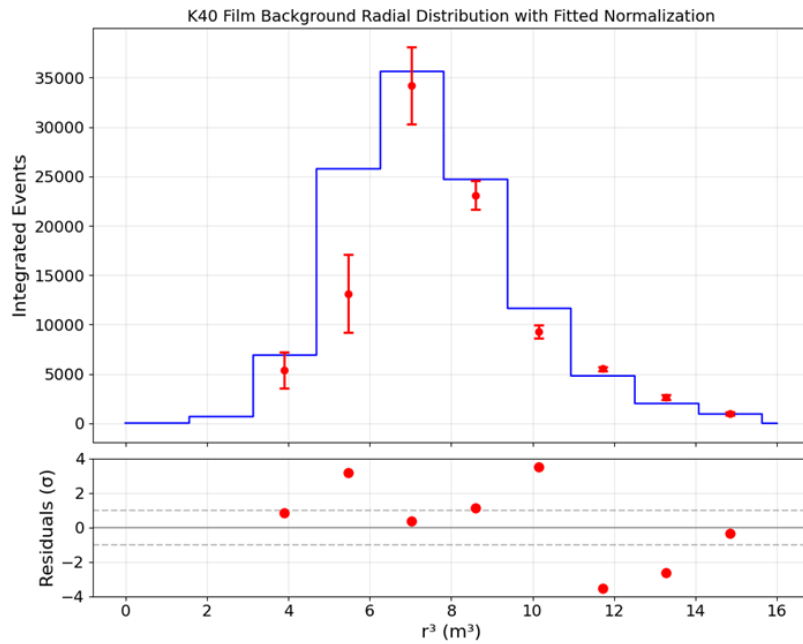


Figure 6·2: The fitted ^{40}K radial distribution. Each point is the fitted ^{40}K rate in a spherical section of the detector. The blue curve is the simulated radial distribution of ^{40}K originated in the inner balloon film. Error increases on and inside the inner balloon film due to large $2\nu\beta\beta$ background.

Material	Parameter	Fit Condition
XeLS	^{136}Xe $2\nu\beta\beta$	free
	^{238}U series 2	constrain
	^{222}Rn	constrain
	^{210}Bi	free
	^{85}Kr	free
	^{11}C	free
Film	Xe spallation	free
	^{238}U series 2	free
	^{232}Th series 2	free
KamLS	^{40}K	free
	^{11}C	free
	^{210}Bi	free
	^{85}K	free
	external gamma	fix
all	Energy scale	constrained
	k_B, R	constrained
	LL-distortion	constrain
	^6He	fix
	^{12}B	fix
	^8Li	fix
	^8B	fix

Table 6.1: Fit parameter configuration for the ^{40}K spectral analysis. The fit condition column indicates whether the parameter is free, fixed, scanned, or constrained in the fit.

after vetoing the upper balloon neck region, excellent qualitative agreement between data and simulation was obtained. This result supports the conclusion that the ^{40}K contamination is predominantly localized on the inner balloon film, with significantly lower contamination in the liquid scintillator volumes. This behavior is consistent with observations for the ^{238}U and ^{232}Th series. The final ^{40}K yield from the mini-balloon film is measured to be:

$$Y_{^{40}\text{K}, \text{film}} = 183 \pm 13 \text{ events/day} \quad (6.1)$$

This independently measured ^{40}K rate is incorporated into the spectral fit as a penalty term.

6.2.4 ^{85}Kr

^{85}Kr is a radioactive isotope released into the atmosphere primarily through the reprocessing of spent nuclear fuel. It undergoes β^- decay with a half-life of $T_{1/2} = 10.76$ years. Despite its relatively short half-life, the atmospheric concentration of ^{85}Kr has continued to increase due to ongoing nuclear fuel reprocessing. ^{85}Kr is expected to be introduced into KamLAND-Zen during liquid scintillator purification and handling. Previous KamLAND and KamLAND-Zen 400 analyses observed a non-uniform distribution of ^{85}Kr along the detector z -axis. In the present study, the ^{85}Kr rate is allowed to float freely within the inner XeLS volume. ^{85}Kr constitutes a significant background contribution in the low-energy region of the spectrum and is therefore an important component of the overall background model.

6.3 Carbon Spallation

A major class of backgrounds in both the $0\nu\beta\beta$ and $2\nu\beta\beta^*$ analyses arises from radioactive isotopes produced when high-energy cosmic-ray muons spallate carbon nuclei in the detector materials. In this work, spallation products are categorized according to their lifetimes. Isotopes with half-lives ranging from milliseconds to minutes are referred to as *short-lived* spallation products, while isotopes produced primarily via xenon spallation with much longer half-lives are referred to as *long-lived*. This section describes the modeling and estimation of backgrounds from short-lived carbon spallation products, as well as the dedicated treatment of the dominant spallation isotope, ^{11}C .

6.3.1 Short-Lived Spallation Products

The short-lived carbon spallation products—primarily ${}^6\text{He}$, ${}^8\text{B}$, ${}^8\text{Li}$, ${}^{10}\text{C}$, and ${}^{12}\text{B}$ —are effectively suppressed by the triple-coincidence veto techniques described in Chapter 4. Nevertheless, a small residual contribution remains due to imperfect tagging efficiency and detector deadtime. The residual background rate from these isotopes is estimated using a combined energy– dT fit, where dT is the time delay between the parent muon event and the subsequent radioactive decay. The event rate as a function of dT can be expressed as:

$$\frac{dN}{dt} = \sum_i N_i \exp\left(-\frac{dT}{\tau_i}\right) + C, \quad (6.2)$$

where N_i is the normalization of isotope i , τ_i is its mean lifetime, and C represents the rate of accidental, non-muon-correlated events. By simultaneously fitting the dT distributions of multiple isotopes together with the accidental component, the production rates of the individual spallation products can be extracted. The fit is performed in the energy range 2–5 MeV, while the resulting full energy spectra are used in the excited-state spectral analysis.

Figure 6.3 shows the result of the combined energy– dT fit. The fit is performed simultaneously over the three energy regions indicated in the figure. The residual background rates that survive the triple-coincidence veto are then estimated using the fitted production rates and the measured shower-veto selection efficiency. This estimation is performed using KamLS events. Any potential discrepancy between spallation production rates in KamLS and XeLS is included as a systematic uncertainty. The resulting short-lived spallation background rates are summarized in Table 6.2.

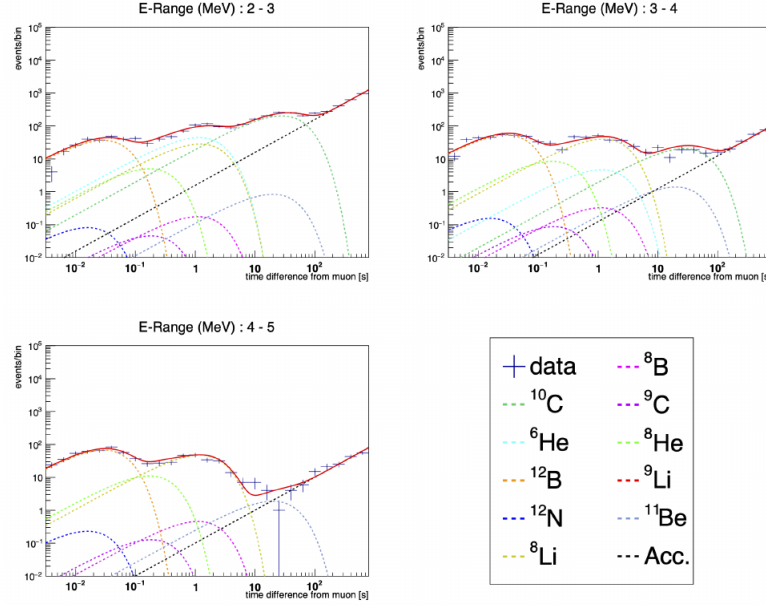


Figure 6.3: The fit to short-lived spallation backgrounds over Energy and dT . While the fit for the spallation rates is performed in the energy range 2-5 MeV, the full expected energy distributions are used in the excited state analysis spectral fit. Figure taken from Reference [47].

	E [MeV]	Lifetime τ	Prod. rate	Bkg. rate	Rej. eff.
			[evt/d/kton]	[evt/d/kton]	[%]
${}^6\text{He}$	3.51 (β^-)	1.16 s	$12.36^{+1.22}_{-1.28}$ (28 ± 2)	$0.33^{+0.23}_{-0.02}$	$97.6^{+1.7}_{-1.7}$
${}^{10}\text{C}$	3.65 (β^+)	27.8 s	$18.70^{+0.72}_{-0.64}$ (23 ± 2)	$0.00^{+0.03}_{-0.00}$	$100^{+0.00}_{-0.66}$
${}^8\text{Li}$	16.0 (β^-)	1.21 s	$25.77^{+0.92}_{-1.04}$ (47 ± 3)	$0.025^{+0.13}_{-0.14}$	$99.1^{+0.5}_{-0.5}$
${}^{12}\text{B}$	13.4 (β^-)	29.1 ms	$56.14^{+1.29}_{-1.28}$ (42 ± 3)	$0.015^{+0.002}_{-0.002}$	$100.0^{+0.0}_{-0.0}$
${}^8\text{B}$	18.0 (β^+)	1.11 s	$0.58^{+0.71}_{-0.44}$ (11 ± 1)	$0.07^{+0.09}_{-0.07}$	$88.3^{+14.8}_{-19.8}$
${}^{12}\text{N}$	17.3 (β^+)	15.9 ms	$0.218^{+0.20}_{-0.12}$ (0.74 ± 0.06)	0^{+0}_{-0}	100^{+0}_{-0}
${}^9\text{C}$	16.5 (β^+)	182.5 ms	$0.53^{+0.54}_{-0.44}$ (1.5 ± 0.1)	$0^{+0.01}_{-0}$	$100^{+0.0}_{-1.0}$
${}^8\text{He}$	10.7 (β^-)	171.7 ms	$4.89^{+0.93}_{-0.86}$ (0.55 ± 0.04)	$0^{+0.02}_{-0}$	$100^{+0}_{-0.3}$
${}^9\text{Li}$	13.6 (β^-)	257.2 ms	$0.00^{+1.19}_{-0}$ (4.9 ± 0.4)	$0^{+0.01}_{-0}$	-
${}^{11}\text{Be}$	11.5 (β^-)	19.9 s	$1.06^{+0.69}_{-0.21}$ (1.1 ± 0.1)	$0.00^{+0.26}_{-0}$	$100^{+0.0}_{-22.1}$

Table 6.2: Production and background rate of carbon spallation products. Values from Reference [60].

6.3.2 ^{11}C Spallation Estimation

Among all spallation products, ^{11}C is by far the dominant isotope in KamLAND-Zen. FLUKA simulations predict a ^{11}C production rate of 679 ± 49 events/day/kton, making it a clear outlier compared to other short- and long-lived isotopes. In addition, ^{11}C is the dominant background in the medium-energy range (1–2 MeV) of the KamLAND-Zen spectrum, aside from $2\nu\beta\beta$ itself. As a result, an accurate determination of the ^{11}C production rate is essential for constraining the $2\nu\beta\beta$ background normalization and for achieving sensitivity to excited-state decays.

The ^{11}C production rate was previously measured in KamLAND using KamLS data and muon-coincidence techniques. In this analysis, the measurement is repeated in KamLAND-Zen 800 using XeLS data and MoGURA-based neutron coincidence tagging.

The ^{11}C production rate is determined by selecting correlated $\mu-^{11}\text{C}$ decay pairs. The following selection criteria are applied:

- Muon delay: $100 < dT < 18,000$ s,
- Event quality cuts as described in Chapter 4, excluding the vertex badness veto to retain ^{11}C orthopositronium decays,
- Removal of other spallation-related vetoes (long-lived veto, MoGURA neutron veto, and ^{137}Xe veto),
- Spatial correlation: $dR < 80$ cm to the nearest neutron in the muon shower,
- Fiducial volume: $0 < r < 160$ cm,
- Energy selection: $1.0 < E_{\text{vis}} < 1.6$ MeV.

The lower bound of $dT > 100$ s suppresses contributions from short-lived spallation isotopes. Applying these selections to the full KamLAND-Zen 800 dataset yields the

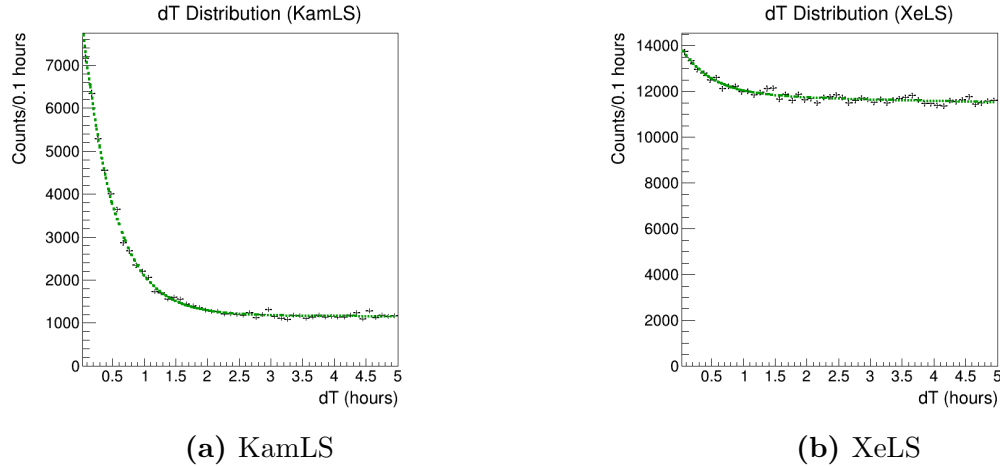


Figure 6.4: Distribution of dT (time delay from muon to event) for muon-event pairs passing all selection cuts, shown separately for KamLS and XeLS.

dT distributions shown in Figure 6.4 for both XeLS and KamLS. The distributions are fitted with an exponential decay corresponding to the known ^{11}C lifetime, $\tau = 1,764$ s, together with a linearly varying background to account for other long-lived spallation products with similar lifetimes.

An independent cross-check of the ^{11}C selection is performed using the reconstructed energy spectrum. The $\mu-^{11}\text{C}$ candidate events are divided into on-time and off-time samples based on dT . The energy spectrum of the off-time events is subtracted from that of the on-time events to remove accidental background contributions. The resulting background-subtracted energy spectra are shown in Figure 6.5. In KamLS, the agreement between the data and the simulated ^{11}C energy spectrum is clear. In XeLS, larger statistical fluctuations and residual background degrade the comparison. Nevertheless, the broad ^{11}C spectral shape is clearly resolved. This cross-check confirms that the selected sample is dominated by genuine ^{11}C decays.

There are many spallation isotopes produced in Xenon-spallation with lifetimes of similar orders of magnitude $10^3 - 10^4$ seconds as ^{11}C , $\tau = 1,764$ seconds. Instead of estimating the relative production of each of these isotopes, the effect of the cumulative

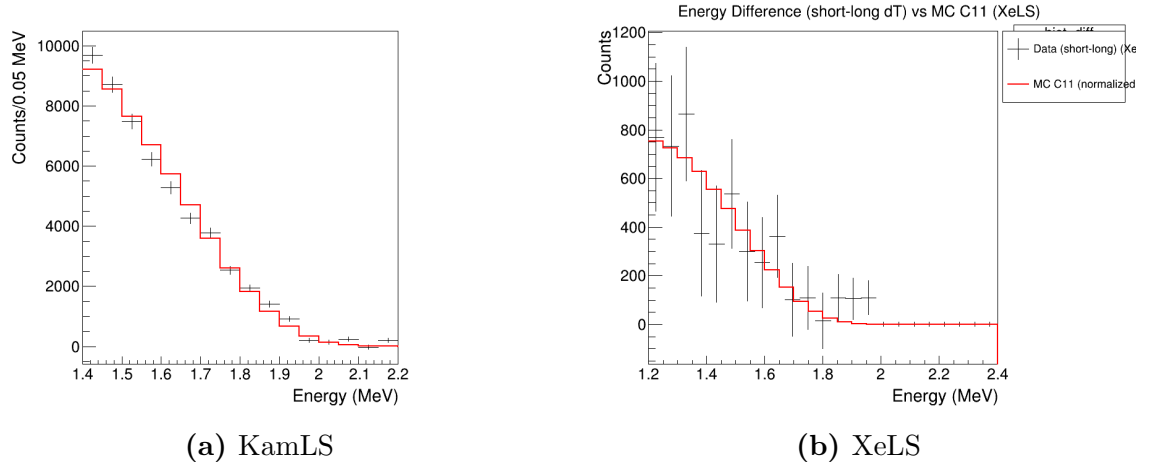


Figure 6.5: Subtracted energy distributions compared to MC ^{11}C in XeLS and KamLS.

background is modeled with an unconstrained linear slope to the background.

¹¹C Rate Calculation

The ^{11}C production rate in XeLS is derived from the exponential component of the dT fit. The expected number of detected, selected, and correlated $\mu-^{11}\text{C}$ pairs is modeled as:

$$I_{C11} = Y_{C11} \times E_{\text{FBE}} \times (1 - dt_{\text{MoG}}) \times \epsilon_{dR} \times \epsilon_{dT} \times \epsilon_{\text{FV}} \times \epsilon_E, \quad (6.3)$$

where the individual quantities are defined as follows:

- $I_{C11} = 10,028$: integral of the exponential component of the fit (observed $\mu^{-11}\text{C}$ pairs),
 - Y_{C11} : ^{11}C production rate (final result),
 - $E_{\text{FBE}} = 22.71$: XeLS exposure in kton·days,
 - $dt_{\text{MoG}} = 1.88\%$: MoGURA deadtime fraction,

- $\epsilon_{dR} = 57\%$: spatial correlation efficiency ($dR < 80$ cm), obtained from FLUKA tuned with ^{11}C data,
- $\epsilon_{dT} = 94.5\%$: efficiency of the $dT > 100$ s requirement,
- $\epsilon_{\text{FV}} \times \epsilon_E = 79.7\%$: combined fiducial volume and energy selection efficiency from KLG4Sim.

Using these inputs, the ^{11}C production rate in XeLS is calculated to be:

$$Y_{C11} = 1,050 \pm 110 \text{ events/(kton}\cdot\text{day).} \quad (6.4)$$

The uncertainty includes contributions from statistical error, exposure uncertainty, the choice of fit model, and neutron production modeling. The individual uncertainty components are summarized in Table 6.3.

6.3.3 ^{137}Xe

Neutrons produced by cosmic-ray muon spallation can be captured on ^{136}Xe nuclei, producing the radioactive isotope ^{137}Xe . The β^- decay of ^{137}Xe has a Q -value of 4.16 MeV and a half-life of $T_{1/2} = 229$ s. Based on the neutron capture cross section, the ^{137}Xe production rate is estimated to be 3.9 events/day/kton. The tagging efficiency of ^{137}Xe using neutron coincidence techniques is estimated to be $74 \pm 7\%$. The

Source	Uncertainty (%)
Statistical	5.4
Exposure uncertainty	4.0
Exponential fit model choice	7.0
Neutron production	7.8
Total uncertainty	10.7

Table 6.3: Sources of uncertainty in the ^{11}C production rate calculation.

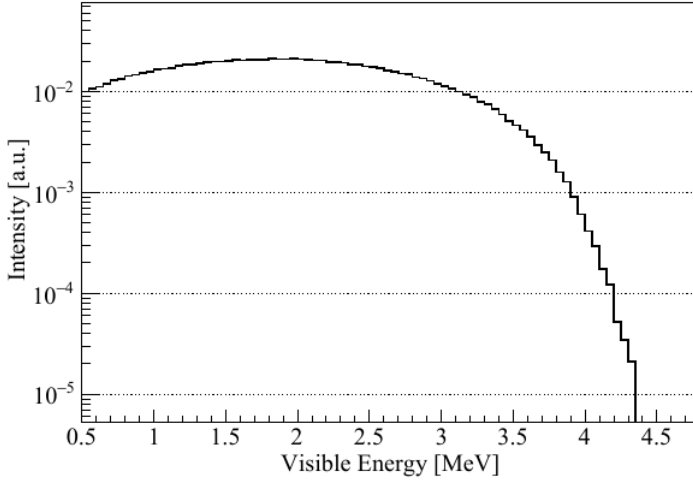


Figure 6.6: The fit to short-lived spallation backgrounds over Energy and dT . While the fit for the spallation rates is performed in the energy range 2–5 MeV, the full expected energy distributions are used in the excited state analysis spectral fit. Figure taken from Reference [47].

long-lived spallation veto described in the following section also removes a fraction of ^{137}Xe events. The efficiency of this veto is estimated from FLUKA simulations to be 42%. After applying all vetoes, the residual ^{137}Xe background rate in the singles dataset is estimated to be 0.43 ± 0.36 events/day/kton.

6.4 Long-Lived Xenon Spallation Products

Long-lived spallation products originating from ^{136}Xe constitute one of the most important background classes in KamLAND-Zen, particularly near the $0\nu\beta\beta$ region of interest (ROI). In the context of the excited-state analysis, these backgrounds are also relevant because they contribute non-negligible spectral structure at energies above the bulk of the $2\nu\beta\beta$ spectrum. If not modeled accurately, residual long-lived spallation backgrounds can bias the inferred $2\nu\beta\beta$ spectral shape near its endpoint and can mimic or distort weak signal features.

Compared to carbon spallation products (typically decay on millisecond–minute timescales) xenon spallation products often have half-lives of hours to days. This

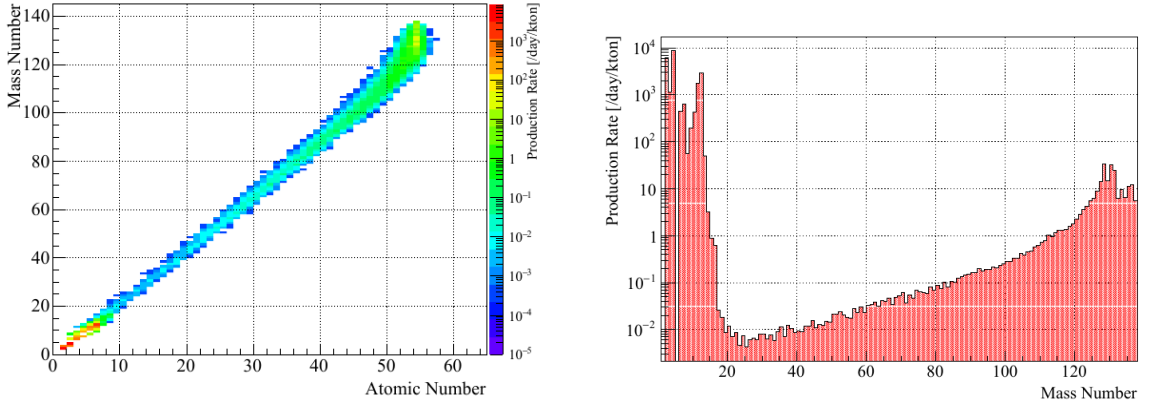
makes their identification by simple time-coincidence or box-cut methods substantially more difficult: the parent muon can be separated from the subsequent decay by timescales comparable to typical run lengths, and accidental coincidences dominate if one attempts direct muon–decay matching.

In the standard $0\nu\beta\beta$ analysis, KamLAND-Zen employs a likelihood-based tagging strategy to classify events into a lower-contamination “Singles” sample and a spallation-enriched “Long-Lived” sample. For the present excited-state analysis, this dataset separation is not applied. The primary motivation is to reduce systematic complexity in the modeling of the much larger ^{11}C contribution in the excited-state energy region. Consequently, the long-lived xenon-spallation contribution must be estimated and constrained using a simulation-driven approach, as described below.

6.4.1 FLUKA Simulation

To estimate the production yields of xenon spallation products, cosmic-ray muons are simulated in a simplified geometry that captures the relevant target materials and shielding volumes. In the FLUKA environment, concentric spherical regions of XeLS ($0 < r < 192$ cm), KamLS ($192 < r < 650$ cm), and buffer oil (outer radius ~ 9 m) are modeled. The muon energy and angular distributions at the Kamioka site are taken from MUSIC simulations of the underground muon flux.

A total of 10^7 muon events (μ^+ and μ^-) are generated, corresponding to an effective exposure of approximately 37 years of KamLAND observation. The muon charge ratio is set to $\mu^-/\mu^+ = 1.3$. The resulting FLUKA output provides the relative production yields of a large number of nuclides created by muon-induced spallation in XeLS. Figure 6.7a summarizes the production landscape as a function of (Z, A) and highlights the dominant production regions.



(a) Atomic mass number A vs. atomic number Z .

(b) Production yield vs. atomic mass number A .

Figure 6.7: Production rates of spallation nuclei in KamLAND-Zen XeLS. Two concentrations are visible: one near the primary heavy isotope (^{136}Xe), and another near lighter scintillator components (e.g., $A \sim 10$) such as carbon- and oxygen-related fragments. Figure adapted from Ref. [52].

6.4.2 ENSDF Database

FLUKA is used to model the muon-induced spallation production process, but it does not generate the full radioactive decay chains for the produced isotopes within the detector response framework used elsewhere in the analysis. Instead, FLUKA provides the *relative production yields* of spallation products, and the subsequent radioactive decays are simulated within KLG4Sim using GEANT4, consistent with the treatment of other backgrounds and signals.

For each isotope produced in the FLUKA simulation, the half-life, decay modes, branching ratios, and daughter transitions are taken from the Evaluated Nuclear Structure Data File (ENSDF). The full decay chains are then propagated using the GEANT4 `RadioactiveDecay` process, and the resulting decay vertices and emitted particles are passed through the same detector-response simulation and reconstruction chain as the analysis data. This procedure yields both the expected *visible-energy spectra* and the expected *relative contributions* of long-lived xenon spallation products

in the excited-state analysis window.

Table 5.3 summarizes the dominant long-lived spallation contributions used in the fit. While FLUKA produces hundreds of isotopes in total, the subset listed in Table 5.3 accounts for more than 95% of the expected long-lived spallation background in the relevant energy range.

6.4.3 Spectrum Distortion

In the absence of a dedicated KamLAND-Zen measurement of xenon spallation yields and decay spectra induced by cosmic-ray muons, validating the absolute accuracy of the FLUKA-based long-lived spallation model is challenging. To quantify a realistic model uncertainty, external beam measurements are used as a cross-check on the FLUKA predictions.

Two relevant beam datasets are considered. First, a 490 GeV μ^+ beam on gaseous xenon measured charged-hadron production yields, which can be reproduced by dedicated FLUKA benchmark simulations [65]. Second, heavy-ion measurements of ^{136}Xe incident on a liquid-hydrogen target were performed at 500 MeV/nucleon and at 1 GeV/nucleon [66, 67]. These beam data provide a practical handle on the level of spectral disagreement that may arise from modeling uncertainties in hadronic fragmentation and secondary production.

Figure 6.8 shows the relative difference between the FLUKA-derived long-lived spallation spectrum and the beam-measurement-inferred expectations. The discrepancy indicates a possible mismodeling of the long-lived spallation energy distribution, particularly in and near the $0\nu\beta\beta$ ROI. To propagate this uncertainty into the excited-state spectral fit, a distortion (shape-nuisance) parameter is introduced that deforms the nominal long-lived spallation spectrum according to the observed discrepancy. The larger deviation (red curve) is adopted as a conservative shape uncertainty, consistent with standard practice when external validation is limited.

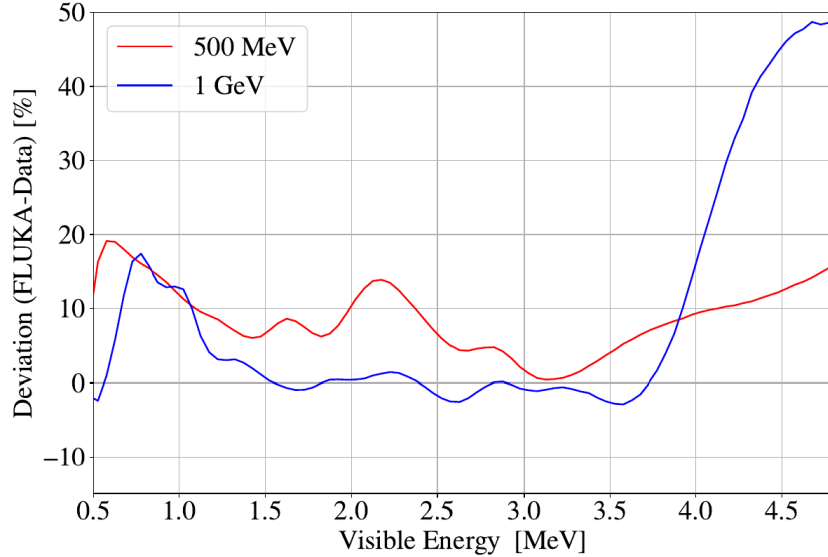


Figure 6.8: Comparison between FLUKA predictions and xenon beam data constraints. The red curve shows the difference inferred from Reference [66], and the blue curve shows the difference from Reference [67]. The red curve is adopted as a conservative distortion uncertainty because it produces the larger deviation near the $0\nu\beta\beta$ ROI.

6.5 Other Backgrounds

6.5.1 External Gamma Rays

Gamma rays emitted by radioactive isotopes outside the active scintillator volumes can penetrate into the detector and deposit visible energy. The dominant contribution of this type arises from the 2.6 MeV gamma ray emitted in the decay of ^{208}Tl , which is present primarily in the PMT glass and surrounding detector materials. Because these sources are external to the XeLS target, the resulting background exhibits a strong radial dependence, decreasing rapidly toward the detector center due to attenuation and geometric effects.

The energy and spatial distributions of external gamma-ray backgrounds are estimated directly from data rather than simulation. Events are selected in an energy window around the ^{208}Tl gamma line, and their radial distribution is modeled as the

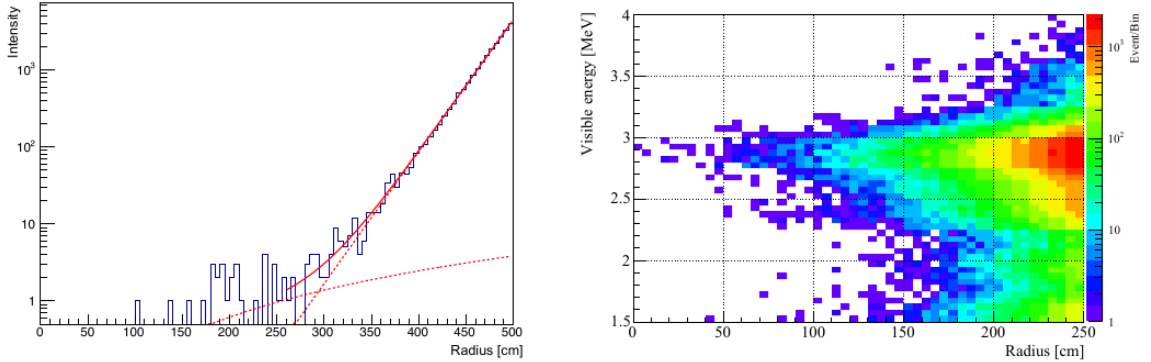


Figure 6.9: Characterization of external gamma-ray backgrounds in KamLAND-Zen. (Left) Radial distribution of events in the 2.6–2.65 MeV energy window, fitted with the sum of an exponential component (external gamma rays) and a second-degree polynomial component (radially uniform backgrounds). (Right) Modeled energy and radial distributions of external gamma-ray events. The 2.6 MeV ^{208}Tl gamma peak appears near 2.8 MeV due to the higher light yield of the outer KamLS and the calibration of E_{vis} to XeLS events. Figures adapted from Reference [52].

sum of an exponentially falling component, representing external gamma rays entering the detector, and a second-degree polynomial component, representing radially uniform internal backgrounds.

Figure 6.9 shows the reconstructed radial distribution of events with visible energies between 2.6 and 2.65 MeV. The fitted exponential component is extrapolated inward to estimate the residual external gamma-ray contribution in the fiducial volume. Using this method, the background rate within $r < 300$ cm is estimated to be 0.32 ± 0.05 events/day/kton for $z < 0$ and 0.69 ± 0.12 events/day/kton for $z > 0$. The corresponding modeled energy and radius distributions are shown in Figure 6.9.

Within the innermost fiducial volume used for the excited-state analysis ($r < 1.33$ m), the extrapolated contribution from external gamma rays is negligible. Consequently, this background component is not included explicitly in the spectral fit for the excited-state decay search.

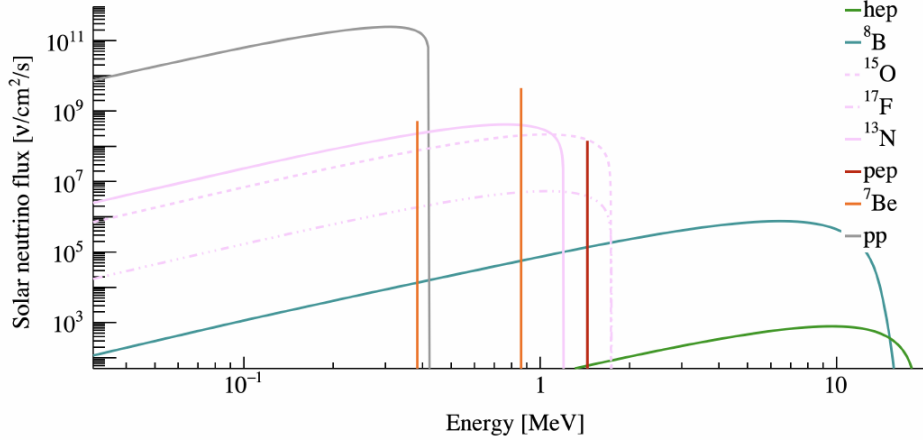


Figure 6.10: Energy spectra of solar neutrino fluxes. Figure adapted from [68].

6.5.2 Solar Neutrinos

Neutrino interactions constitute an irreducible background for searches for rare processes in KamLAND-Zen. Relevant neutrino sources include solar neutrinos, atmospheric neutrinos, geoneutrinos, and reactor antineutrinos. Among these, solar neutrinos dominate the interaction rate at visible energies below approximately 20 MeV and are therefore the most relevant for the present analysis.

Neutrinos interact in the detector primarily via elastic scattering (ES) on electrons and charged-current (CC) interactions on nuclei. In elastic scattering, a neutrino transfers a fraction of its energy to an electron, which subsequently deposits energy in the liquid scintillator. The resulting recoil electron spectrum reflects the incident neutrino energy distribution. Figure 6.10 shows the expected solar neutrino fluxes as a function of energy. Of these, ${}^8\text{B}$ solar neutrinos provide the dominant contribution near the $2\nu\beta\beta$ endpoint region. Other solar neutrino components occur at lower energies and are negligible compared to internal radioactive backgrounds; they are therefore neglected in this analysis.

Charged-current interactions of solar neutrinos on xenon nuclei also contribute to

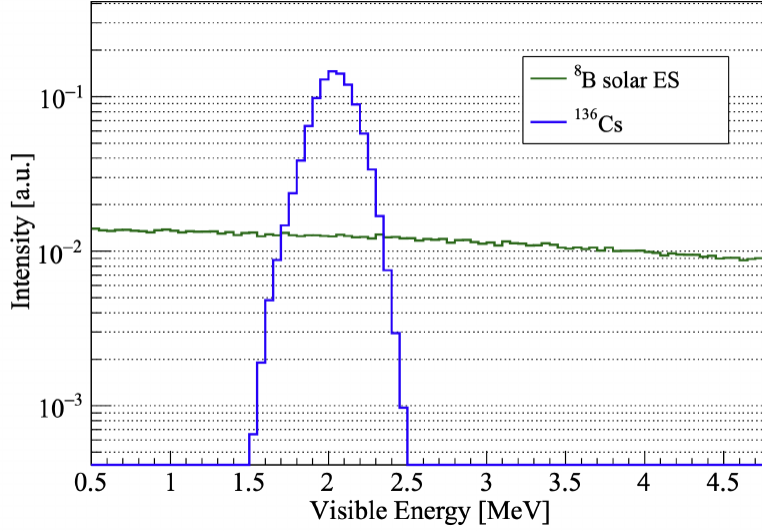


Figure 6.11: Modeled solar neutrino backgrounds included in the excited-state analysis, including ^8B elastic scattering and ^{136}Cs beta decay. Figure adapted from [52].

the background. In particular, electron neutrinos can interact with ^{136}Xe via:



The produced ^{136}Cs subsequently decays to ^{136}Ba with a half-life of $T_{1/2} = 13.01$ days and a decay Q -value of 2.55 MeV. The resulting beta decay produces a continuous visible-energy spectrum extending into the region relevant for excited-state decays.

Figure 6.11 shows the modeled visible-energy spectra of ^8B solar neutrino elastic scattering and ^{136}Cs decays. Both components are included explicitly in the spectral fit for the excited-state decay analysis.

Chapter 7

$2\nu\beta\beta^*$ Analysis

This chapter describes the analysis framework used to search for the $2\nu\beta\beta^*$ decay of ^{136}Xe in KamLAND-Zen 800. We first summarize the xenon loading and enrichment used to normalize decay rates. We then define the full dataset used in this work, including data-taking periods excluded specifically for the excited-state analysis. Next, we summarize the dominant sources of systematic uncertainty. Finally, we describe the one-dimensional binned spectral fit used to extract (or constrain) the $2\nu\beta\beta^*$ rate, and we present both a profile-likelihood (Wilks) limit and a Feldman–Cousins construction to obtain correct 90% confidence-level coverage.

7.1 Xenon Enrichment in KamLAND-Zen

The ^{136}Xe exposure is a normalization factor for all xenon decay rates. The total mass of xenon dissolved into the XeLS is estimated by accounting for xenon remaining in the handling system after installation:

1. initial xenon mass: 769 ± 1 kg,
2. xenon remaining in LS tanks and pipelines: 21.5 ± 2.8 kg,
3. xenon remaining in storage bottles: 1 ± 1 kg,
4. xenon trapped in the charcoal filter and/or used for sampling: 1.5 ± 0.5 kg.

From these terms, the installed Xenon gas is determined to be, 745 ± 3 kg. The isotopic composition of the enriched xenon is evaluated using a mass spectrometer. The

	^{136}Xe	^{134}Xe	Others	Total
Provided fraction [%]	90.85	8.82	0.33	100.00
Measured fraction [%]	90.77 ± 0.08	8.96 ± 0.02	—	—
Atomic mass [u]	135.907	133.905	—	—
Total mass [kg]	677.39	64.83	2.79	745.0

Table 7.1: Enriched xenon composition used in this analysis.

measured values agree with the enrichment specification provided by the supplier. The enrichment fractions and the corresponding ^{136}Xe mass are summarized in Table 7.1.

7.2 Full KamLAND-Zen 800 Dataset

The dataset used in this analysis was collected between February 5, 2019 and April 30, 2023 (run range 15431–18691). Unlike the primary $0\nu\beta\beta$ analysis, the excited-state search presented here does not subdivide the data by long-lived spallation likelihood. Instead, all events passing the selections in Chapter 4 are combined into a single energy spectrum and fitted simultaneously.

7.2.1 Vetoed Data Periods

In addition to standard run-quality selections and detector deadtime described in Chapter 4, we exclude several data-taking periods that are specific to this analysis.

Electric power supply instability

Runs 16790–16874 are excluded because the data acquisition system was unstable due to automatic voltage regulator (AVR) issues. Frequent DAQ restarts produced many short runs, which prevents stable run-by-run calibration as described in Chapter 5.

MoGURA disorder period

MoGURA data were unstable between September and November 2022 and some raw files were corrupted. While KamDAQ files remain readable, MoGURA information is required to reconstruct and tag events close in time to cosmic-ray muons, which provides key constraints on muon-correlated spallation backgrounds. Therefore, runs 17768–17905 are excluded from this analysis.

7.3 Systematic Uncertainties

Although the $2\nu\beta\beta^*$ search is dominated by statistical uncertainty from the large $2\nu\beta\beta$ background, several systematic effects contribute non-negligibly to the final limit. The uncertainty in the total xenon mass dissolved in the XeLS is taken as 0.4% from an internal study. The xenon enrichment uncertainty is taken as the difference between the supplier specification and the mass-spectrometer measurement (0.1%). The detector energy response drifts slowly over time due to electronics changes and PMT performance. Using the 2.2 MeV neutron-capture peak, we assign a conservative 0.9% uncertainty on the energy scale.

Finally, the fiducial-volume (FV) uncertainty reflects the uncertainty in the true volume enclosed by the FV cut. This is evaluated using uniformly distributed ^{222}Rn introduced during xenon loading, tagged via $^{214}\text{Bi-Po}$ delayed coincidences. Comparing the expected volume ratio of the FV to the inner balloon volume (0.5686) with the observed Bi–Po ratio (0.5454), we assign a 4.1% FV uncertainty.

7.4 Spectral Fit

The $2\nu\beta\beta^*$ decay rate is extracted (or constrained) by fitting signal and background models to the reconstructed visible-energy spectrum of data events within the reduced fiducial volume $r < 1.33$ m, after applying the event selections described in Chapter 4.

In contrast to analyses that bin the data in time and/or hemisphere, we adopt a single one-dimensional spectral fit to reduce complexity and mitigate systematics associated with time-dependent detector response and imperfect spatial modeling. This choice is additionally motivated by the fact that the excited-state search is dominated by the statistical precision of the underlying $2\nu\beta\beta$ spectrum.

The fit is performed over $E_{\text{vis}} = 0.5\text{--}4.8$ MeV using 0.05 MeV-wide bins. This window includes the low-energy radioactive backgrounds (^{85}Kr and ^{210}Bi), cosmogenic contributions (^{11}C), the ^{40}K peak, the $2\nu\beta\beta$ endpoint region, and the $2\nu\beta\beta^*$ region of interest.

7.4.1 Likelihood (NLL) Definition

We perform a binned maximum-likelihood fit using Poisson statistics for each energy bin and Gaussian penalty terms for externally constrained parameters. Following the formulation used in the analysis summary slides, the fit minimizes the negative log-likelihood (NLL), written schematically as :contentReference[oaicite:1]index=1

$$-\ln L(\boldsymbol{\eta}, \boldsymbol{\theta}) = \sum_{i=1}^{N_{\text{bins}}} [\nu_i(\boldsymbol{\eta}, \boldsymbol{\theta}) - n_i \ln \nu_i(\boldsymbol{\eta}, \boldsymbol{\theta})] + \sum_{j=1}^{N_{\text{constr}}} \frac{(\theta_j - \theta_{j,0})^2}{2\sigma_j^2} + \text{const.}, \quad (7.1)$$

where n_i is the observed number of events in energy bin i , and ν_i is the expected number of events in that bin given the model parameters. The vector $\boldsymbol{\eta}$ denotes free (or scanned) parameters such as component normalizations, while $\boldsymbol{\theta}$ denotes constrained nuisance parameters (e.g., background rates constrained by independent measurements and detector-response parameters). The Gaussian penalty terms implement external constraints with central values $\theta_{j,0}$ and standard deviations σ_j .

For numerical stability (including bins with $n_i = 0$), the equivalent Poisson de-

viance form is often used:

$$\chi^2_{\text{Poisson}} = 2 \sum_{i=1}^{N_{\text{bins}}} \left[\nu_i - n_i + n_i \ln \left(\frac{n_i}{\nu_i} \right) \right] \quad (7.2)$$

with the convention that the $n_i \ln(n_i/\nu_i)$ term is zero when $n_i = 0$. In this work, we report fit quality and profile scans using the test statistic:

$$\Delta\chi^2(\mu) \equiv 2 [-\ln L(\mu) + \ln L(\hat{\mu})] \quad (7.3)$$

where μ denotes the fixed (scanned) $2\nu\beta\beta^*$ signal rate and $\hat{\mu}$ is its best-fit value.

7.4.2 Model Prediction per Energy Bin

The expected bin counts are computed as a sum over templates:

$$\nu_i(\boldsymbol{\eta}, \boldsymbol{\theta}) = \sum_k \eta_k T_{k,i}(\boldsymbol{\theta}) \quad (7.4)$$

where $T_{k,i}$ is the predicted spectral shape (template) for component k in bin i , including detector-response effects such as energy scale and nonlinearity. The coefficients η_k represent the fitted normalizations (rates) of each background and the signal.

An overall energy-scale parameter α_E is implemented by mapping reconstructed energy to simulated energy via $E_{\text{vis}} = \alpha_E E_{\text{sim}}$ and using linear interpolation of templates to compute ν_i .

7.4.3 Minimization and Fit Configuration

The NLL is minimized using the MINUIT package [69] in the ROOT framework [70]. The fit parameters are grouped by source location (XeLS and inner balloon film). The overall configuration is summarized in Table 7.2. This analysis uses 29 fit parameters in total, with a mixture of fixed, free, and constrained parameters.

The constrained radioactive-chain rates (${}^{238}\text{U}$ series 2, ${}^{222}\text{Rn}$, and ${}^{232}\text{Th}$ series

Material	Parameter	Fit Condition
XeLS	^{136}Xe $2\nu\beta\beta^*$	scan
	^{136}Xe $2\nu\beta\beta$	free
	^{238}U series 2	constrained
	^{222}Rn	constrained
	^{232}Th series 2	constrained
	^{210}Bi	free
	^{85}Kr	free
	^{11}C	constrained
	^{137}Xe	constrained
	Xe spallation	free
Film	solar ν (ES+CC)	fixed
	^{136}Cs	constrained
	^{238}U series 1	fixed
	^{238}U series 2	free
	^{232}Th series 1	free
	^{232}Th series 2	free
	^{40}K	constrained
All	^{210}Bi	free
	Energy scale α_E	constrained
	k_B, R	fixed
	LL distortion	constrained
	^6He	fixed
	^{12}B	fixed
	^8Li	fixed
	^8B	fixed

Table 7.2: Fit parameter configuration for the spectral analysis. The fit condition column indicates whether parameters are free, fixed, scanned, or constrained in the fit.

2) are obtained from coincidence-tagged Bi–Po events (Chapter 4). The ^{11}C and ^{40}K constraints come from independent measurements described in Chapter 6. The ^{137}Xe constraint is derived from its correlation with muon-induced neutrons tagged by MoGURA (Chapter 6).

A penalty term is also included for detector-response parameters, most importantly the global energy scale. Although the short-term energy-scale stability, evaluated using the 2.2 MeV neutron-capture peak, is better than 1%, the global energy-scale parameter in the spectral fit is constrained more conservatively. Following the approach adopted in previous KamLAND-Zen analyses and theses [45, 47], we apply a Gaussian prior of $\alpha_E = 1 \pm 0.016$ to account for residual nonlinearity, spatial dependence, and long-term variations not explicitly modeled in the fit while keeping k_B and the Cherenkov fraction R fixed for fit stability.

7.5 $2\nu\beta\beta^*$ Results

7.5.1 Best-Fit Result

The spectral fit to the full KamLAND-Zen 800 dataset yields a best-fit $2\nu\beta\beta^*$ signal rate consistent with zero, indicating no statistically significant excess above the background-only hypothesis. Figure 7.1 shows the fitted energy spectrum in the reduced fiducial volume ($r < 1.33$ m), together with the dominant background components and the expected signal shape.

Table 7.3 summarizes the best-fit parameter values and their fit conditions. All constrained parameters remain within their assigned prior uncertainties, indicating no significant tension between the data and the background model. A notable feature of the fit is the ^{232}Th S1 contribution on the mini-balloon film, which is driven to zero. This behavior is expected, as the ^{232}Th S1 film background is spectrally degenerate with the ^{232}Th S2P film component in the absence of strong radial discrimination.

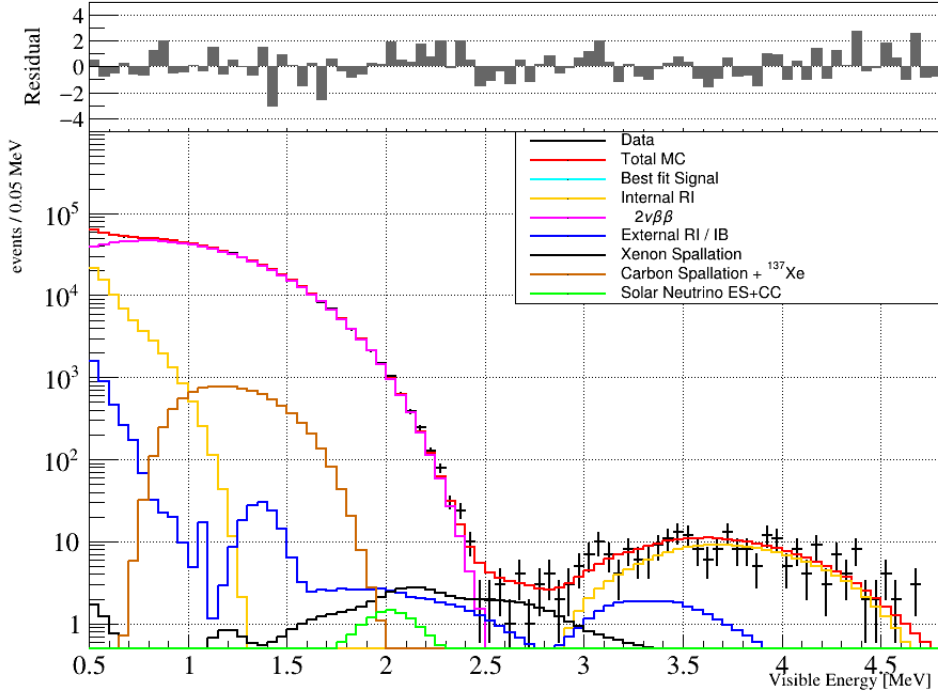


Figure 7.1: Best-fit energy spectrum for the full KamLAND-Zen 800 dataset in the reduced fiducial volume $r < 1.33$ m.

Since both components originate from the mini-balloon film and exhibit similar spatial and spectral characteristics, the inclusion of both parameters introduces redundancy, with the fit naturally preferring a single effective contribution. Overall, the stability of the fit and the absence of pathological parameter behavior demonstrate that the background model provides an adequate description of the data in the energy region relevant for the $2\nu\beta\beta^*$ search.

7.5.2 $2\nu\beta\beta^*$ Half-life Limits

In the absence of a statistically significant $2\nu\beta\beta^*$ signal, an upper limit on the decay rate is derived at the 90% confidence level (C.L.). This is achieved by performing a profile likelihood scan over the $2\nu\beta\beta^*$ signal rate. For each fixed signal-rate hypothesis, the remaining background parameters are re-optimized to minimize the negative log-likelihood (NLL). The degradation in the agreement between the model and the

Parameter	Value	Fit Condition
^{12}B Spallation	0.016	fix
^8B Spallation	0.239	fix
^{210}Bi (XeLS)	26000	floated
^{210}Bi (film)	22930	floated
^{11}C (XeLS)	983	constrained
^{136}Cs (XeLS)	0.8	fix
^6He Spallation	0.33	fix
^{40}K (film)	186	constrained
^{85}Kr (XeLS)	41500	floated
^8Li Spallation	0.525	fix
Long-lived (XeLS)	0.68	floated
Monochromatic	3.4e+07	fix
^{222}Rn (XeLS)	8002.15	constrained
Signal ($2\nu\beta\beta^*$, XeLS)	0	floated
Solar ν (XeLS)	4.87	fix
^{232}Th S1 (film)	0	floated
^{232}Th S2P (XeLS)	114	constrained
^{232}Th S2P (film)	98.7	floated
^{238}U S1 (film)	25	fix
^{238}U S2 (XeLS)	30.2	constrained
^{238}U S2 (film)	61.3	floated
^{136}Xe $2\nu\beta\beta$ (XeLS)	107601	floated
^{137}Xe (XeLS)	0.980653	constrained
Energy Scale α (Internal)	0.991	constrained
LL distortion	0.118	constrained
R (Internal)	0.018	fix
k_B (Internal)	0.31	fix

Table 7.3: The best fit parameter values and their fit conditions.

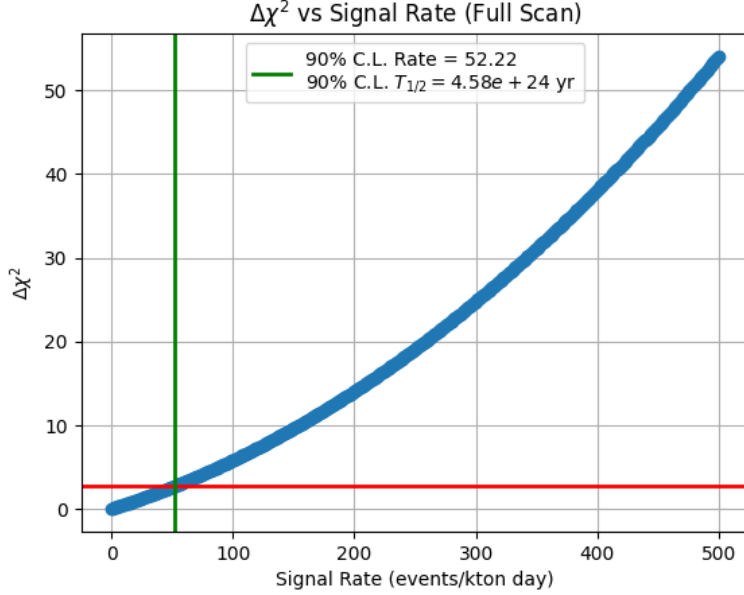


Figure 7.2: Difference in the NLL test statistic as a function of fixed $2\nu\beta\beta^*$ signal rate. The horizontal line indicates the Wilks' theorem threshold corresponding to a one-parameter 90% C.L.

data is quantified by the test statistic:

$$\Delta\chi^2 = 2 [\text{NLL}(\text{rate}) - \text{NLL}_{\text{best fit}}] \quad (7.5)$$

where $\text{NLL}_{\text{best fit}}$ corresponds to the global minimum. The result of this scan is shown in Figure 7.2.

Under the assumptions of Wilks' theorem [71], the 90% C.L. upper limit on the signal rate is obtained by identifying the rate at which $\Delta\chi^2 = 2.71$, corresponding to the 90% quantile of the χ^2 distribution with one degree of freedom. The corresponding lower limit on the $2\nu\beta\beta^*$ half-life is calculated as:

$$T_{1/2} = \frac{\ln(2) N_{^{136}\text{Xe}}}{(\text{rate}) \times 365.2}, \quad (7.6)$$

where $N_{^{136}\text{Xe}}$ is the number of ^{136}Xe atoms in the xenon-loaded liquid scintillator

(XeLS). The xenon concentration in the XeLS is given by:

$$C_{\text{Xe}} = \frac{\text{Xe mass}}{\text{total XeLS mass}} \times 100 \quad (7.7)$$

$$= \frac{745 \text{ kg}}{30.5 \text{ m}^3 \times 780.13 \text{ kg/m}^3} \times 100 \quad (7.8)$$

$$= 3.13 \pm 0.01 \text{ wt\%} \quad (7.9)$$

Using the ^{136}Xe enrichment fraction of 90.85%, the number of ^{136}Xe atoms per kiloton of XeLS is calculated as

$$\begin{aligned} N_{^{136}\text{Xe}} &= (1 \text{ kton} \times C_{\text{Xe}} \times 0.9085) \frac{N_A}{M_{\text{Xe}}} \\ &= \frac{3.13 \times 0.9085}{135.80} \times 6.022 \times 10^{23} \\ &= (1.261 \pm 0.004) \times 10^{29} \text{ (kton-XeLS)}^{-1} \end{aligned} \quad (7.10)$$

where N_A is Avogadro's number and M_{Xe} is the average atomic mass of enriched xenon.

7.5.3 Validity of Wilks' Theorem

While the Wilks' theorem-based limit provides a useful reference, it is likely not strictly valid for this analysis. First, the $2\nu\beta\beta^*$ signal rate is bounded from below at zero, violating the regularity conditions required for Wilks' theorem. Second, the observed test statistic profile is non-parabolic near the best-fit point and rises sharply as the signal rate approaches zero. These features indicate that asymptotic χ^2 approximations may not accurately describe the true distribution of the test statistic.

For these reasons, the Wilks' theorem result should be regarded as a preliminary and potentially aggressive estimate. A more reliable confidence interval is obtained using the Feldman–Cousins approach, described in the following section.

7.5.4 Feldman–Cousins Calculation

To obtain a statistically robust upper limit with correct coverage, the Feldman–Cousins (FC) method is employed [72]. Unlike Wilks’ theorem, the FC approach does not rely on asymptotic assumptions and explicitly accounts for physical parameter boundaries. The FC construction is performed by scanning over fixed $2\nu\beta\beta^*$ signal-rate hypotheses in steps of 1 cts/(kt·day). At each signal rate, an ensemble of Toy Monte Carlo datasets is generated using the best-fit background model. Each Toy dataset is fit in the same manner as the real data, and the corresponding test statistic is recorded. For each signal-rate hypothesis, 10,000 Toy MC fits are performed to construct the test statistic distribution, from which the 90% inclusion threshold is determined.

The $\Delta\chi^2$ profile obtained from the real data represents a single realization drawn from these distributions. The 90% C.L. upper limit is defined by the signal rate at which the observed test statistic intersects the FC inclusion threshold. The result of this procedure is shown in Figure 7.3, where the Feldman–Cousins inclusion threshold is observed to be nearly flat as a function of the assumed $2\nu\beta\beta^*$ signal rate. This behavior indicates that the test statistic distribution is dominated by background fluctuations rather than by the signal hypothesis itself, consistent with the background-limited sensitivity of the analysis. The intersection occurs at a signal rate of $R = 56.25$ cts/(kt·day).

At large signal rates, the Feldman–Cousins inclusion threshold approaches $\Delta\chi^2 \simeq 2.8$, close to the Wilks’ theorem expectation of 2.71 for a single parameter. However, the pronounced non-parabolic shape of the data test statistic near the physical boundary at zero signal rate demonstrates the breakdown of asymptotic χ^2 assumptions in this regime, motivating the use of the Feldman–Cousins construction.

Using this approach, the 90% C.L. lower limit on the $2\nu\beta\beta^*$ half-life of ^{136}Xe is

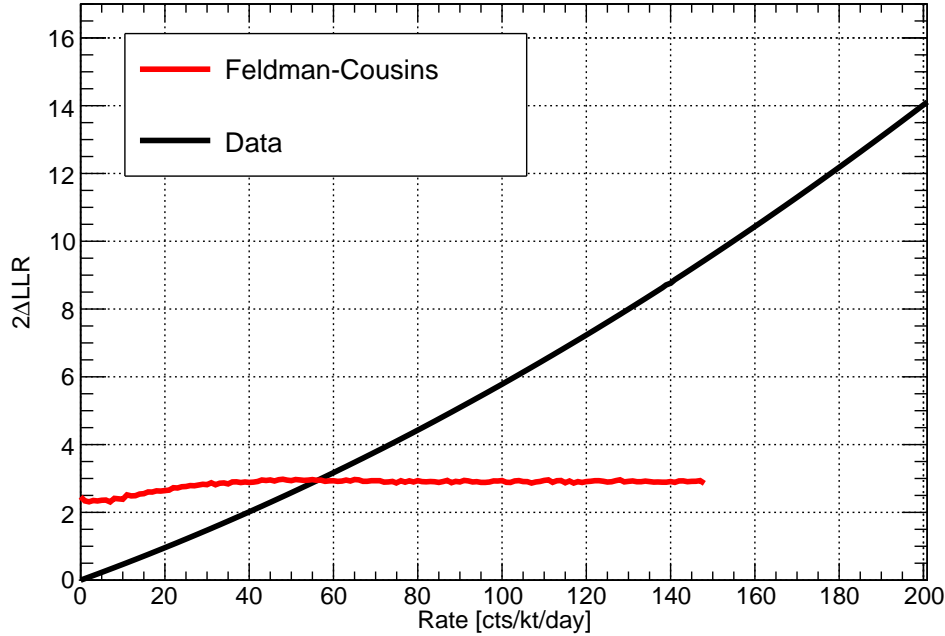


Figure 7.3: Feldman–Cousins analysis results. The black curve shows the test statistic obtained from the data as a function of fixed $2\nu\beta\beta^*$ signal rate. The red curve indicates the 90% Feldman–Cousins inclusion threshold derived from Toy MC ensembles. Their intersection defines the 90% C.L. upper limit.

found to be:

$$T_{1/2} > 4.25 \times 10^{24} \text{ yr} \quad (7.11)$$

As expected, this result is slightly more conservative than the corresponding Wilks' theorem estimate.

7.5.5 Discussion

While preliminary, this analysis establishes a new world-leading limit on the $2\nu\beta\beta^*$ decay of ${}^{136}\text{Xe}$ to the first excited 0_1^+ state. The derived half-life limit of $T_{1/2} > 4.25 \times 10^{24}$ yr exceeds the previous best constraint from EXO-200, $T_{1/2} > 1.4 \times 10^{24}$ yr [44], as well as the earlier KamLAND-Zen 400 result, $T_{1/2} > 8.3 \times 10^{23}$ yr [73]. This improvement is driven primarily by the increased ${}^{136}\text{Xe}$ exposure of the KamLAND-

Zen 800 dataset and the enhanced control of backgrounds achieved through improved detector modeling and statistical treatment.

Figure 7.4 summarizes the current experimental status of the $2\nu\beta\beta^*$ search by comparing the KamLAND-Zen 800 result with previous experimental limits and a representative set of theoretical predictions compiled in Reference [74]. The experimental results are shown as arrows, where the arrow tip indicates the 90% C.L. lower limit on the half-life. The arrow length carries no physical meaning and is used solely to visually indicate that these are lower limits rather than measured values.

The shaded horizontal bands represent predicted half-life ranges from different

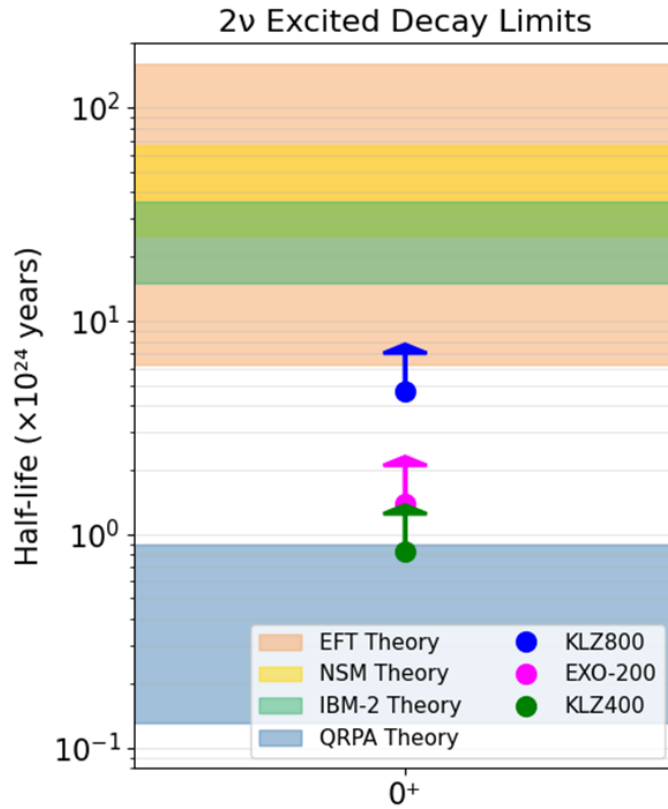


Figure 7.4: A comparison of experimental lower limits on the $2\nu\beta\beta^*$ decay half-life to the 0_1^+ excited state in ^{136}Xe and selected theoretical predictions taken from Reference [74]. The experimental results are shown as arrows, where the arrow tip indicates the 90% C.L. lower limit and the arrow length has no physical meaning.

nuclear-structure approaches, including QRPA, IBM-2, NSM, and EFT-based calculations. The vertical extent of each band reflects the spread of predicted values arising from model assumptions, treatment of nuclear correlations, and uncertainties in nuclear matrix elements. As such, these bands should be interpreted as indicative ranges rather than precise predictions.

The KamLAND-Zen 800 limit lies above the upper edge of the QRPA prediction band, thereby excluding the currently available QRPA calculations for the $2\nu\beta\beta^*$ transition in ^{136}Xe . However, the result remains below the central values of the IBM-2, NSM, and EFT-based predictions, indicating that further sensitivity improvements are required to fully probe the favored parameter space of these models. The progression from KLZ-400 to EXO-200 and now to KLZ-800 illustrates a steady experimental approach toward the predicted half-life region.

It is noteworthy that for several lighter nuclei, measured $2\nu\beta\beta^*$ half-lives have historically been significantly shorter than early theoretical expectations. In this context, the exclusion of a substantial portion of the predicted parameter space represents meaningful progress, even in the absence of a positive observation. Continued improvements in exposure, background reduction, and energy response modeling in future KamLAND-Zen phases may enable direct tests of the remaining theoretical predictions.

Chapter 8

Conclusion

This dissertation presents a preliminary search for the $2\nu\beta\beta^*$ decay of ^{136}Xe using data from the KamLAND-Zen 800 experiment, which employs 745 kg of enriched xenon dissolved in a liquid scintillator calorimeter. Building upon existing KamLAND-Zen 800 analyses, this work focuses on improving the treatment of previously weakly constrained low-energy background components and assessing their impact on the sensitivity to the $2\nu\beta\beta^*$ signal.

In particular, dedicated studies were performed to constrain the rates of ^{11}C produced by cosmic muon spallation and intrinsic ^{40}K contamination in the inner balloon film. These backgrounds contribute in the low-energy region relevant for the excited-state decay search and were previously treated with limited external constraints. By introducing data-driven estimates and incorporating them into the spectral model, this analysis reduces degeneracies among background components and improves the robustness of the subsequent fitting procedure.

A spectral fit to the KamLAND-Zen 800 data was performed in a reduced fiducial volume, and limits on the $2\nu\beta\beta^*$ decay rate were derived using a Feldman–Cousins construction. The resulting 90% confidence level lower limit on the half-life, $T_{1/2} > 4.25 \times 10^{24}$ yr, represents a preliminary but potentially world-leading constraint. However, this limit is obtained under a simplified treatment of detector response and does not yet incorporate the full set of systematic uncertainties associated with energy scale, non-linearity, and spatial response, and should therefore be

interpreted as an optimistic estimate.

Future analyses of the KamLAND-Zen 800 dataset will enable a more comprehensive and robust search for $2\nu\beta\beta^*$ decay. Improved detector response modeling is expected to reduce systematic uncertainties in the energy scale and non-linearity, which directly affect the spectral shape of the dominant ground-state $2\nu\beta\beta$ background. Additionally, resolving residual mismodeling of the radial distribution of backgrounds near and beyond the inner balloon will permit an expansion of the fiducial volume and enhanced rejection of film-originating background events, further improving sensitivity. Future analyses of the KamLAND-Zen 800 dataset will enable a more comprehensive and robust search for $2\nu\beta\beta^*$ decay. Improved detector response modeling is expected to reduce systematic uncertainties in the energy scale and non-linearity, which directly affect the spectral shape of the dominant ground-state $2\nu\beta\beta$ background. In particular, the energy scale can be further constrained using spectral features from long-lived ^{136}Xe spallation isotopes produced by cosmic muons in the xenon-loaded scintillator. These isotopes provide internally generated calibration handles that are spatially distributed throughout the XeLS volume and span the full duration of KamLAND-Zen 800 data-taking.

Tagged spallation events are identified using a likelihood-based selection that exploits correlations between candidate decays and the parent muon track, including the time since the muon (ΔT), distance to associated neutron captures (dR), and the effective number of neutrons (ENN). This discriminator enables the isolation of specific xenon spallation products whose decay spectra exhibit distinctive peak or edge features. By extracting these features in data and comparing them to Monte Carlo expectations, the detector energy scale and its time dependence can be constrained independently of traditional calibration sources.

Because these spallation-derived calibration points populate the same energy re-

gion relevant for the $2\nu\beta\beta^*$ search and are present continuously throughout the data-taking period, they provide a powerful means of validating and correcting residual mismodeling of the energy response. Incorporating this information into future analyses is expected to significantly reduce systematic distortions in the background model and improve sensitivity to excited-state double beta decay.

In addition to improvements in detector calibration and background modeling, machine learning techniques provide a powerful and complementary approach to enhancing sensitivity to $2\nu\beta\beta^*$ decays. The KamNet framework, a spatiotemporal deep neural network developed specifically for KamLAND-Zen, has demonstrated strong discrimination power between single-site energy depositions and closely spaced multivertex events using low-level PMT hit timing and spatial information [75]. This distinction is particularly relevant for excited-state double-beta decays, which are characterized by prompt γ cascades following the primary $\beta\beta$ transition and therefore produce multiple, spatially separated energy deposits in the liquid scintillator.

KamNet exploits the spherical symmetry of the detector geometry through spherical convolutional layers, while simultaneously modeling the time structure of scintillation light using a convolutional LSTM with an attention mechanism. This architecture enables the network to focus on specific regions of the scintillation time profile that carry the most discriminating information. In the case of excited-state decays, KamNet assigns increased attention to time slices associated with delayed energy depositions from γ interactions, effectively separating these events from the dominant ground-state $2\nu\beta\beta$ background, which is largely single-site and isotropic.

Using detailed Monte Carlo simulations, KamNet has been shown to improve the signal-to-background ratio for ^{136}Xe excited-state decays by approximately 70% relative to a traditional energy-only analysis, corresponding to a substantial gain in experimental sensitivity. Importantly, this improvement is achieved without intro-

ducing additional coincidence requirements or hardware upgrades, and the network's attention mechanism provides a degree of interpretability by revealing which temporal and spatial features drive the classification. These results demonstrate that machine learning approaches such as KamNet are well suited for excited-state double-beta decay searches and represent a promising avenue for future analyses of the KamLAND-Zen 800 dataset.

Bibliography

- [1] W. Pauli. Dear radioactive ladies and gentlemen. *Phys. Today*, 31N9:27, 1978.
- [2] C. L. Cowan, F. Reines, F. B. Harrison, H. W. Kruse, and A. D. McGuire. Detection of the Free Neutrino: a Confirmation. *Science*, 124(3212):103–104, 1956.
- [3] Sheldon L. Glashow. Partial-symmetries of weak interactions. *Nuclear Physics*, 22(4):579–588, 1961.
- [4] Abdus Salam. Elementary particle theory: Relativistic groups and analyticity. In Nils Svartholm, editor, *Elementary Particle Theory: Relativistic Groups and Analyticity (Nobel Symposium No. 8)*, page 367. Almqvist and Wiksell, Stockholm, 1968.
- [5] Steven Weinberg. A Model of Leptons. *Phys. Rev. Lett.*, 19:1264–1266, 1967.
- [6] Gerard 't Hooft and M. J. G. Veltman. Regularization and Renormalization of Gauge Fields. *Nucl. Phys. B*, 44:189–213, 1972.
- [7] Gerard 't Hooft. Renormalization of Massless Yang-Mills Fields. *Nucl. Phys. B*, 33:173–199, 1971.
- [8] M. Grunewald et al. Precision electroweak measurements on the Z resonance. *Physics Reports*, 427(5):257–454, 2006.
- [9] NobelPrize.org. The Nobel Prize in Physics 2015. <https://www.nobelprize.org/prizes/physics/2015/summary/>. Accessed: 2025-01-24.
- [10] B. Pontecorvo. Mesonium and anti-mesonium. *Soviet Journal of Experimental and Theoretical Physics*, 6:429, 1957.
- [11] Ivan Esteban, M. C. Gonzalez-Garcia, Michele Maltoni, Ivan Martinez-Soler, João Paulo Pinheiro, and Thomas Schwetz. NuFit-6.0: Updated Global Analysis of Three-Flavor Neutrino Oscillations. *Journal of High Energy Physics*, 2024(12), 2024.
- [12] Alessandro Paoloni. Status of the JUNO experiment. *Proceeding of Science*, HQL2023:017, 2024.

- [13] Ali Ajmi. Status of the Hyper-Kamiokande Experiment. *Proceeding of Science*, HQL2023:098, 2024.
- [14] Inés Gil-Botella. The Deep Underground Neutrino Experiment (DUNE) Program. *Proceeding of Science*, ICHEP2024:165, 2025.
- [15] M. Aker et al. Direct Neutrino-Mass Measurement With Sub-Electron Volt Sensitivity. *Nature Physics*, 18(2):160–166, 2022.
- [16] A. Ashtari Esfahani, S. Böser, N. Buzinsky, M. C. Carmona-Benitez, C. Claessens, L. de Viveiros, P. J. Doe, M. Fertl, J. A. Formaggio, J. K. Gaisson, L. Gladstone, M. Grando, M. Guigue, J. Hartse, K. M. Heeger, X. Huyan, J. Johnston, A. M. Jones, K. Kazkaz, B. H. LaRoque, M. Li, A. Lindman, E. Machado, A. Marsteller, C. Matthé, R. Mohiuddin, B. Monreal, R. Mueller, J. A. Nikkel, E. Novitski, N. S. Oblath, J. I. Peña, W. Pettus, R. Reimann, R. G. H. Robertson, D. Rosa De Jesús, G. Rybka, L. Saldaña, M. Schram, P. L. Slocum, J. Stachurska, Y.-H. Sun, P. T. Surukuchi, J. R. Tedeschi, A. B. Telles, F. Thomas, M. Thomas, L. A. Thorne, T. Thümmler, L. Tvrznikova, W. Van De Pontseele, B. A. VanDevender, J. Weinroub, T. E. Weiss, T. Wendler, A. Young, E. Zayas, and A. Ziegler. Tritium Beta Spectrum Measurement and Neutrino Mass Limit from Cyclotron Radiation Emission Spectroscopy. *Physical Review Letters*, 131:102502, Sep 2023.
- [17] Eleonora Di Valentino, Stefano Gariazzo, and Olga Mena. Most constraining cosmological neutrino mass bounds. *Physical Review D*, 104:083504, Oct 2021.
- [18] Carlo Giunti and Chung W. Kim. *Fundamentals of Neutrino Physics and Astrophysics*. Oxford University Press, 03 2007.
- [19] Sacha Davidson, Enrico Nardi, and Yosef Nir. Leptogenesis. *Physics Reports*, 466(4–5):105–177, September 2008.
- [20] Wayne Hu and Scott Dodelson. Cosmic microwave background anisotropies. *Annual Review of Astronomy and Astrophysics*, 40(1):171–216, September 2002.
- [21] M. Abdul Karim, J. Aguilar, S. Ahlen, S. Alam, L. Allen, C. Allende Prieto, O. Alves, A. Anand, U. Andrade, E. Armengaud, A. Aviles, S. Bailey, C. Baltay, P. Bansal, A. Bault, J. Behera, S. BenZvi, D. Bianchi, C. Blake, S. Brieden, A. Brodzeller, D. Brooks, E. Buckley-Geer, E. Burtin, R. Calderon, R. Canning, A. Carnero Rosell, P. Carrilho, L. Casas, F.J. Castander, M. Charles, E. Chausson, J. Chaves-Montero, D. Chebat, X. Chen, T. Claybaugh, S. Cole, A.P. Cooper, A. Cuceu, K.S. Dawson, A. de la Macorra, A. de Mattia, N. Deiosso, J. Della Costa, R. Demina, A. Dey, B. Dey, Z. Ding, P. Doel, J. Edelstein, D.J. Eisenstein, W. Elbers, P. Fagrelius, K. Fanning, E. Fernández-García, S. Ferraro, A. Font-Ribera, J.E. Forero-Romero, C.S. Frenk, C. Garcia-Quintero,

- L.H. Garrison, E. Gaztañaga, H. Gil-Marín, S. Gontcho A. Gontcho, D. Gonzalez, A.X. Gonzalez-Morales, C. Gordon, D. Green, G. Gutierrez, J. Guy, B. Hadzhiyska, C. Hahn, S. He, M. Herbold, H.K. Herrera-Alcantar, M.-F. Ho, K. Honscheid, C. Howlett, D. Huterer, M. Ishak, S. Juneau, N.V. Kamble, N.G. Karaçayl, R. Kehoe, S. Kent, A.G. Kim, D. Kirkby, T. Kisner, S.E. Koposov, A. Kremin, A. Krolewski, O. Lahav, C. Lamman, M. Landriau, D. Lang, J. Lasker, J.M. Le Goff, L. Le Guillou, A. Leauthaud, M.E. Levi, Q. Li, T.S. Li, K. Lodha, M. Lokken, F. Lozano-Rodríguez, C. Magneville, M. Manera, P. Martini, W.L. Matthewson, A. Meisner, J. Mena-Fernández, A. Menegas, T. Mergulhão, R. Miquel, J. Moustakas, A. Muñoz-Gutiérrez, D. Muñoz-Santos, A.D. Myers, S. Nadathur, K. Naidoo, L. Napolitano, J.A. Newman, G. Niz, H.E. Noriega, E. Paillas, N. Palanque-Delabrouille, J. Pan, J.A. Peacock, M.P. Ibanez, W.J. Percival, A. Pérez-Fernández, I. Pérez-Ràfols, M.M. Pieri, C. Poppett, F. Prada, D. Rabinowitz, A. Raichoor, C. Ramírez-Pérez, M. Rashkovetskyi, C. Ravoux, J. Rich, A. Rocher, C. Rockosi, J. Rohlf, J.O. Román-Herrera, A.J. Ross, G. Rossi, R. Ruggeri, V. Ruhlmann-Kleider, L. Samushia, E. Sanchez, N. Sanders, D. Schlegel, M. Schubnell, H. Seo, A. Shafieloo, R. Sharples, J. Silber, F. Sinigaglia, D. Sprayberry, T. Tan, G. Tarlé, P. Taylor, W. Turner, L.A. Ureña-López, R. Vaisakh, F. Valdes, G. Valogiannis, M. Vargas-Magaña, L. Verde, M. Walther, B.A. Weaver, D.H. Weinberg, M. White, M. Wolfson, C. Yèche, J. Yu, E.A. Zaborowski, P. Zarrouk, Z. Zhai, H. Zhang, C. Zhao, G.B. Zhao, R. Zhou, and H. Zou. DESI DR2 results. II. Measurements of baryon acoustic oscillations and cosmological constraints. *Physical Review D*, 112(8), October 2025.
- [22] M. Goeppert-Mayer. Double Beta-Disintegration. *Physical Review*, 48:512–516, Sep 1935.
- [23] J. J. Gomez-Cadenas, J. Martin-Albo, M. Mezzetto, F. Monrabal, and M. Sorel. The Search for neutrinoless double beta decay. *Riv. Nuovo Cim.*, 35(2):29–98, 2012.
- [24] J. Kotila and F. Iachello. Phase-space factors for double- β decay. *Physical Review C*, 85:034316, Mar 2012.
- [25] Mihai Horoi and Andrei Neacsu. Shell Model Study of Using an Effective Field Theory for Disentangling Several Contributions to Neutrinoless Double- β Decay. *Physical Review C*, 98:035502, Sep 2018.
- [26] B. Pritychenko and V.I. Tretyak. Comprehensive Review of 2β decay half-lives. *Atomic Data and Nuclear Data Tables*, 161:101694, 2025.
- [27] Jouni Suhonen and Joel Kostensalo. Double β Decay and the Axial Strength. *Frontiers in Physics*, 7, 2019.

- [28] W. H. Furry. On Transition Probabilities in Double Beta-Disintegration. *Physical Review*, 56(12):1184, 12 1939.
- [29] J. Schechter and J. W. F. Valle. Neutrinoless double- β decay in $SU(2) \times U(1)$ theories. *Phys. Rev. D*, 25:2951–2954, Jun 1982.
- [30] Michael Duerr, Manfred Lindner, and Alexander Merle. On the Quantitative Impact of the Schechter-Valle Theorem. *JHEP*, 06:091, 2011.
- [31] Lukáš Gráf, Sudip Jana, Oliver Scholer, and Nele Volmer. Neutrinoless double beta decay without vacuum Majorana neutrino mass. *Physics Letters B*, 859:139111, 2024.
- [32] M. Agostini, G. R. Araujo, A. M. Bakalyarov, M. Balata, I. Barabanov, L. Baudis, C. Bauer, E. Bellotti, S. Belogurov, A. Bettini, L. Bezrukov, V. Biancacci, D. Borowicz, E. Bossio, V. Bothe, V. Brudanin, R. Brugnera, A. Caldwell, C. Cattadori, A. Chernogorov, T. Comellato, V. D’Andrea, E. V. Demidova, N. Di Marco, E. Doroshkevich, F. Fischer, M. Fomina, A. Gangapshev, A. Garfagnini, C. Gooch, P. Grabmayr, V. Gurentsov, K. Gusev, J. Hakenmüller, S. Hemmer, R. Hiller, W. Hofmann, J. Huang, M. Hult, L. V. Inzhechik, J. Janicskó Csáthy, J. Jochum, M. Junker, V. Kazalov, Y. Kermaïdic, H. Khushbakht, T. Kihm, I. V. Kirpichnikov, A. Klimenko, R. Kneißl, K. T. Knöpfle, O. Kochetov, V. N. Kornoukhov, P. Krause, V. V. Kuzminov, M. Laubenstein, A. Lazzaro, M. Lindner, I. Lippi, A. Lubashevskiy, B. Lubsandorzhev, G. Lutter, C. Macolino, B. Majorovits, W. Maneschg, L. Manzanillas, M. Miloradovic, R. Mingazheva, M. Misiaszek, P. Moseev, Y. Müller, I. Nemchenok, K. Panas, L. Pandola, K. Pelczar, L. Pertoldi, P. Piseri, A. Pullia, C. Ransom, L. Rauscher, S. Riboldi, N. Rumyantseva, C. Sada, F. Salamida, S. Schönert, J. Schreiner, M. Schütt, A.-K. Schütz, O. Schulz, M. Schwarz, B. Schwingenheuer, O. Selivanenko, E. Shevchik, M. Shirchenko, L. Shtembari, H. Simgen, A. Smolnikov, D. Stukov, A. A. Vasenko, A. Veresnikova, C. Vignoli, K. von Sturm, T. Wester, C. Wiesinger, M. Wojcik, E. Yanovich, B. Zatschler, I. Zhitnikov, S. V. Zhukov, D. Zinatulina, A. Zschocke, A. J. Zsigmond, K. Zuber, and G. Zuzel. Final Results of GERDA on the Search for Neutrinoless Double- β Decay. *Physical Review Letters*, 125:252502, Dec 2020.
- [33] E. Armengaud, C. Augier, A. S. Barabash, F. Bellini, G. Benato, A. Benoît, M. Beretta, L. Bergé, J. Billard, Yu. A. Borovlev, Ch. Bourgeois, V. B. Brudanin, P. Camus, L. Cardani, N. Casali, A. Cazes, M. Chapellier, F. Charlieux, D. Chiesa, M. de Combarieu, I. Dafinei, F. A. Danevich, M. De Jesus, T. Dixon, L. Dumoulin, K. Eitel, F. Ferri, B. K. Fujikawa, J. Gascon, L. Gironi, A. Giuliani, V. D. Grigorieva, M. Gros, E. Guerard, D. L. Helis, H. Z. Huang, R. Huang, J. Johnston, A. Juillard, H. Khalife, M. Kleifges, V. V. Kobylev, Yu. G. Kolomensky, S. I. Konovalov, A. Leder, P. Loaiza, L. Ma, E. P. Makarov,

- P. de Marcillac, R. Mariam, L. Marini, S. Marnieros, D. Misiak, X.-F. Navick, C. Nones, E. B. Norman, V. Novati, E. Olivieri, J. L. Ouellet, L. Pagnanini, P. Pari, L. Pattavina, B. Paul, M. Pavan, H. Peng, G. Pessina, S. Pirro, D. V. Poda, O. G. Polischuk, S. Pozzi, E. Previtali, Th. Redon, A. Rojas, S. Rozov, C. Rusconi, V. Sanglard, J. A. Scarpaci, K. Schäffner, B. Schmidt, Y. Shen, V. N. Shlegel, B. Siebenborn, V. Singh, C. Tomei, V. I. Tretyak, V. I. Umatov, L. Vagneron, M. Velázquez, B. Welliver, L. Winslow, M. Xue, E. Yakushev, M. Zarytskyy, and A. S. Zolotarova. New Limit for Neutrinoless Double-Beta Decay of ^{100}Mo from the CUPID-Mo Experiment. *Physical Review Letters*, 126:181802, May 2021.
- [34] D. Q. Adams, C. Alduino, K. Alfonso, F. T. Avignone, O. Azzolini, G. Bari, F. Bellini, G. Benato, M. Beretta, M. Biassoni, A. Branca, C. Brofferio, C. Bucci, J. Camilleri, A. Caminata, A. Campani, L. Canonica, X. G. Cao, S. Capelli, C. Capelli, L. Cappelli, L. Cardani, P. Carniti, N. Casali, E. Celi, D. Chiesa, M. Clemenza, S. Copello, O. Cremonesi, R. J. Creswick, A. D'Addabbo, I. Dafinei, F. Del Corso, S. Dell'Oro, S. Di Domizio, S. Di Lorenzo, V. Dompè, D. Q. Fang, G. Fantini, M. Faverzani, E. Ferri, F. Ferroni, E. Fiorini, M. A. Franceschi, S. J. Freedman, S. H. Fu, B. K. Fujikawa, S. Ghislandi, A. Giachero, A. Gianvecchio, L. Gironi, A. Giuliani, P. Gorla, C. Gotti, T. D. Gutierrez, K. Han, E. V. Hansen, K. M. Heeger, R. G. Huang, H. Z. Huang, J. Johnston, G. Keppel, Yu. G. Kolomensky, R. Kowalski, R. Liu, L. Ma, Y. G. Ma, L. Marini, R. H. Maruyama, D. Mayer, Y. Mei, S. Morganti, T. Napolitano, M. Nastasi, J. Nikkel, C. Nones, E. B. Norman, A. Nucciotti, I. Nutini, T. O'Donnell, M. Olmi, J. L. Ouellet, S. Pagan, C. E. Pagliarone, L. Pagnanini, M. Pallavicini, L. Pattavina, M. Pavan, G. Pessina, V. Pettinacci, C. Pira, S. Pirro, S. Pozzi, E. Previtali, A. Puiu, S. Quitadamo, A. Ressa, C. Rosenfeld, S. Sangiorgio, B. Schmidt, N. D. Scielzo, V. Sharma, V. Singh, M. Sisti, D. Speller, P. T. Surukuchi, L. Taffarello, F. Terranova, C. Tomei, K. J. Vetter, M. Vignati, S. L. Wagaarachchi, B. S. Wang, B. Welliver, J. Wilson, K. Wilson, L. A. Winslow, S. Zimmermann, and S. Zucchelli. New Direct Limit on Neutrinoless Double Beta Decay Half-Life of ^{128}Te with CUORE. *Physical Review Letters*, 129:222501, Nov 2022.
- [35] D. Gooding. *Enhancing the Neutrinoless Double Beta Decay Sensitivity of SNO+ with Deep Learning*. PhD thesis, Boston University, 2025.
- [36] Jonathan Engel and Javier Menéndez. Status and Future of Nuclear Matrix Elements for Neutrinoless Double-Beta Decay: A Review. *Reports on Progress in Physics*, 80(4):046301, Mar 2017.
- [37] A. Belley, C. G. Payne, S. R. Stroberg, T. Miyagi, and J. D. Holt. Ab Initio Neutrinoless Double-Beta Decay Matrix Elements for ^{48}Ca , ^{76}Ge , and ^{82}Se . *Physical Review Letters*, 126:042502, Jan 2021.

- [38] M. Horoi, A. Neacsu, and S. Stoica. Statistical analysis for the neutrinoless double- β -decay matrix element of ^{48}Ca . *Phys. Rev. C*, 106:054302, Nov 2022.
- [39] L. Jokiniemi, B. Romeo, C. Brase, J. Kotila, P. Soriano, A. Schwenk, and J. Menéndez. Two-neutrino $\beta\beta$ decay of ^{136}Xe to the first excited 0^+ state in ^{136}Ba . *Physics Letters B*, 838:137689, 2023.
- [40] Lotta Jokiniemi, Beatriz Romeo, Pablo Soriano, and Javier Menéndez. Neutrinoless $\beta\beta$ -decay nuclear matrix elements from two-neutrino $\beta\beta$ -decay data. *Phys. Rev. C*, 107:044305, Apr 2023.
- [41] Lotta Jokiniemi, Beatriz Romeo, Pablo Soriano, and Javier Menéndez. Neutrinoless $\beta\beta$ -decay nuclear matrix elements from two-neutrino $\beta\beta$ -decay data. *Phys. Rev. C*, 107(4):044305, 2023.
- [42] Daniel Castillo, Lotta Jokiniemi, Pablo Soriano, and Javier Menéndez. Neutrinoless $\beta\beta$ decay nuclear matrix elements complete up to N2LO in heavy nuclei. *Physics Letters B*, 860:139181, 2025.
- [43] S. Abe, T. Araki, K. Chiba, T. Eda, M. Eizuka, Y. Funahashi, A. Furuto, A. Gando, Y. Gando, S. Goto, T. Hachiya, K. Hata, K. Ichimura, S. Ieki, H. Ikeda, K. Inoue, K. Ishidoshiro, Y. Kamei, N. Kawada, Y. Kishimoto, M. Koga, A. Marthe, Y. Matsumoto, T. Mitsui, H. Miyake, D. Morita, R. Nakajima, K. Nakamura, R. Nakamura, R. Nakamura, J. Nakane, T. Ono, H. Ozaki, K. Saito, T. Sakai, I. Shimizu, J. Shirai, K. Shiraishi, A. Suzuki, K. Tachibana, K. Tamae, H. Watanabe, K. Watanabe, S. Yoshida, S. Umehara, K. Fushimi, K. Kotera, Y. Urano, B. E. Berger, B. K. Fujikawa, J. G. Learned, J. Marićic, Z. Fu, S. Ghosh, J. Smolsky, L. A. Winslow, Y. Efremenko, H. J. Karwowski, D. M. Markoff, W. Tornow, S. Dell’Oro, T. O’Donnell, J. A. Detwiler, S. Enomoto, M. P. Decowski, K. M. Weerman, C. Grant, Ö. Penek, H. Song, A. Li, S. N. Axani, M. Garcia, and M. Sarfraz. Search for Majorana Neutrinos with the Complete KamLAND-Zen Dataset. *Phys. Rev. Lett.*, 135:262501, Dec 2025.
- [44] S. Al Kharusi, G. Anton, I. Badhrees, P.S. Barbeau, D. Beck, V. Belov, T. Bhatta, M. Breidenbach, T. Brunner, G.F. Cao, W.R. Cen, C. Chambers, B. Cleveland, M. Coon, A. Craycraft, T. Daniels, L. Darroch, S.J. Daugherty, J. Davis, S. Delaquis, A. Der Mesrobian-Kabakian, R. DeVoe, J. Dilling, A. Dolgolenko, M.J. Dolinski, J. Echevers, W. Fairbank Jr., D. Fairbank, J. Farine, S. Feyzbakhsh, P. Fierlinger, Y.S. Fu, D. Fudenberg, P. Gautam, R. Gornea, G. Gratta, C. Hall, E.V. Hansen, J. Hoessl, P. Hufschmidt, M. Hughes, A. Iverson, A. Jamil, C. Jessiman, M.J. Jewell, A. Johnson, A. Karelina, L.J. Kaufman, T. Koffas, R. Krücke, A. Kuchenkov, K.S. Kumar, Y. Lan, A. Larson, B.G.

- Lenardo, D.S. Leonard, G.S. Li, S. Li, Z. Li, C. Licciardi, Y.H. Lin, R. MacLellan, T. McElroy, T. Michel, B. Mong, D.C. Moore, K. Murray, O. Njoya, O. Nu-sair, A. Odian, I. Ostrovskiy, A. Perna, A. Piepke, A. Pocar, F. Retière, A.L. Robinson, P.C. Rowson, J. Runge, S. Schmidt, D. Sinclair, K. Skarpaas, A.K. Soma, V. Stekhanov, M. Tarka, S. Thibado, J. Todd, T. Tolba, T.I. Totev, R. Tsang, B. Veenstra, V. Veeraraghavan, P. Vogel, J.-L. Vuilleumier, M. Wagenpfeil, J. Watkins, M. Weber, L.J. Wen, U. Wichoski, G. Wrede, S.X. Wu, Q. Xia, D.R. Yahne, L. Yang, Y.-R. Yen, O.Ya. Zeldovich, T. Ziegler, and (EXO-200 Collaboration) . Search for two-neutrino double-beta decay of ^{136}Xe to the 0_1^+ excited state of ^{136}Ba with the complete EXO-200 dataset. *Chinese Physics C*, 47(10):103001, oct 2023.
- [45] H. Ozaki. *High Sensitivity Search for Neutrinoless Double-Beta Decay in KamLAND-Zen with Double Amount of ^{136}Xe* . PhD thesis, Tohoku University, 2019.
 - [46] S. Matsuda. *Search for Neutrinoless Double-Beta Decay in ^{136}Xe after Intensive Background Reduction with KamLAND-Zen*. PhD thesis, Tohoku University, 2016.
 - [47] H. Miyake. *Search for Neutrinoless Double-Beta Decay in KamLAND-Zen Applying Improved Long-Lived Spallation Background Reduction*. PhD thesis, Tohoku University, 2023.
 - [48] A. Gando. *First Results of Neutrinoless Double Beta Decay Search with KamLAND-Zen*. PhD thesis, Tohoku University, 2012.
 - [49] A. Li. *The Tao and Zen of neutrinos: neutrinoless double beta decay in KamLAND-ZEN 800*. PhD thesis, Boston University, 2020.
 - [50] H. Yoshida. *Limit on Majorana Neutrino Mass with Neutrinoless Double Beta Decay from KamLAND-Zen*. PhD thesis, Tohoku University, 2014.
 - [51] Y. Karino. *Improvement of Background Rejection for Cosmic Muon Spallation in KamLAND-Zen*. PhD thesis, Tohoku University, 2017.
 - [52] A. Takeuchi. *First Search for Majorana Neutrinos in the Inverted Mass Hierarchy Region with KamLAND-Zen*. PhD thesis, Tohoku University, 2023.
 - [53] T. Hachiya. e^+/e^- Discrimination in KamLAND. *Proceedings of the 10th International Workshop on Neutrino-Nucleus Interactions in Few-GeV Region (NuInt15)*, 2016.
 - [54] S. Agostinelli, J. Allison, K. Amako, J. Apostolakis, H. Araujo, P. Arce, M. Asai, D. Axen, S. Banerjee, G. Barrand, F. Behner, L. Bellagamba, J. Boudreau,

- L. Broglia, A. Brunengo, H. Burkhardt, S. Chauvie, J. Chuma, R. Chytracek, G. Cooperman, G. Cosmo, P. Degtyarenko, A. Dell'Acqua, G. Depaola, D. Dietrich, R. Enami, A. Feliciello, C. Ferguson, H. Fesefeldt, G. Folger, F. Foppiano, A. Forti, S. Garelli, S. Giani, R. Giannitrapani, D. Gibin, J.J. Gómez Cadenas, I. González, G. Gracia Abril, G. Greeniaus, W. Greiner, V. Grichine, A. Grossheim, S. Guatelli, P. Gumplinger, R. Hamatsu, K. Hashimoto, H. Hasui, A. Heikkinen, A. Howard, V. Ivanchenko, A. Johnson, F.W. Jones, J. Kallenbach, N. Kanaya, M. Kawabata, Y. Kawabata, M. Kawaguti, S. Kelner, P. Kent, A. Kimura, T. Kodama, R. Kokoulin, M. Kossov, H. Kurashige, E. Lamanna, T. Lampén, V. Lara, V. Lefebure, F. Lei, M. Liendl, W. Lockman, F. Longo, S. Magni, M. Maire, E. Medernach, K. Minamimoto, P. Mora de Freitas, Y. Morita, K. Murakami, M. Nagamatu, R. Nartallo, P. Nieminen, T. Nishimura, K. Ohtsubo, M. Okamura, S. O'Neale, Y. Oohata, K. Paech, J. Perl, A. Pfeiffer, M.G. Pia, F. Ranjard, A. Rybin, S. Sadilov, E. Di Salvo, G. Santin, T. Sasaki, N. Savvas, Y. Sawada, S. Scherer, S. Sei, V. Sirotenko, D. Smith, N. Starkov, H. Stoecker, J. Sulkimo, M. Takahata, S. Tanaka, E. Tcherniaev, E. Safai Tehrani, M. Tropeano, P. Truscott, H. Uno, L. Urban, P. Urban, M. Verderi, A. Walkden, W. Wander, H. Weber, J.P. Wellisch, T. Wenaus, D.C. Williams, D. Wright, T. Yamada, H. Yoshida, and D. Zschiesche. Geant4—a simulation toolkit. *Nuclear Instruments and Methods in Physics Research Section A: Accelerators, Spectrometers, Detectors and Associated Equipment*, 506(3):250–303, 2003.
- [55] FLUKA. <https://fluka.cern>. Accessed: 2025-12-31.
- [56] C. Ahdida, D. Bozzato, D. Calzolari, F. Cerutti, N. Charitonidis, A. Cimmino, A. Coronetti, G. L. D'Alessandro, A. Donadon Servelle, L. S. Esposito, R. Froeschl, R. García Alía, A. Gerbershagen, S. Gilardoni, D. Horváth, G. Hugo, A. Infantino, V. Kouskoura, A. Lechner, B. Lefebvre, G. Lerner, M. Magistris, A. Manousos, G. Moryc, F. Ogallar Ruiz, F. Pozzi, D. Prelipcean, S. Roesler, R. Rossi, M. Sabaté Gilarte, F. Salvat Pujol, P. Schoofs, V. Stránský, C. Theis, A. Tsinganis, R. Versaci, V. Vlachoudis, A. Waets, and M. Widorski. New Capabilities of the FLUKA Multi-Purpose Code. *Frontiers in Physics*, Volume 9 - 2021, 2022.
- [57] Giuseppe Battistoni et al. Overview of the FLUKA code. *Annals Nucl. Energy*, 82:10–18, 2015.
- [58] Hugo, Gabrielle, Ahdida, Claudia, Bozzato, Davide, Calzolari, Daniele, Cerutti, Francesco, Ciccotelli, Alessia, Cimmino, Anna, Devienne, Arnaud, Donadon Servelle, Andre, Dyracz, Patrycja K., Salvatore Esposito, Luigi, Formento, Alice, Froeschl, Robert, García Alía, Ruben, Gilardoni, Simone, Gomes, Andrea, Horváth, Dávid, Humann, Barbara, Infantino, Angelo, Lechner, Anton, Lefebvre,

- Benoit, Lerner, Giuseppe, Lorenzon, Tommaso, Luchsanyi, David, Magistris, Matteo, Marin, Stefano, Mazzola, Giuseppe, Niang, Samuel, Nowak, Elzbieta, Ogalalor Ruiz, Francisco, Potoine, Jean-Baptiste, Pozzi, Fabio, Prelipcean, Daniel, Rodin, Volodymyr, Roesler, Stefan, Sabaté Gilarte, Marta, Sacristan Barbero, Mario, Salvat Pujol, Francesc, Schoofs, Philippe, Šerban, Alexandra-Gabriela, Sharankov, Ivan, Theis, Chris, Tisi, Marco, Tsinganis, Andrea, Versaci, Roberto, Vlachoudis, Vasilis, Waets, Andreas, Widorski, Markus, and Zymak, Illia. Latest FLUKA developments. *EPJ Nuclear Sci. Technol.*, 10:20, 2024.
- [59] S. Abe, S. Asami, M. Eizuka, S. Futagi, A. Gando, Y. Gando, T. Gima, A. Goto, T. Hachiya, K. Hata, K. Hosokawa, K. Ichimura, S. Ieki, H. Ikeda, K. Inoue, K. Ishidoshiro, Y. Kamei, N. Kawada, Y. Kishimoto, M. Koga, M. Kurashawa, T. Mitsui, H. Miyake, T. Nakahata, K. Nakamura, R. Nakamura, H. Ozaki, T. Sakai, I. Shimizu, J. Shirai, K. Shiraishi, A. Suzuki, Y. Suzuki, A. Takeuchi, K. Tamae, H. Watanabe, Y. Yoshida, S. Obara, A. K. Ichikawa, S. Yoshida, S. Umehara, K. Fushimi, K. Kotera, Y. Urano, B. E. Berger, B. K. Fujikawa, J. G. Learned, J. Maricic, S. N. Axani, Z. Fu, J. Smolsky, L. A. Winslow, Y. Efremenko, H. J. Karwowski, D. M. Markoff, W. Tornow, S. Dell’Oro, T. O’Donnell, J. A. Detwiler, S. Enomoto, M. P. Decowski, K. M. Weerman, C. Grant, A. Li, and H. Song. Measurement of cosmic-ray muon spallation products in a xenon-loaded liquid scintillator with KamLAND. *Phys. Rev. C*, 107:054612, May 2023.
- [60] S. Abe, S. Enomoto, K. Furuno, Y. Gando, H. Ikeda, K. Inoue, Y. Kibe, Y. Kishimoto, M. Koga, Y. Minekawa, T. Mitsui, K. Nakajima, K. Nakajima, K. Nakamura, M. Nakamura, I. Shimizu, Y. Shimizu, J. Shirai, F. Suekane, A. Suzuki, Y. Takemoto, K. Tamae, A. Terashima, H. Watanabe, E. Yonezawa, S. Yoshida, A. Kozlov, H. Murayama, J. Busenitz, T. Classen, C. Grant, G. Keefer, D. S. Leonard, D. McKee, A. Piepke, T. I. Banks, T. Bloxham, J. A. Detwiler, S. J. Freedman, B. K. Fujikawa, F. Gray, E. Guardincerri, L. Hsu, K. Ichimura, R. Kadel, C. Lendvai, K. B. Luk, T. O’Donnell, H. M. Steiner, L. A. Winslow, D. A. Dwyer, C. Jillings, C. Mauger, R. D. McKeown, P. Vogel, C. Zhang, B. E. Berger, C. E. Lane, J. Maricic, T. Miletic, M. Batygov, J. G. Learned, S. Matsuno, S. Pakvasa, J. Foster, G. A. Horton-Smith, A. Tang, S. Dazeley, K. E. Downum, G. Gratta, K. Tolich, W. Bugg, Y. Efremenko, Y. Kamyshev, O. Perevozchikov, H. J. Karwowski, D. M. Markoff, W. Tornow, K. M. Heeger, F. Piquemal, J. S. Ricol, and M. P. Decowski. Production of radioactive isotopes through cosmic muon spallation in KamLAND. *Phys. Rev. C*, 81:025807, Feb 2010.
- [61] P. Antonioli, C. Ghetti, E.V. Korolkova, V.A. Kudryavtsev, and G. Sartorelli. A three-dimensional code for muon propagation through the rock: MUSIC. *Astroparticle Physics*, 7(4):357–368, 1997.

- [62] Y. Kamei. *Hunting Massive Majoron Emission in Neutrinoless Double-Beta Decay of ^{136}Xe with KamLAND-Zen*. PhD thesis, Tohoku University, 2021.
- [63] Brookhaven National Laboratory National Nuclear Data Center. Evaluated Nuclear Structure Data File (ENSDF). webpage.
- [64] A. Gando et al. Search for double-beta decay of ^{134}Xe . *Phys. Rev. C*, 93:045501, 2016.
- [65] E665 Collaboration, M.R. Adams, M. Aderholz, and et al. Production of charged hadrons by positive muons on deuterium and xenon at 490 GeV. *Z. Phys. C – Particles and Fields*, 61:179–198, 1994.
- [66] L. Giot, J.A. Alcántara-Núñez, J. Benlliure, D. Pérez-Loureiro, L. Audouin, A. Boudard, E. Casarejos, T. Enqvist, J.E. Ducret, B. Fernández-Domínguez, M. Fernández Ordóñez, F. Farget, A. Heinz, V. Henzl, D. Henzlova, A. Kelić-Heil, A. Lafriaskh, S. Leray, P. Napolitani, C. Paradela, J. Pereira, M.V. Ricciardi, C. Stéphan, K.-H. Schmidt, C. Schmitt, L. Tassan-Got, C. Villagrasa, C. Volant, and O. Yordanov. Isotopic production cross sections of the residual nuclei in spallation reactions induced by ^{136}Xe projectiles on proton at 500 MeV. *Nuclear Physics A*, 899:116–132, 2013.
- [67] P. Napolitani, K.-H. Schmidt, L. Tassan-Got, P. Armbruster, T. Enqvist, A. Heinz, V. Henzl, D. Henzlova, A. Kelić, R. Pleskač, M. V. Ricciardi, C. Schmitt, O. Yordanov, L. Audouin, M. Bernas, A. Lafriaskh, F. Rejmund, C. Stéphan, J. Benlliure, E. Casarejos, M. Fernandez Ordonez, J. Pereira, A. Boudard, B. Fernandez, S. Leray, C. Villagrasa, and C. Volant. Measurement of the complete nuclide production and kinetic energies of the system $^{136}\text{Xe}+\text{hydrogen}$ at 1 GeV per nucleon. *Phys. Rev. C*, 76:064609, Dec 2007.
- [68] Matteo Agostini, Giovanni Benato, Jason A. Detwiler, Javier Menéndez, and Francesco Vissani. Toward the discovery of matter creation with neutrinoless $\beta\beta$ decay. *Rev. Mod. Phys.*, 95:025002, May 2023.
- [69] F. James and M. Roos. Minuit: A System for Function Minimization and Analysis of the Parameter Errors and Correlations. *Comput. Phys. Commun.*, 10:343–367, 1975.
- [70] R. Brun and F. Rademakers. ROOT: An object oriented data analysis framework. *Nuclear Instruments and Methods in Physics Research Section A: Accelerators, Spectrometers, Detectors and Associated Equipment*, 389:81–86, 1997. See also "ROOT" [software], Release v6.32/08, Nov 14, 2024.
- [71] J M Hardin. Wilks's theorem, global fits, and neutrino oscillations. *European Journal of Physics*, 45(2):025806, feb 2024.

- [72] Gary J. Feldman and Robert D. Cousins. Unified approach to the classical statistical analysis of small signals. *Phys. Rev. D*, 57:3873–3889, Apr 1998.
- [73] K. Asakura, A. Gando, Y. Gando, T. Hachiya, S. Hayashida, H. Ikeda, K. Inoue, K. Ishidoshiro, T. Ishikawa, S. Ishio, M. Koga, S. Matsuda, T. Mitsui, D. Motoiki, K. Nakamura, S. Obara, M. Otani, T. Oura, I. Shimizu, Y. Shirahata, J. Shirai, A. Suzuki, H. Tachibana, K. Tamae, K. Ueshima, H. Watanabe, B.D. Xu, H. Yoshida, A. Kozlov, Y. Takemoto, S. Yoshida, K. Fushimi, T.I. Banks, B.E. Berger, B.K. Fujikawa, T. O’Donnell, L.A. Winslow, Y. Efremenko, H.J. Karwowski, D.M. Markoff, W. Tornow, J.A. Detwiler, S. Enomoto, and M.P. Decowski. Search for double-beta decay of ^{136}Xe to excited states of ^{136}Ba with the KamLAND-Zen experiment. *Nuclear Physics A*, 946:171–181, 2016.
- [74] Pekka Pirinen and Jouni Suhonen. Systematic approach to β and $2\nu\beta\beta$ decays of mass $a = 100 - 136$ nuclei. *Phys. Rev. C*, 91:054309, May 2015.
- [75] A. Li, Z. Fu, C. Grant, H. Ozaki, I. Shimizu, H. Song, A. Takeuchi, and L. A. Winslow. KamNet: An integrated spatiotemporal deep neural network for rare event searches in KamLAND-Zen. *Phys. Rev. C*, 107:014323, Jan 2023.

CURRICULUM VITAE

Hasung Song

Department of Physics
 Boston University
 Email: hwsong@bu.edu

Education

- **Ph.D. in Physics**, Boston University, 2019–Present
- **M.Sc. in Physics**, Boston University, 2019–2022
- **B.Sc. in Physics**, University of California, Berkeley, 2016–2018

Professional Experience

- **Post-Baccalaureate Researcher**, University of California, Berkeley, 2018–2019

Selected Publications

- "Search for Majorana Neutrinos with the Complete KamLAND-Zen Dataset" KamLAND-Zen Collaboration, arXiv:2406.11438 [hep-ex] (2024)
- "Eos: conceptual design for a demonstrator of hybrid optical detector technology" T. Anderson et al. JINST 18 P02009 (2023)
- "KamNet: An integrated spatiotemporal deep neural network for rare event searches in KamLAND-Zen" A. Li, et al. Phys. Rev. C 107, 014323 (2023)
- "RFSoC-based front-end electronics for pulse detection" S.N. Axani et al. 2024 JINST 19 P03013 (2024)
- "Search for the Majorana Nature of Neutrinos in the Inverted Mass Ordering Region with KamLAND-Zen" KamLAND-Zen Collaboration, Phys. Rev. Lett. 130, 051801 (2023)

Scientific Collaborations

- EoS Collaboration 2023–Present
- NuDOT Collaboration 2022–Present
- KamLAND Collaboration 2020–Present
- NIM+ 2020–2021
- Mu2E Collaboration 2018–2019

Conferences and Presentations

- ”Getting Excited About Double Beta Decay in KamLAND-Zen”, APS DNP, Talk, Boston, MA, 2024.
- ”Understanding KamNet Performance in KamLAND-ZEN with ML Interpretability”, SLAC Summer Institute, Poster, SLAC, 2023.
- ”KamLAND-Zen’s New ML Tricks”, Neutrino Physics and Machine Learning, Talk, Northeastern University, 2023.
- ”Rejecting Spallation Backgrounds in KamLAND-ZEN with KamNet”, Neutrino, Poster, Seoul, Korea, 2022.
- ”Rejecting Spallation Backgrounds in KamLAND-ZEN with KamNet”, TAUP, Poster, Valenica, Spain, 2021.
- ”Neutrinoless Muon-to-Positron Conversion at Mu2e”, APS April Meeting, Talk, Denver, Colorado, 2019.

Teaching Experience

- Physics 211 General Physics I, Teaching Assistant, Boston University, Summer 2020.
- Physics 211 General Physics I, Teaching Assistant, Boston University, Fall 2019.

Professional Service

- Member, Graduate Student Council, Boston University Physics Department, 2019–Present.